

Vol II

NASA-CR-61180

VOLUME II - APPENDIXES

AUGUST 1967

PREPARED UNDER
NASA-AUBURN-ALABAMA
SUMMER FACULTY FELLOWSHIP PROGRAM
IN ENGINEERING SYSTEMS DESIGN

NASA CONTRACT NSR 01-003-025

REPORT NO. CR-61180

J O V E



SCHOOL OF ENGINEERING
AUBURN UNIVERSITY
AUBURN, ALABAMA

N68-10569

(ACCESSION NUMBER)
192
(THRU)
1
(CODE)
31
(CATEGORY)

(PAGES)
Cr # 61180
(NASA CR OR TMX OR AD NUMBER)

JOVE

JUPITER ORBITING VEHICLE FOR EXPLORATION

VOLUME II

APPENDIXES

prepared under

CONTRACT NSR 01-003-025
UNIVERSITY AFFAIRS OFFICE
HEADQUARTERS
NATIONAL AERONAUTICS AND SPACE ADMINISTRATION

with the cooperation of

THE

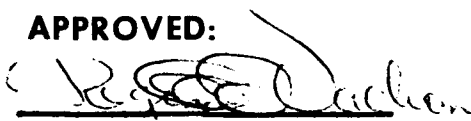
ADVANCED SYSTEMS OFFICE
GEORGE C. MARSHALL SPACE FLIGHT CENTER
NATIONAL AERONAUTICS AND SPACE ADMINISTRATION

by

AUBURN-ALABAMA ENGINEERING SYSTEMS DESIGN
SUMMER FACULTY FELLOWS

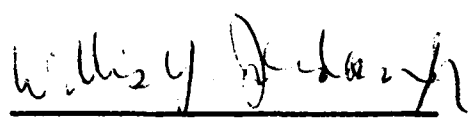
AUGUST, 1967

APPROVED:


Reginald D. Vachon, Ph. D.
Alumni Professor, Auburn Univ.
Co-Director

Gordan W. Breland, Ph. D.
Asst. Professor, Auburn Univ.
Associate Director

Ross M. McDonald, Ph. D.
Asst. Professor, University of Tulsa
Associate Director


Willis Y. Jordan
MSFC Advanced Systems Office
Co-Director

Alfred M. Leppert
Asst. Professor, Auburn Univ.
Associate Director

PREFACE

Objective

Systems engineering or systems engineering design has become an accepted term to describe the multidisciplinary or interdisciplinary character of the "systematic design" of any large engineering system. It emphasizes and attempts to systematize, through the availability of modern techniques, the design of modern, complex, multidisciplinary engineering systems. The term seems to have originated in the aerospace field where the complexity of modern aerospace systems demanded a systematically controlled approach to design to insure that all factors of all subsystems, representing many disciplines, were carefully integrated into the final system. The importance of the multidisciplinary systems approach has been recognized by the National Aeronautics and Space Administration to the extent that they now support three engineering systems design summer programs for engineering faculty fellows.

This report summarizes the results of one of these programs. This study was conducted by 19 faculty members, representing some 14 engineering colleges throughout the United States. The program was conducted by Auburn University and University of Alabama at the Marshall Space Flight Center in Huntsville, Alabama. The group received a great deal of technical assistance from the Marshall Space Flight Center and from the many contractors that assist the Center. The technical data contained in this report, however, does not necessarily reflect the views or policy of the George C. Marshall Space Flight Center, or any other government agency or private corporation.

The Acknowledgments section of Volume I lists individuals and companies to whom we are especially indebted.

The University Affairs Office, National Aeronautics and Space Administration, Headquarters, Washington, D. C. , funded the project with the primary objective of allowing the participants to obtain actual design experience as members of a multidisciplinary design team. The engineering educational world is indebted to NASA for this farsighted assistance to engineering educational programs of this country.

Organization

Very early in the program, the participants were briefed on the main objectives, both technical and educational. They selected an interplanetary orbiting vehicle as the primary design objective, then organized themselves into groups and assigned tasks, according to the background of each faculty fellow. Originally, there were four groups: Mission Profile, Spacecraft Configuration, Telecommunications, and Experiments. Spacecraft Configuration eventually split itself into several groups because of its size, and the final actual grouping was more like the chapter headings in this report. The participants and their educational backgrounds are listed in the next section.

The program had three phases. The first was an educational one during which time the group organized itself, listened to extensive briefings by the Marshall people and representatives of their associated contractors, and developed background material pertinent to the solution of the problems. This phase covered approximately three weeks.

The next five weeks were spent evaluating alternate solutions to the problems as they developed, effecting trade-offs, and in preliminary design studies and analysis. The last two weeks were occupied with the organization of the material for the oral presentation and for the written material that appears in this report.

The participants of this program sincerely hope that this report of their ten weeks effort at the Marshall Space Flight Center will be of interest and value to the Marshall Space Flight Center and to the space effort of the United States. Any such benefit would be a real bonus since, as has already been pointed out, the primary purpose of the program was to give a group of college professors a feel for, and experience with, systems engineering.

This final report of JOVE is broken into two volumes for convenience; Volume I, Mission and System Study, and Volume II, Appendixes. It should be understood that both volumes represent an integral part of the results of this program and both must be studied to obtain the full story of the JOVE mission. The format selected by the fellows was to keep the technical description directly related to the mission in Volume I, and to place supporting engineering and scientific data in Volume II.

Comments, criticisms, suggestions, and questions will be answered as promptly as possible if they are directed to the attention of Dr. R. I. Vachon, Alumni Professor of Mechanical Engineering, Auburn University, Auburn, Alabama 36830.

LIST OF PARTICIPANTS

1. Fayette Johnson Brown
Ass't Prof. of Mech. Engr.
Chico State College
B. S. , Ohio University, in 1952
M. S. M. E. , Univ. of Washington, 1956
Spacecraft Configuration Group
2. Ward Ervin Bullock
Assoc. Prof. in Mech. Engr.
State University of New York at
Buffalo
M. E. , Univ. of Cincinnati, 1928
Spacecraft Configuration Group
3. James J. Carlson
Assoc. Prof. of Mech. Engr.
University of Nevada
B. S. M. E. , Univ. of Nevada, 1955
M. S. M. E. , Univ. of California
(Berkeley) 1959
Engineer, Stanford University, 1965
Spacecraft Configuration Group
4. John E. Dimatteo, Sr.
Assoc. Prof. of Engr. Graphics
Newark College of Engineering
B. S. M. E. , Copper Union, 1931
M. S. M. E. , Stevens Inst. of Tech. ,
1950
Spacecraft Configuration Group
5. James Edward Dupree
Instructor of Electrical Engr.
Auburn University
B. E. E. , Auburn University, 1960
M. S. E. E. , Auburn University, 1963
Electronics Group Leader
6. Donnell Wayne Dutton
Prof. of Aerospace Engineering
Georgia Institute of Technology
B. S. M. E. , Univ. of Missouri School
of Mines and Metalurgy, 1935
M. S. A. E. Georgia Inst. of Tech. , 1940
M. E. (Honorary), Univ. of Missouri
at Rolla, 1959
Spacecraft Configuration Group Leader
Project Leader
JOVE Editor
7. Norman Jay Gleicher
Assistant Professor
State Univ. of New York
B. E. E. , City College of New York,
1962
M. E. E. , New York University, 1964
Electronics Group Leader

8. Robert Grant Golden, Jr.
Ass't. Prof. of Engr. Graphics
and Design
Newark College of Engineering
A. B. , Little Rock College, 1951
B. S. M. E. , Newark College of
Engineering, 1956
A. M. , Seton Hall University, 1961
Mission Profile Group Leader
9. John Wesley Herring, Jr.
Assoc. Prof. of Elect. Engr.
Mississippi State University
B. S. E. E. , Mississippi State Univ. ,
1950
M. S. E. E. , Univ. of Arizona, 1960
Ph. D. , Univ. of Arizona, 1967
Electronics Group Leader
10. Martin Theophilus Jasper
Ass't. Prof. of Mech. Engr.
Mississippi State University
B. S. , Mississippi State Univ. , 1955
M. S. , Mississippi State Univ. , 1962
Ph. D. , Univ. of Alabama, 1967
Spacecraft Configuration Group
11. Murray I. Lieb
Instructor of Mathematics
Newark College of Engineering
B. S. E. E. , Newark College of Engr. ,
1961
M. S. E. E. , Newark College of Engr. ,
1963
M. S. (Math), New York University,
1965
Experiments Group Leader
12. Philip Arthur Loretan
Ass't. Prof. of Nuclear Engr.
Iowa State University
B. S. , University of Notre Dame, 1961
M. S. , Iowa State University, 1963
Ph. D. , Iowa State University, 1965
Spacecraft Configuration Group
13. Frank Stanley Moore, Jr.
Ass't. Prof. Physics
Pfeiffer College
B. S. , Hampden Sydney College, 1957
M. S. , Univ. of Michigan, 1959
Experiments Group Leader
14. Jacob Monroe Schmidt
Assoc. Prof. Mech. Engr. and
Physics
Chico State College
A. B. Physics, Phillips Univ. , 1932
M. S. Physics, Univ. of Oklahoma,
1932
Ph. D. , Univ. of Southern Calif. , 1944
Experiments Group Leader

- | | |
|--|---|
| 15. Leverne Kenneth Seversike
Ass't. Prof. of Aerospace Engr.
Iowa State University | B.S. , Iowa State University, 1958
M.S. , Iowa State University, 1961
Ph.D. , Iowa State University, 1964

Mission Profile Group Leader
Project Leader |
| 16. David W. C. Shen
Prof. of Elect. Engr.
Moore School of Electrical Engr. | B.Sc. National Tsing Hua Univ. , 1938
Ph.D. University of London, 1948

Electronics Group |
| 17. Kenneth Alva Stead
Instructor, Civil Engr.
University of So. Carolina | B.C.E. , Univ. of Louisville, 1953
M.S. , Univ. of Missouri, 1961

Spacecraft Configuration Group |
| 18. Harold Francis Trent
Assoc. Prof. of Industrial Engr.
Virginia Polytechnic Institute | B.S. , Roanoke College, 1941
M.S. , Virginia Polytechnic Inst. , 1958

Spacecraft Configuration Group |
| 19. Jesse H. Wilder
Professor of Mech. Engr.
University of Dayton | B.S.M.E. , Duke University, 1947
M.S. , State University of Iowa, 1949

Spacecraft Configuration Group Leader
Project Leader |

TABLE OF CONTENTS

	Page
Preface	iii
List of Participants	vi

APPENDIX A. PHYSICAL PROPERTIES OF JUPITER

Definition of Symbols	A-1
General Features	A-5
Physical Characteristics	A-6
Orbital Elements	A-10
Radio-Frequency Emission	A-13
Electromagnetic and Particle Fields	A-16
Visual Surface	A-19
Atmosphere Composition	A-29
Atmosphere and Internal Structure	A-32
Atmospheric Circulation	A-42
Satellites	A-49
References	A-52
Bibliography	A-58

APPENDIX B. INTERPLANETARY SPACE ENVIRONMENT

Definition of Symbols	B-1
General Features	B-3
Meteoroid Environment	B-4
Asteroid Environment	B-13
Comet Environment	B-21
Galactic Cosmic Radiation	B-24
Solar Wind and Space Magnetic Fields	B-26
Solar Flares	B-31
Radiation Properties of the Sun	B-38
References	B-42
Bibliography	B-44

TABLE OF CONTENTS (Concluded)

Page

APPENDIX C. RADIO OCCULTATION EXPERIMENTS

Introduction	C-1
Occultation Measurements from a Single Orbiting Vehicle	C-5
Occultation Measurements using an Orbital Pair of Vehicles	C-5
Summary and Recommendations	C-12
References	C-13

APPENDIX D. RTG ALTERNATE POWER SUPPLY SYSTEM

General Discussion	D-1
Summary	D-3
References	D-4

APPENDIX E. ALTERNATE ANTENNA CONSIDERATIONS

Definition of Symbols	E-1
Introduction	E-2
Electronically Scanned Antennas	E-3
Deployable Antennas	E-9
References	E-12

APPENDIX F. DETAILED STRUCTURE CALCULATIONS . . . F-1

APPENDIX G. ON-BOARD NAVIGATION AND GUIDANCE SYSTEM

Definition of Symbols	G-1
Introduction	G-3
Saturn Ascending Phase Guidance	G-5
Celestial-Inertial Guidance	G-5
Concluding Remarks	G-12
References	G-14

APPENDIX H. LEMDE EXHAUST JET EFFECTS

Definition of Symbols	H-1
References	H-10

LIST OF ILLUSTRATIONS

Figure	Title	Page
A-1.	Orbits of Jupiter and Earth	A-14
A-2.	The Off-Center Radiation Belts of Jupiter	A-20
A-3.	Integrated Electron Flux for Earth and Jupiter.	A-21
A-4.	Jupiter Integrated Electron Flux for $\gamma = 1.02$	A-22
A-5.	Jupiter Integrated Electron Flux for $\gamma = 2.0$	A-23
A-6.	Jupiter Trapped Radiation Iso-Flux Map	A-24
A-7.	Nomenclature of Jovian Belts and Zones and Associated Visible Surface Currents.	A-26
A-8.	Jovian Cloud Layers Proposed by Gallet Overlying Jovian Interior by Peebles	A-43
B-1.	Spectra of Energetic Particles Observed in the Solar System . . .	B-5
B-2.	Parametric Analysis of Meteoroid Particle Environment	B-10
B-3.	Meteoroid Penetrations of Aluminum Sheet for Near-Earth Region	B-14
B-4.	Meteoroid Penetrations of Aluminum Sheet for Interplanetary Region	B-15
B-5.	Meteoroid Penetrations of Aluminum Sheet for Asteroidal Region I	B-16
B-6.	Meteoroid Penetrations of Aluminum Sheet for Asteroidal Region II	B-17
B-7.	Meteoroid Penetration for Aluminum Sheet for Near-Jupiter Region	B-18
B-8.	Integral Spectra of Galactic Cosmic Radiation	B-25
B-9.	Primary Cosmic Ray and Van Allen Belt Radiation Environment in Space	B-27
B-10.	Interaction of Solar Wind with Magnetic Fields	B-29
B-11.	Earth Trapped Radiation	B-30
B-12.	Energy Spectrum of Typical Relativistic Solar Flare and a Severe Nonrelativistic Solar Flare	B-32
B-13.	The Probability, p , of the Occurrence of a Flare Whose Flux is Equal to or Greater than N , and Whose Individual Particle Energies are Equal to or Greater than 30 MeV	B-34
B-14.	Solar Flare/Sunspot Correlation (Cycles 21 and 22 were projected from Cycles 18 and 19)	B-35
B-15.	Time Development of Model Flare Event	B-37

LIST OF ILLUSTRATIONS (Concluded)

Figure	Title	Page
C-1.	Radio Occultation Geometry	C-2
C-2.	Orbital Pair Occultation Experiment (Schematic)	C-7
C-3.	Occultation Geometry for $R_{pm} = R_J$, Apsidal Ratio = 10	C-9
E-1.	Coordinate System	E-4
E-2.	JOVE Phase Steered Array Concept	E-6
E-3.	JOVE Deployable Reflector Concept	E-11
G-1.	The Basic Navigation Loop in the Inertial Frame	G-4
G-2.	Adaptive Saturn Guidance System	G-6
G-3.	Determination of Vehicle Position Using Gimballed Sun Sensor	G-8
G-4.	Recursive Navigation Computation	G-11
G-5.	Error Signal for ΔV Steering	G-13
H-1.	Turning Angle of Prandtl-Meyer Flow	H-5
H-2.	Sketch of LEM Engine Exhaust for Space Environment	H-6
H-3.	Model for Radiant Heat Transfer from LEMDE Exhaust Jet to Spacecraft	H-8

LIST OF TABLES

Table	Title	Page
A-1.	Jupiter Gravitational Constants	A-9
A-2.	Summary of Orbital and Physical Characteristics of Jupiter . . .	A-11
A-3.	Orbital Constants of Jupiter	A-12
A-4.	Probable Atmospheric Composition	A-32
A-5.	Two Atmospheric Models of Jupiter's Upper Atmosphere	A-34
A-6.	Model of Jovian Upper Atmosphere	A-37
A-7.	Model Planet for Jupiter's Interior	A-44
A-8.	Climate Zones	A-48
A-9.	Satellites of Jupiter	A-50
B-1.	Meteoroid Environment Parameters	B-8
B-2.	Particles per Square Meter per Second per 2π Steradian Unshielded from Mass \geq One Microgram	B-9
B-3.	Orbital Elements for some Asteroids	B-20
B-4.	Observed Comets	B-23
B-5.	Variation of Solar Constant with Solar Distance	B-39
C-1.	Communications Circuit Calculation JOVE-to-Ground Down-link Distance	C-6
C-2.	Communication Circuit Calculation (10 Watts Power)	C-10
C-3.	Communication Circuit Calculation (100 Watts Power)	C-11



APPENDIX A

PHYSICAL PROPERTIES OF JUPITER

APPENDIX A

PHYSICAL PROPERTIES OF JUPITER

DEFINITION OF SYMBOLS

A	Planetary albedo (m^2)
a	Radius of planet (km)
a	Semi-major axis (km)
B	A parameter
c	Speed of sound (km/sec)
D	A parameter
d	Characteristic length (km)
e	Flattening or oblateness (dimensionless)
e	Eccentricity of orbit (dimensionless)
e_{dyn}	Dynamical flattening (dimensionless)
e_{opt}	Optical flattening (dimensionless)
G	Constant of universal acceleration $\frac{\text{dyne-cm}}{\text{gm}^2}$
g	Acceleration of gravity cm/sec^2
g_{eq}	Gravitational acceleration at Jupiter's equator $\frac{\text{dyne-cm}}{\text{gm}^2}$
g	Gravitational acceleration at any latitude $\frac{\text{dyne-cm}}{\text{gm}^2}$
KE	Kinetic energy

DEFINITION OF SYMBOLS (CONTINUED)

i	Inclination of the orbit to the ecliptic (radians)
L	Characteristic length (km)
L	Mean longitude at any time t. (km)
L_o	Mean longitude at epoch of Jupiter (km)
M	Molecular weight (gm per gm mole)
M	Mass of Jupiter (gm)
M	Rotational mach number
N(E)	Electron density (electrons/cm ³)
n	Mean daily motion (km/sec)
P	Pressure (atmosphere)
R	Rossby number
R	Radius at latitude of an oblate spheroid (km)
R_{eq}	Equatorial radius of Jupiter (km)
\bar{R}	Mean radius of an oblate spheroid
R_E	Earth radius (km)
R_J	Jupiter radius (km)
S_J	Mean solar constant of Jupiter $\left(\frac{\text{cal}}{\text{cm}^2 \text{ min}}\right)$
T	Temperature (°K)
T_c	Cloudtop (visible surface) temperature (°K)
T_e	Blackbody temperature (°K)

DEFINITION OF SYMBOLY (CONTINUED)

T_{eq}	Mean planetary temperature ($^{\circ}$ K)
T_z	Temperature at any elevation z ($^{\circ}$ K)
t	Time (seconds)
ν	Typical horizontal wind speed (km/sec)
z	Altitude (cm)
Γ	Vertical gradient of potential density
γ	Electron field strength parameters
ϕ	Planetocentric, angle between a radius vector to the point and the equatorial plane, (radians)
$\tilde{\phi}$	Angle of Jupiter's magnetic field (rad)
ϕ_e	Electron flux (electrons/cm ² sec)
ρ	Density (gm/cm ³)
$\bar{\rho}$	Mean density of an oblate spheroid (gm/cm ³)
σ	Stefan-Boltzmann constant
Ω	Longitude of ascending node on the ecliptic measured from the vernal equinox (radian)
Ω	Rotation of planet (rad/sec)
o	Optical thickness at cloudtop (m)
z	Average optical thickness
ω	Brunt-Vaisala frequency
ω	Angular velocity of rotation (rad/sec)

DEFINITION OF SYMBOLS (CONTINUED)

- ω Longitude of the perihelion (radians)
- $\bar{\omega}$ Mean anomaly

GENERAL FEATURES

Jupiter is the largest and most massive planet in the solar system as well as being the innermost of the nonterrestrial-type planets. The mass of Jupiter is more than twice the sum of the masses of the other planets while the diameter is slightly over a tenth of that of a sun. It has a low mean density which indicates that the present chemical composition may be very similar to what it was when the planet was formed and that the relative chemical abundances are more solar-like than Earth-like. Thus, Jupiter greatly influences the Solar System and is the chief source of perturbations within it.

In a sense Jupiter is similar to Venus in that a dense cloudy atmosphere obscures visual or photographic observations of the surface. Whereas very little detail is visible across the planetary disk of Venus, Jupiter's visual surface or cloudtop exhibits a band-like structure that is in a continual state of unrest manifested by changes in shape, detail, motion, and coloration. In addition to the belts and zones there have been observed several special features, the best known being the Great Red Spot.

Jupiter's atmosphere contained enormous amounts of hydrogen and lesser amounts of ammonia, methane, and other light carbon-hydrogen-nitrogen gases. Although visual observation below the clouds is impossible, it has been suggested that the solid surface of the planet contains primarily hydrogen in, probably, liquid and solid states.

Jupiter has a wide range of radio-frequency emission not of thermal or solar origin. These emissions, as well as other evidence, suggest that this giant planet has a very extensive magnetic field and large Van Allen radiation belt containing trapped particles.

Jupiter has 12 known satellites, four of which are very large in size. These operate in two systems, inner and outer, and are probably terrestrial in nature.

The principal reference for this brief summary is the "Handbook of the Physical Properties of the Planet Jupiter," [Ref. 1]. Other references are listed for the reader's benefit so that he may conduct a more thorough search on particular points of interest.

PHYSICAL CHARACTERISTICS

Jupiter, by virtue of its mass, is second only to the sun as the main body of the solar system. Its mass is some 318 times greater than Earth's. It is, therefore, expected that Jupiter causes significant gravitational perturbations on other members of the solar system, particularly on its neighboring planets, Mars and Saturn, and the asteroids.

These gravitational perturbations on the motion of other planets is one method of calculating the mass of this giant planet. The other method which is somewhat more suspicious is the scaling of the orbits of Jupiter's satellites. Investigators have used Saturn, the four largest satellites, asteroids, and comets in determining the mass. Clemence [Ref. A-2] discussed all of the values and suggested that Jupiter's mass be taken as the reciprocal of 1047.41 ± 0.02 where the reference mass is the sun and is unity.

Jupiter's shape is definitely oblate. Measurement of its diameter and shape are further hampered by the very dense cloud layer that covers the planet. For this reason measurements pertain to the visible surface which is the top of the cloud layer. Although the actual depth of this cloud layer is unknown, theoretical estimates have been made from which the possible diameter of the solid or liquid surface underlying the clouds can be inferred.

Two types of flattening are quoted, optical flattening and dynamic flattening. The former is oblateness value received by the telescopic image of Jupiter while the latter is a flattening value received from the orbital characteristics of certain appropriate satellites. The values obtained by both of these methods are not significantly different. An average value for optical flattening might be taken as the reciprocal of 16.35 while an average value for dynamic flattening might be the reciprocal of 15.34. It might be noted that the optical flattening of Mars is twice that of the dynamical.

Since Jupiter is very oblate, its radius varies with latitude and can be considered as an oblate spheroid according to the formula:

$$R = R_{eq} (1 - e \sin^2 \phi) \quad (1)$$

Where: R_{eq} - equatorial radius

ϕ - planetocentric (angle between a radius vector to the point and the equatorial plane)

e - flattening or oblateness

R - radius at latitude

In contrast to the visible surface, the radii of the solid surface depends on the atmospheric depth lying below the surface as well as the value of the flattening. Rabe suggested the optical flattening as $e_{opt} = 0.06117$ and Brouwer and Clemence suggested for the dynamic flattening as $e_{dyn} = 0.06518$. Using these and an atmospheric depth assumption, the radii of the solid surface can be found.

The mean radius of an oblate spheroid is:

$$\bar{R} = \left(1 - \frac{e}{3}\right) R_{eq} \quad (2)$$

If a visible surface has a mean radius of 70 035 kilometers and the mean radius of its solid globe is 69 347 kilometers (this assumes a 500 kilometer high cloud cover), then the eccentricity is found to be, using the relation:

$$e = \sqrt{e(1-e)} \quad (3)$$

$$e_{opt} = 0.23146 \text{ and } e_{dyn} = 0.24684$$

Jupiter has the shortest rotation period of the major planets. This, along with Jupiter's great mass, accounts for the large gravitational forces which lead to the dynamical flattening. Furthermore, the cloud layers have different periods of rotation, particularly in the equatorial regions. The question naturally arises as to the period of rotation of the solid surface.

There are three general methods used for determining the rotation rate of Jupiter which are: (1) The optical (or visual) method associated with the cloud surface, (2) The spectroscopic (or Doppler shift) method for the upper atmosphere, and (3) The radio-emission method. These will be discussed in more detail later; however, the "radio-period" is taken to be $9^h 55^m 29^s .37$.

The mean density of an oblate spheroid is approximately the same as that of a sphere having a radius equal to the mean radius of the spheroid if the oblateness is sufficiently small. This can be approximated by:

$$\bar{\rho} = (1 + e_{\text{dyn}}) \frac{M}{4/3 \pi R_{\text{eq}}^3}$$

Where: M - Mass (1.899×10^{30} gm)

e_{dyn} - Dynamic oblateness (0.06518)

R_{eq} - Equatorial radius (71 387 kilometers)

giving the mean density, using the values above, as:

$$\bar{\rho} = 1.327 \pm 0.008 \text{ g/cm}^3$$

The equatorial radius introduces the most uncertainty in this calculation.

The oblateness, large mass, and rapid rotation of Jupiter greatly affect the gravitational acceleration. To the first order of oblateness this can be given by two formulae:

$$g_{\text{eq}} = \left(\frac{GM}{R_{\text{eq}}^2} \right) \left[1 + e - 3\omega^2 (R_{\text{eq}}^3/2GM) \right] \quad (5)$$

and

$$g_{\phi} = g_{\text{eq}} \left[1 + \left(\frac{5\omega^2 R_{\text{eq}}^3}{2gM - e} \right) \sin^2 \phi \right] \quad (6)$$

Where: G - constant of universal acceleration = 6.670×10^{-8}
 $\frac{\text{dyne cm}}{\text{g}^2\text{m}}$

M - Mass

R_{eq} - Equatorial radius

e - Oblateness

ω - Angular velocity of rotation

g_{eq} - Gravitational acceleration at the equator

g_{ϕ} - Gravitational acceleration at any latitude.

Table A-1 gives the resulting gravity of Jupiter in terms of centimeter-gram-seconds and terrestrial units (g) in terms of zeno-centric latitude at the visible surface. The same values of the constants in equations (5) and (6) are used in the computation of the mean density and a terrestrial "g" unit is assumed to be $980.6 \frac{\text{cm}}{\text{sec}^2}$ along with a period of $9^{\text{h}} 52^{\text{m}}$.

TABLE A-1. JUPITER GRAVITATIONAL CONSTANTS

<u>Zenocentric Latitude,</u> <u>(north or south), degrees</u>	<u>Absolute Value of</u> <u>Gravity, g cm/sec²</u>	<u>Relative Value of</u> <u>Gravity, Terrestrial</u> <u>"g" Units</u>
0	23.12	2.36
15	23.58	2.40
30	24.04	2.45
45	24.96	2.55
60	25.89	2.64
75	26.56	2.71
90	26.81	2.74

The temperature of Jupiter has been estimated by two means: (1) using Stefan's law by equating the solar energy absorbed by the planet to that radiated from it and (2) by Radiometry.

The first method assumes that the planet acts as a blackbody relative to its thermal radiation characteristics, and for a rapidly rotating Jupiter, it is assumed that a constant radiative temperature over the entire surface is maintained so that energy is radiative over an area four times larger than that in which it is effectively received. Thus Stefan's law is:

$$T_{\text{eq}}^4 = S_j \frac{(1 - A)}{4\sigma} \quad (7)$$

Where: S_j - The mean solar constant of Jupiter (0.073 ± 0.001
 $\frac{\text{cal}}{\text{cm}^2 \text{ min}}$ for a body 5.2 astronomical units from the
 sun)

σ - The Stefan-Boltzmann constant

A - The planetary albedo (0.45)

T_{eq} - The mean planetary temperature

Giving $T_{eq} = 105 \pm 3^\circ\text{K}$.

On the other hand, radiometry gives equilibrium temperatures, measured from the emission from Jupiter in the 9 to 13 micron Earth atmospheric window from 128 to 130° K. It should be noted that the main radiating element in the Jovian upper atmosphere is ammonia which absorbs very strongly in the 8-14 micro region. Using an assumed ammonia content of 1 cm-atm of ammonia and a lengthy analysis of the available data, Opik [Ref. A-3] concluded that the cloudtop temperature is $T_c = 156^\circ\text{K}$.

The difference between the equilibrium and radiometric temperatures has been attributed by Opik to be the radiation of internal heat which is produced by gravitational contraction. This internal heat has also been associated with radioactivity of the interior, tidal dissipation, meteor bombardment, magnetic field decay, and an atmospheric greenhouse effect created by pressure induced transitions in the abundant molecular hydrogen.

Radiometric temperature maps of the Jovian disk by Wildley, et al., [Ref. A-4] shows very slight temperature variations, only a 5 degree decrease from the disk center, at an average of 129° K, to the outer periphery of the disk. Interesting enough is that the equatorial belts seem to be about a half a degree warmer than the adjoining tropical zones, and the Great Red Spot is 1.5 to 2 degrees cooler than adjacent areas.

Table A-2 gives a summary of the orbital and physical characteristics of Jupiter and are the accepted values for this report.

ORBITAL ELEMENTS

Jupiter moves slowly about the sun completing an orbit in approximately 12 years. This orbit is nearly circular and is inclined to the ecliptic by slightly more than 1 degree. The respective positions of the orbits of Earth and Jupiter is shown in Figure A-1 and the important orbital constants derived from the orbital elements of both planets are listed in Table A-3.

TABLE A-2. SUMMARY OF ORBITAL AND PHYSICAL CHARACTERISTICS OF JUPITER

	<u>Jupiter</u>	<u>Earth</u>	<u>Jupiter/</u> <u>Earth</u>
Orbit semi-major axis (meters)	7.781x10 ¹¹	1.49527x10 ¹¹	5.20
Aphelion distance (meter)	8.159x10 ¹¹	1.52028x10 ¹¹	5.37
Perihelion distance (meters)	7.404x10 ¹¹	1.47026x10 ¹¹	5.04
Eccentricity of orbit	0.0485	0.016726	2.90
Orbital period (around sun) (year)	11.86	1	11.86
Inclination to ecliptic	1.306 deg	0	-
Inclination of equator to plane of orbit	3° 7'	23° 27'	.133
Equatorial radius (meters)	7.1384x10 ⁷	6.378145x10 ⁶	11.19
Flattening	1/15.34	1/298.34	18.66
Volume (m ³)	1.42844x10 ²¹	1.0832124x10 ²¹	1.32x10 ³
Sidereal rotation period (hr)	9.842	23.93447	.41
Density (kg/m ³)	1.327x10 ³	5.518229x10 ³	.24
Coriolis parameter at pole	3.5466x10 ⁻⁴	1.45842x10 ⁻⁴	2.43
Albedo	.44	.35	1.26
Solar constant ($\frac{\text{Jovles}}{\text{m}^2 \text{ sec}}$)	3.094x10 ³	8.38x10 ⁴	
Surface gravity at pole ($\frac{\text{m}}{\text{sec}^2}$)	26.81		
Surface gravity at equator ($\frac{\text{m}}{\text{sec}^2}$) no rotation	25.37		
Surface gravity at equator with rotation ($\frac{\text{m}}{\text{sec}^2}$)	23.12		

The elliptical motions of a planet are usually described by six orbital parameters. These are:

- a. Semi-major axis. a .
- b. Eccentricity, e .
- c. Inclination of the orbit to the ecliptic, i .
- d. Longitude of the ascending node, Ω , on the ecliptic measured from the vernal equinox.
- e. Longitude of the perihelion, ω .
- f. Mean longitude at epoch of the planet, L_0 , which is the constant
(Cont'd)

TABLE A-3. ORBITAL CONSTANTS OF JUPITER

<u>Constant</u>	<u>Earth Sidereal Years</u>	<u>Earth Tropical Years</u>	<u>Earth Solar Years</u>
Jupiter sidereal year	11.86177	11.86223	4332.587
Mean synodic period	1.09205	1.09210	398.88

DISTANCES FROM SUN

	<u>Astronomical Units</u>	<u>Kilometers</u>	<u>Miles</u>
Mean solar distance	5.202803	778.344×10^6	483.634×10^6
Perihelion distance	4.950805	740.635×10^6	460.210×10^6
Aphelion distance	5.454801	816.032×10^6	507.059×10^6

DISTANCES FROM EARTH

	<u>Astronomical Units</u>	<u>Kilometers</u>	<u>Miles</u>
Minimum distance	3.9308	588.05×10^6	365.4×10^6
Maximum distance	6.4363	962.87×10^6	598.3×10^6

ORBITAL VELOCITY

Mean orbital velocity - 13.1 kilometers/sec, 8.1 miles/sec measured along the ecliptic from equinox to ascending node, then along the orbit from node to perihelion.

in the formula $L = L_0 + nt$ where L is the mean longitude, L_0 at any time, t , after the epoch ($t=0$) with t is the time in ephemeris days since the epoch, and n is the mean daily motion. The mean anomaly is the difference, $L - \tilde{\omega} = L_0 - \tilde{\omega} + nt$.

The orbits of all planets are not precisely defined because of disturbing effects of other planets and bodies. These perturb the orbits making them not strictly elliptical and consist of both secular (that is progressively changing) and periodic terms. Mean elements are used to calculate the planet's position. The tables listing these osculating elements are too lengthy to list in this report. Perhaps the best tabulation is given by the American Ephemeris and Nautical Almanac [Ref. A-5].

There is one notable long-period perturbation in the orbital motion of Jupiter. It is produced by the near-commensurability of the periods of revolution. This perturbation is known as the Great Inequality and has a period of approximately 900 years. Brouwer and Clemence [Ref. A-6] report that the deviations in longitude from elliptic motion may reach 0.3° for Jupiter.

Several investigators have developed theories of the motion of Jupiter. It is, however, the numerical integration by high speed computers which gives the most accurate data. The American Ephemeris and Nautical Almanac [Ref. A-5] is again the best reference.

Oppositions and superior conjunctions of Jupiter with respect to Earth occur every 13 months. The mean synodic period of revolution (time from opposition to opposition) of the two planets is 399 days and the actual synodic period has a maximum difference of 2 days. The distance at opposition can be as much as 46.6 million miles.

RADIO-FREQUENCY EMISSION

Radiometric studies of Jupiter reveal a steady radio-frequency emission having a wide range of wave lengths. The observed range varies from about 3 centimeters to about 62.5 meters and is divided into three distinct categories and one questionable region.

These categories are: (1) the centimeter region up to ~ 3 centimeter, (2) the decimeter region from ~ 3 centimeters to ~ 70 centimeters, and (3) the decameter region from ~ 7 to 62.5 meters. The questionable region, the metric region, is from 70 centimeters to 7 meters.

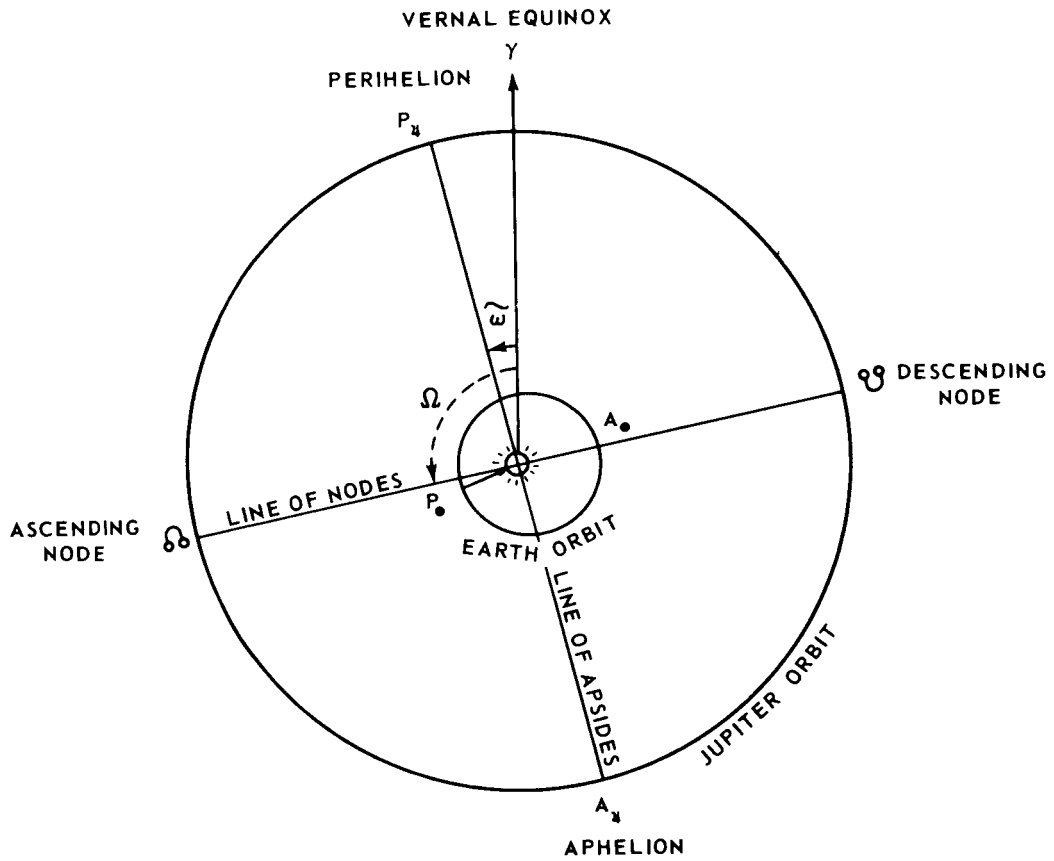


FIGURE A-1. ORBITS OF JUPITER AND EARTH

Radio emission in the centimeter region is undoubtedly thermal in origin and is thought to be caused by the thermal motion of the molecules in the Jovian atmosphere. Although the 3-centimeter radiation is somewhat higher than infrared temperature, it can be accounted for if the radio-frequency emission at 3 centimeters is from regions below the ammonia clouds.

Between ~ 3 and ~ 70 centimeters, the decimeter emission is thought to be the result of electrons spiralling in the Jovian magnetic field and is called cyclotron emission if the radiating electrons are nonrelativistic, and synchrotron emission if they are relativistic. This emission is nonthermal in origin.

The third category, the decameter emission from ~ 7 meters to 62.5 meters, is also nonthermal and its origin is not fully understood.

The emission between the decimeter and decameter, that is between ~ 70 centimeters and 7 meters, the metric region, is not well known because of observational complications such as galactic background and technical limitations such as highly sensitive receivers.

Ionospheric attenuation of Earth blocks out any incoming emission at wavelengths greater than the decameter region. This radiation, hectometric, is undoubtedly present but is so far undetected.

Emission of the decameter radiation occurs in bursts in sharply focused cones originating from specific locations on Jupiter and are definitely correlated with the rotation of the planet. This emission is of the noise-storm type that has short bursts from milliseconds to tens of seconds in duration to form an intense storm lasting a few minutes to several hours. In many cases of noise-storms, the frequency seems to drift up and down the spectrum. This radiation is circularly polarized and exhibits very complex intensity variations. There are indications that decameter radiation is associated with sunspot activity and the probability is inversely related to the sunspot number and strong emission occurs a few days after a strong solar flare.

At present, no theory for the origin of decameter radiation is accepted. There are, however, some mechanisms that help explain the nature of this radiation. Among these are:

- a. Lightning-like discharges from the Jovian atmosphere [Ref. A-7].
- b. Plasma oscillations in the Jovian ionosphere caused by a turbulent atmosphere [Ref. A-8] or shock waves caused by volcanos [Ref. A-9].

- c. Focusing of distant radio sources by the Jovian ionosphere [Ref. A-10].
- d. Chemical explosions in the Jovian atmosphere [Ref. A-11].
- e. Cerenkov radiation emitted by electrons precipitating into the Jovian ionosphere [Ref. A-12].
- f. Maser-like amplification of radiation from mildly relativistic electrons [Ref. A-13].
- g. Cyclotron emission by bunches of electrons at anomalies in the Jovian magnetic field [Ref. A-14].
- h. Amplified low frequency waves (whistlers) in the Jovian magnetosphere [Ref. A-15].
- i. Coherent cyclotron emission [Ref. A-16].

In contrast to the burst emission in the decameter range, the decimeter emission intensity appears to be rather constant for some wavelengths over long periods of time. This difference has been observed by several investigators such as Sloanaker [Ref. A-17]. It has also been observed by these investigators that the decimeter radiation from Jupiter has a strong linearly polarized component and a source dimension which is several times the size of the visible disk. This suggests that electrons are trapped in the Jovian magnetic field forming a Van Allen belt similar to that about Earth.

Cyclotron radiation would require a very large magnetic field, a steep particle spectrum, and a polar extent larger than that which has been observed. For these reasons cyclotron radiation has been discarded in favor of synchrotron emission. Several observers such as Chang and Davis [Ref. A-18] have concluded that the predicted polarization, source dimensions, and the time scales, because of energy losses by the electrons, support synchrotron emission.

ELECTROMAGNETIC AND PARTICLE FIELDS

The basic information concerning the strength and orientation of the magnetic field of Jupiter is provided by the radio emission characteristics of the planet. The cause of the decimeter radiation suggests polar field strengths of the order of 10^3 gauss.

If the decimeter radiation is caused by cyclotron emission, then Field [Ref. A-19] suggests that a polar field strength on the order of 10^5 must exist. However, if the decimeter radiation is caused by synchrotron emission, (that is by relativistic electrons in the Jovian magnetic field) Chang and Davis [Ref. A-18] suggest that polar fields on the order of only 100 gauss exist, and the fields in the emitting region at about $3 R_j^*$ are on the order of 1 to 10 gauss.

Warwick [Ref. A-20] in order to explain the characteristics of the decametric radiation from Jupiter suggested a dipole magnetic field with a magnetic moment of $\sim 4 \times 10^{30}$ gauss cm^3 . Such a field would have strengths at $3 R_j^*$ of ~ 0.1 to 1 gauss. In order to explain the time variations of decimeter emission Berge and Morris [Ref. A-21] required an off-center dipole field. These theories determine the sense of the dipole field. The north pole of Jupiter's magnetic moment is also the north magnetic pole; thus, Jupiter's magnetic moment is opposite in sense to that of Earth.

Several observers of the decimetric radiation suggest that the plane of polarization rocks as Jupiter rotates. This suggests that the axis of the magnetic field is at an angle to the rotational axis. Estimates of this angle, ϕ , range from 9° to 24° . This observation is consistent with a tilted dipole having a displaced center but the location of the center is not known.

Solar winds probably extend as far as Jupiter, and Axford, et al., [Ref. A-22] predict that the sunside of the Jovian magnetosphere is confined somewhat like that of Earth. If the magnetic moment of Jupiter is assumed to be 5×10^4 times the magnetic moment of the earth and if the formulas of Mead and Beard [Ref. A-23] are used, the distance from the center of Jupiter to the boundary will be on the order of $\sim 40 R_j$. Others have suggested it may be on the order to $50 R_j$. The extent of the magnetic field on the nightside of the planet is, as with Earth, unknown.

There must exist trapped relativistic electrons in the Jovian Van Allen belt by the synchrotron radiation. This synchrotron model places restrictions on the product of the magnetic field strength in the emitting region and the number of radiating electrons. Chang and Davis [Ref. A-18] have suggested electron fluxes for three field strengths. These are:

At 0.1 gauss, $\phi_e \sim 5 \times 10^8$ electrons per $\text{cm}^2 \text{sec}^{-1}$ between 10 and 100 MeV.

* R_j is the radius of Jupiter, 69 000 km.

At 1.0 gauss, $\phi_e \sim 5 \times 10^7$ electrons per cm^2 sec between 2.5 and 25 MeV.

At 10 gauss, $\phi_e \sim 25 \times 10^6$ electrons per cm^2 sec between 1 and 10 MeV.

Depending upon which combination is correct, the corresponding flux presumably extends only to $3 R_j$. Thus, between $3 R_j$ to the other boundary of the Jovian magnetosphere, $50 R_j$, the electron flux is too low to emit any decimeter radiation which can be detected from Earth.

Radhakrishnan and Roberts [Ref. A-24] observed that the emission is strongly polarized and that many electrons are trapped in flat helices at large pitch angles. The proportion of these trapped electrons with large pitch angles increases with distance from Jupiter out to $3 R_j$. Figure A-2 shows the model of the off-center radiation belts with plane-polarized decimeter radiation (synchrotron radiation) and the circularly polarized decametric radiation which emanate from helical paths of the trapped electrons.

The source of the trapped electrons in the Jovian magnetosphere is presumably the same as that which supplies Earth's trapped radiation, that is the solar wind.

Finally, a few comments should be made about the location of the homogeneous dynamo that, presumably causes Jupiter's general magnetic field. Hide [Ref. A-25] suggests that if Jupiter's atmosphere is sufficiently deep, the electrical conductivity of its lower atmosphere will be sufficiently high for a dynamo mechanism to operate. In this condition, energy dissipation in Jupiter's atmosphere could be primarily caused by ohmic heating, and the atmosphere may be coupled with the underlying parts of the planet by magnetic fields and not by mechanical friction. Also, the motion of the magnetic field corresponds to the motion of the material within the planet at the lowest depth at which the magnetic Reynolds number exceeds about 10. It is not inconceivable that variations in the radio-period and in the Great Red Spot are manifestations of a gross torsional hydromagnetic oscillation of the interior of Jupiter.

Hove, et al., [Ref. A-26] summarized the work of several investigators who believe that Jupiter's magnetic field is from 0.1 to 10 gauss at a distance of 3 Jupiter radii. The most probable value is about 1 gauss. At this field strength, most observers feel the radio-frequency radiation, if produced by synchrotron radiation, would be produced mainly by electrons in the 1 to 100 MeV energy range. The differential energy spectrum probably can be expressed by

$$N(E) dE = KE^{-\gamma} dE \quad (8)$$

with $\gamma \sim 1$. If a thick shell of lower energy radiation existed around the high energy radiating fields, then γ would be expected to be higher.

Using the above estimates, we find that the average electron density in the vicinity of Jupiter is on the order of $10^{-3} e^-/cm^3$ over 10 planetary volumes. This can be compared to an electron density of $10^{-6} e^-/cm^3$ for Earth's magnetic field. Thus, Jupiter's environment has an electron density of about 10^3 that of Earth.

Figures A-3 through A-6 summarize the estimates of Jupiter's trapped electron radiation field. Energy spectra for two values of γ in equation (8) are shown in Figure A-3. Figures A-4 and A-5 present the flux distribution as a function of energy and planetary radii out from Jupiter's center. The curves are shown only out to 5.3 Jupiter radii; however, the radiation zones extend farther out into space. An iso-flux map of the Jupiter-trapped radiation is shown in Figure A-6 while Earth-trapped radiation is shown in Figure B-9 (Appendix B).

VISUAL SURFACE

Telescopic observations of Jupiter do reveal some details of appearance of the visual surface and offers some clues to its makeup and the forces acting on it. Perhaps the best description of the planetary surface as seen from Earth is given by Peek [Ref. A-27].

The visual surface of Jupiter can be divided into alternating dark and light bands running parallel to the equator. The dark bands between two parallels of latitude are called belts while the light bands are known as zones.

The main zones and belts have been named according to their location on the planet's northern and southern hemispheres. There is a broad equatorial zone, bounded by north and south tropical belts which are followed by north and south tropical zones, respectively. There is then a temperate belt, a temperate zone, another temperate belt, and finally a polar region in each hemisphere.

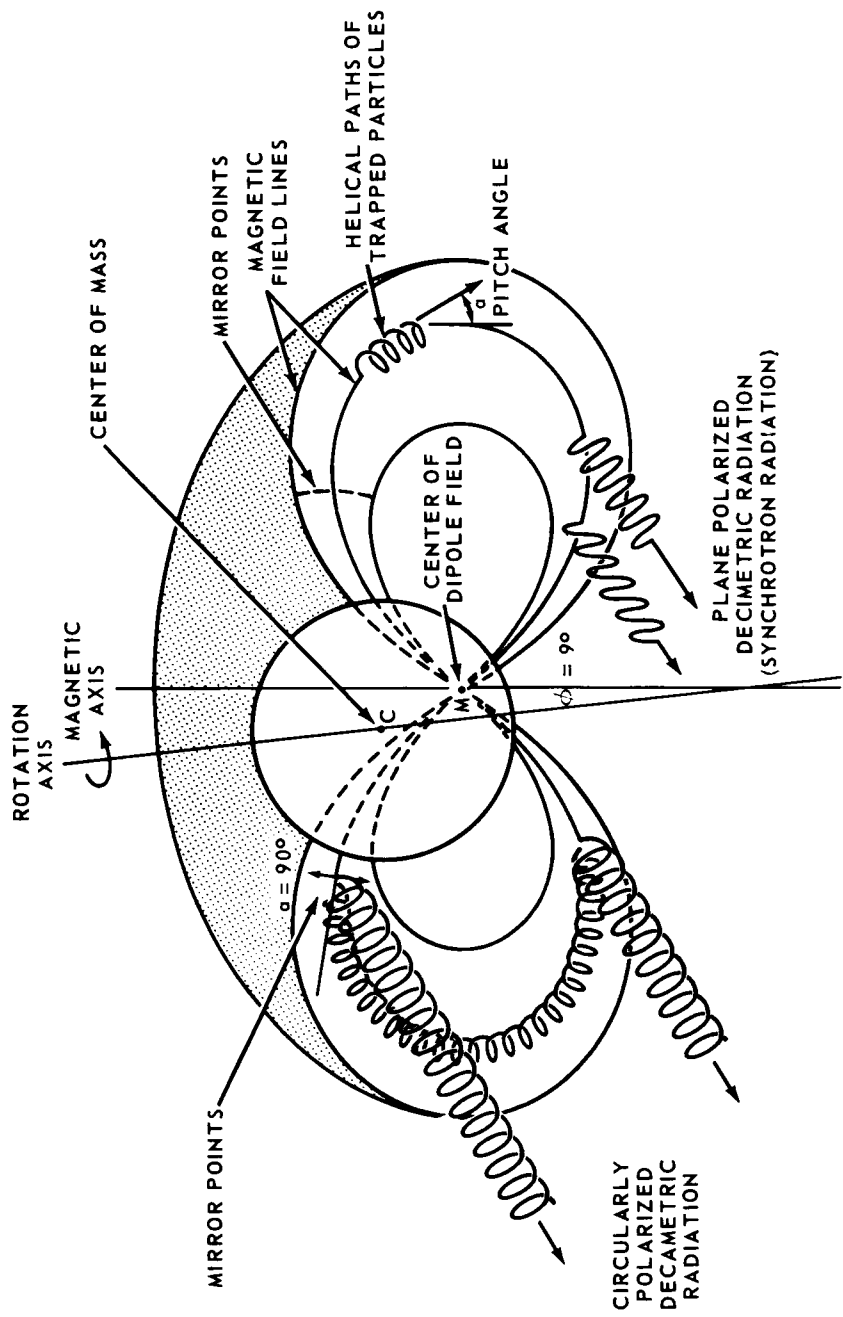


FIGURE A-2. THE OFF-CENTER RADIATION BELTS OF JUPITER

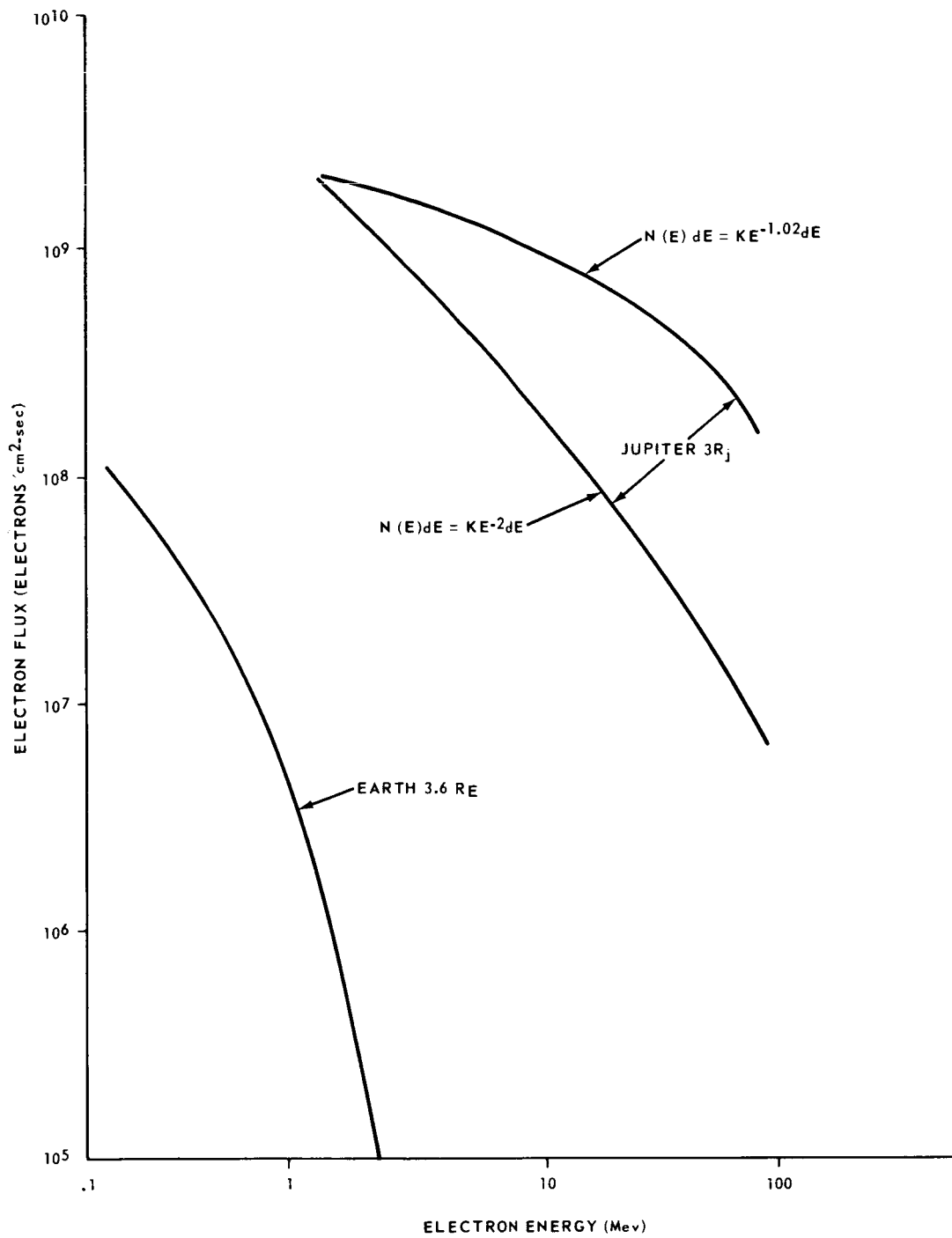


FIGURE A-3. INTEGRATED ELECTRON FLUX FOR EARTH AND JUPITER

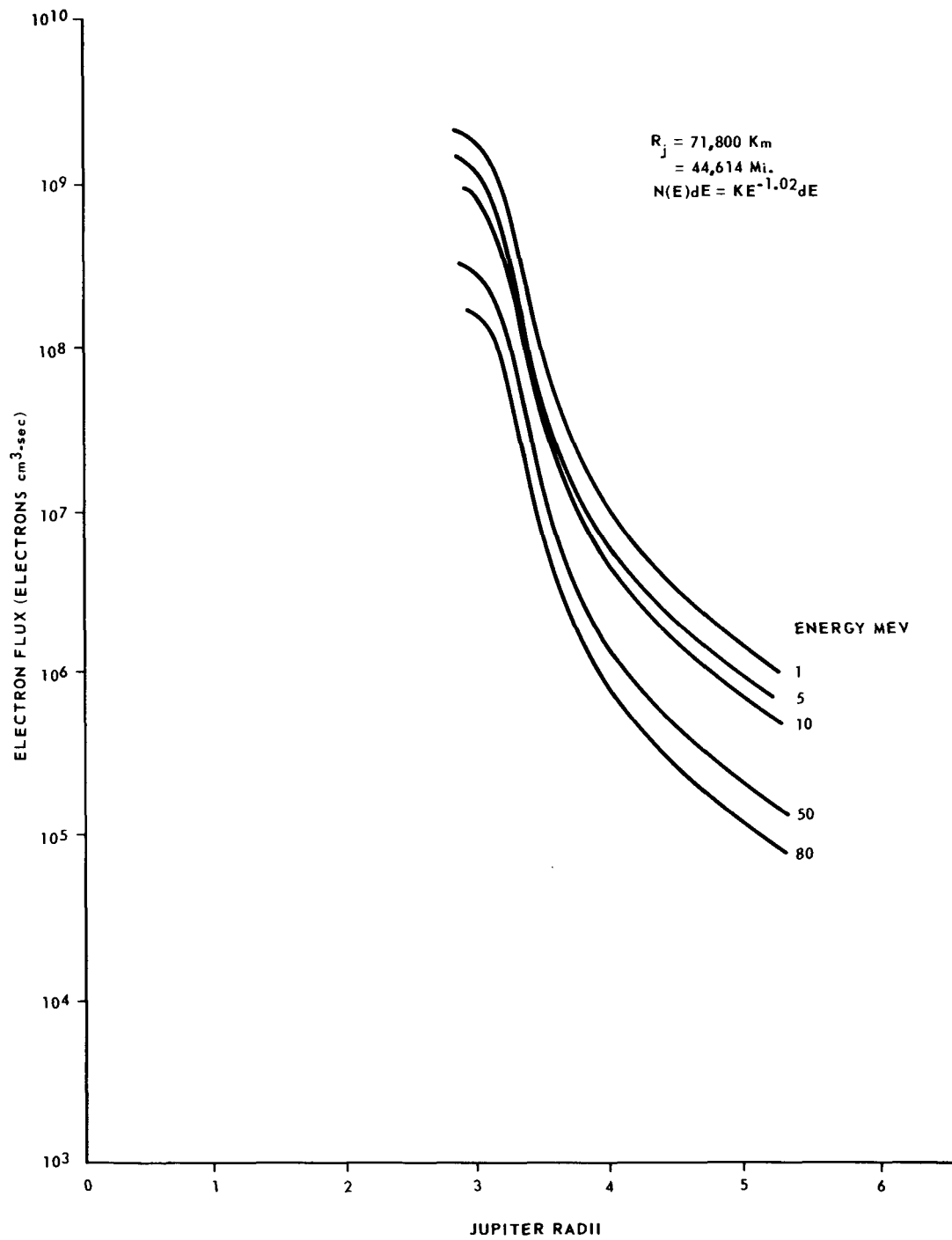


FIGURE A-4. JUPITER INTEGRATED ELECTRON FLUX
FOR $\gamma = 1.02$

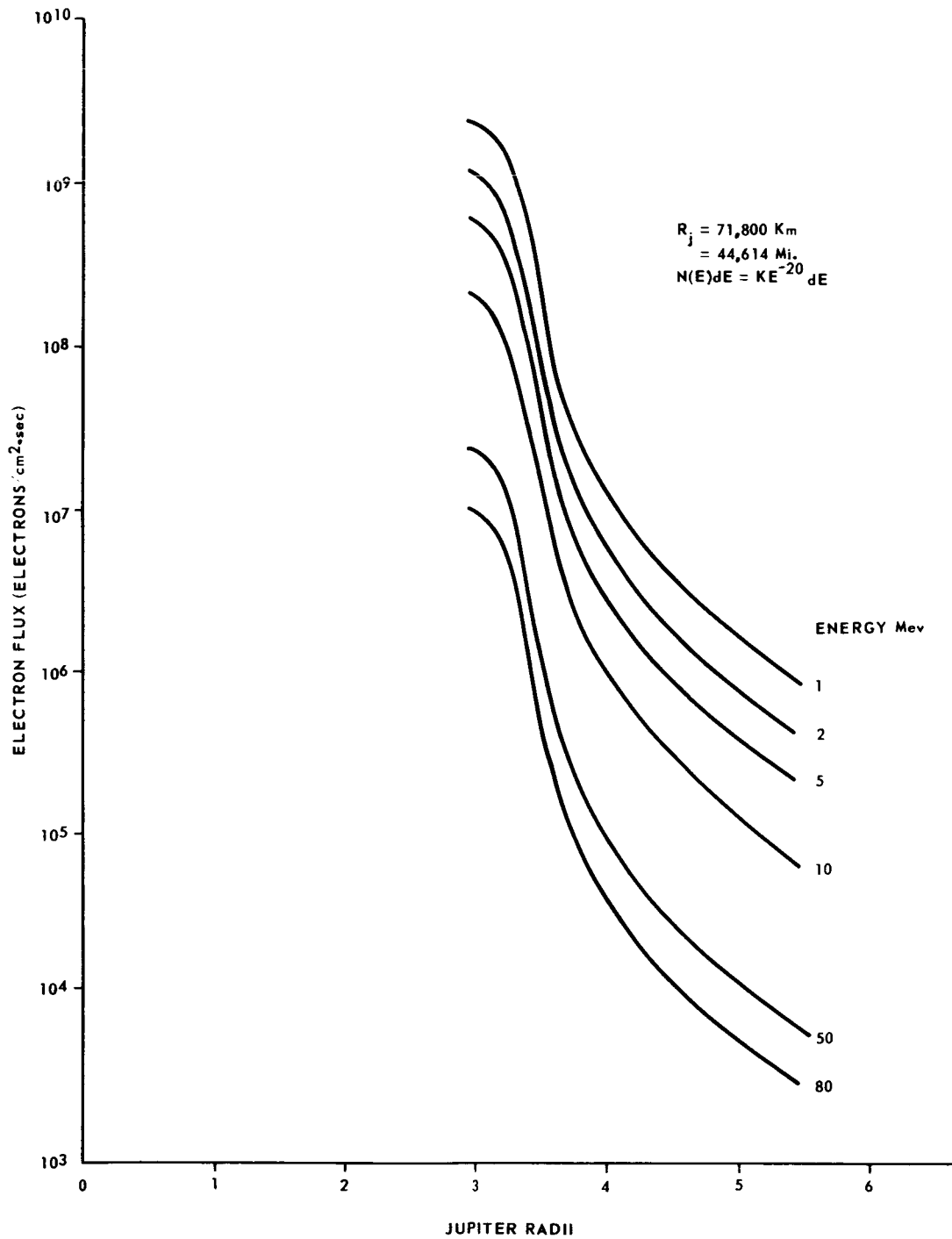
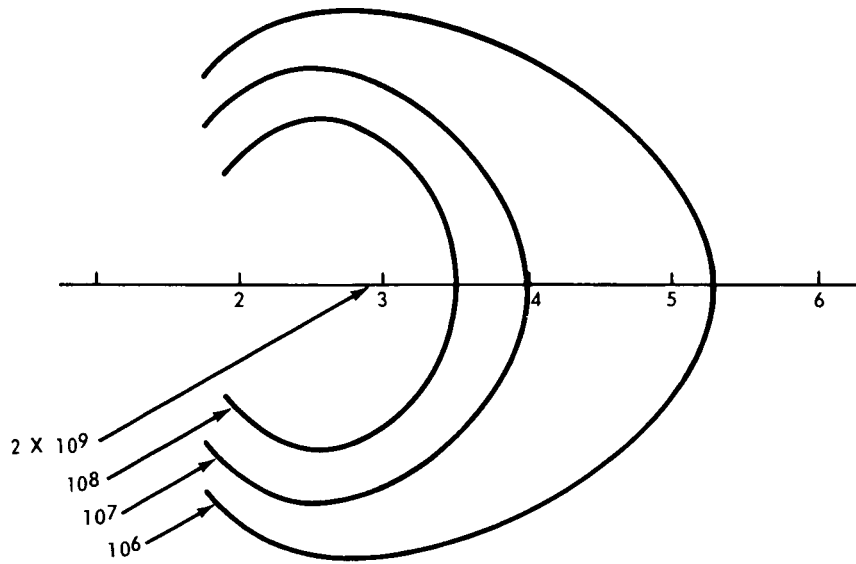


FIGURE A-5. JUPITER INTEGRATED ELECTRON FLUX FOR $\gamma = 2.0$

RADIAL DISTANCE IN JUPITER RADII



ELECTRON FLUX [ELECTRONS $\text{cm}^2\text{-sec}$ ($E > 1 \text{ Mev}$)]

FIGURE A-6. JUPITER TRAPPED RADIATION ISO-FLUX MAP

These cloud bands are by no means regular or constant in form. While most of the markings on Jupiter's surface change fairly quickly, some markings are more permanent and last from months to many years with varying intensity. One of the most striking feature is an oval area, lying mainly in the south tropical zone, called the Great Red Spot. These observed features are manifestations of the general circulation of the Jovian atmosphere. The nomenclature of the Jovian belts, zones, and associated visual surface currents, as adopted by the British Astronomical Association, is shown in Figure A-7.

There also exists many irregularly distributed smaller features within the belts and zones. These consist of an assortment of markings in the form of streaks, wisps, arches, loops, and patches of either darker or lighter material. The more or less permanent "surface currents" or "drifts" are included in Figure A-7.

The belts are usually gray in color but can exhibit great variability in tones of subdued reds and blues. The zones generally appear pale yellow or creamy white, the polar regions gray, and the Great Red Spot is red. Rice [Ref. A-28, A-29, and A-30] partially explains this coloration by the absorption of ultraviolet sunlight by the ammonia (NH_3) and methane (CH_4) of Jupiter's atmosphere to form free radicals stabilized in "ices" at low temperatures. The possible transitory radicals are amine (NH_2), imine (NH), hydrazine (NH_2NH), methyl (CH_3), and methylene (CH_2). The colors represented by the free radicals are mostly yellows and blues. Papazian [Ref. A-31] suggested charged-particle bombardment at the tips of the Jovian radiation belts as an explanation of the observed colored bands of Jupiter. Wildt [Ref. A-32] suggests the presence of metallic sodium in liquid or solid ammonia which changes from gray to brown at 161°K and to blue above 195°K . Calcium could account for the complete range of hues from yellow and delicate gold to red and bronze which, perhaps, is an explanation of the color variations of the Great Red Spot. Both sodium and calcium are cosmically abundant, i. e., supplied from comet's trails.

The acceptance of these before mentioned theories on Jupiter's colors is not universal. Several experiments such as Abelsen [Ref. A-33] Heyns, et al., [Ref. A-34], Sagan [Ref. A-35], and Siegel and Guimarro [Ref. A-36], have conducted studies which lead to the conclusion that a Jovian microsphere may exist and the possibility of a form of primitive life on the giant planet is not as remote as anticipated. It has been suggested that some microbial type of life could contribute to Jupiter's colors.

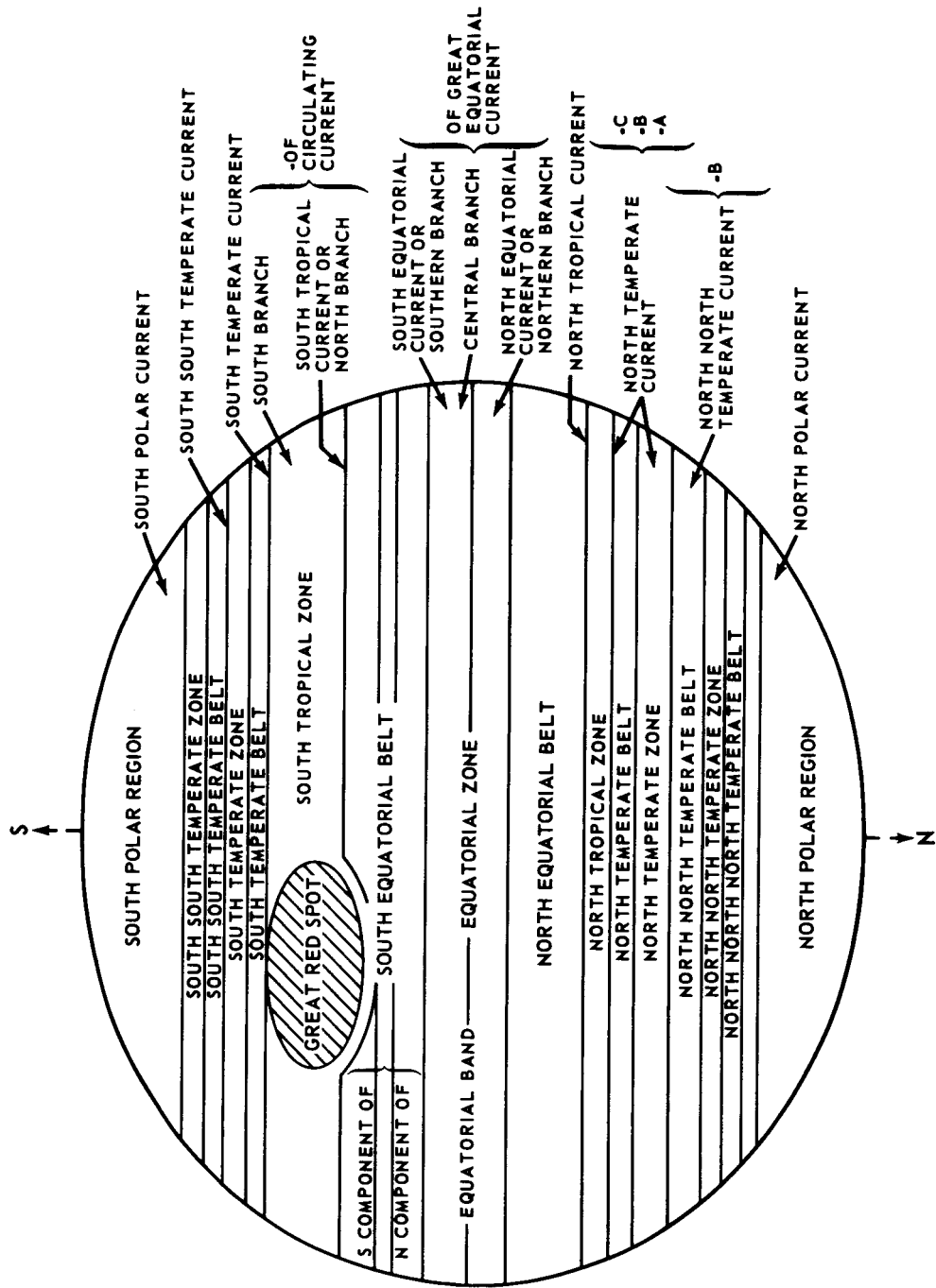


FIGURE A-7. NOMENCLATURE OF JOVIAN BELTS AND ZONES AND ASSOCIATED VISIBLE SURFACE CURRENTS

Hess [Ref. A-37] investigated possible variations in the heights and temperatures of the Jovian ammonia cloud surface. Assuming the cloud layer is to be flat-topped, Hess postulated the surface rises toward the limbs (at 60° from the center of the disk). On the basis of these observations, Squires [Ref. A-38] proposed the existence of large cumuliform equatorial clouds with tops reaching perhaps 20 to 30 kilometers above the main cloud deck.

The Equatorial Zone covers about one-eighth of the planet's surface and straddles the equator but is seldom symmetrical about it. Its latitudinal width averages about 14° and has varied greatly from 17.6° to 11.0° . The intensity of the Equatorial Zone can change from the brightest ever observed on the planet to a deep sombre tone. The planet's rotation separates the zone into three branches: the Northern, Central, and Southern Branches of the Great Equatorial Current. A thin, dusky line known as the Equatorial Band sometimes indistinctly divides the zone within 1° of the true equator. Gray wisps from the North and South Equatorial Belts may curve and merge into fragments of this band.

The most conspicuous belt on Jupiter is the North Equatorial Belt. This wide, dark belt is laced with white spots, humps, and spikes which often develop into gray wisps which, in turn, merge into adjacent zones. It is the most consistently active region of Jupiter, and rotation periods of these spots and currents, the North Equatorial Current and North Tropic Current, are quite variable.

The North Tropical Zone is usually conspicuous and is sometimes the brightest zone of Jupiter. Dark spots and streaks are characteristic along the edges, but occasional white spots are general in the northern half of the zone.

The North Temperate Belt and Zone vary in width and intensity. This zone can be the brightest but it has also been observed to disappear. Large white spots appear at times as do two currents, North Temperate Currents A and C. There is also an intermediate North Temperate Current B. The rotation periods of these currents are relatively slow. Dull colors, mostly grays and blue-grays, are usually associated with the North Temperate Belt.

The North North Temperate Zone is frequently lost in the general north polar shading and seldom displays any feature, such as occasional white spot. The North North Temperate Belt is also not very distinct. It is often broken up into faint and dark fragments and sometimes appears double. A fairly steady current, North North Temperate Current A, was derived from the dark spots.

The North North Temperate Belt and Zone are usually featureless and may not circle the planet.

The North Polar Region has varying duskiness and extends to about 48° N latitude. A North Polar Current apparently exists with a steady drift rate.

The South Equatorial Belt generally consists of two distinct components separated by a wide, bright space similar to a zone. The Great Red Spot is deeply embedded into the southern component of the belt. The belt sometimes has violent outbursts of activity while at other times the southern component may virtually disappear. Although dark projections and light rifts may be present, there are no elongated patches or large white spots which are characteristic of its northern counterpart, the North Equatorial Belt. The spots and wisks sometimes form branches to two currents, the North Circulating Current and the South Equatorial Current. Color of the belt is quite varied. Sometimes gray or gray-blue or, more often, pink with various shades and tints of these.

The South Tropical Zone, although it comprises only 10 degrees of latitude, is the most fascinating region of the planet. Included in it are the permanent Great Red Spot and the sites of the short-lived South Tropical Disturbance, the Circulating Current, the Oscillating Spot, and the Dark South Tropical Streaks. Of these only the Great Red Spot is presently observed. These phenomena produce heavily shaded portions of the zone while the undisturbed portions remain very bright and white.

The Great Red Spot is an enormous oval some 40 000 kilometers long and 13 000 kilometers wide. It has periods of extreme contrast in brightness, and color has been known to fade almost completely. Tints of the Great Red Spot vary to mauve to lilac and peach-blossom. This huge oval wanders erratically and its motion did reverse around 1880.

The South Temperate Belt is narrow but permanent having frequent dark and light spots or sections which are controlled by the steady South Temperate Current. The South Temperate Zone brightness is quite variable and is a creamy yellow or white. The South Temperate Current controls objects of the belt and zone, but the steadier South Temperate Current may dominate the whole region.

The South South Temperate Belt assumes various aspects. Its color is faint and gray with occasional brown tinges. The South South Temperate Zone is not well known but it seems to suffer frequent interruptions. The rotation periods of its spots and markings are comparatively constant. The South South Temperate Current is well determined and prominent and flows steadily over a wide range of latitudes.

The South South South Temperate Belt and Zone is also dependent on the South South Temperatue Current. This belt and zone is immersed in the South Polar Region. This Region is of gray shading but is much higher in latitude than its counterpart, the North Polar Region. Although it is featureless most of the time, its boundary varies greatly.

Finally, Jupiter's colors may be caused by varying chemical composition and heights of particulate matter. Sharonov [Ref. A-39] suggests, however, that the coloration is caused by light scattering in colorless gases and aerosols. The scattering of light in a pure molecular atmosphere will cause the light to become strongly polarized. On the other hand, scattering of light in clouds generally will decrease polarization. The polarization effects in clouds is a function of chemical composition, size, shape, and state of the cloud particles. The atmosphere above clouds will increase polarization.

Polarization of Jupiter is strongest at the gray-colored polar regions and decreases near the equatorial region. This leads to the conclusion that a thin fog with particles of about 1 micron in diameter extends over most of the planet but disappears over the polar regions. A more reasonable interpretation to the photometric data, however, is that Rayleigh scattering is not valid in the atmosphere of Jupiter and that the atmosphere is filled with clouds of solid particulate matter.

ATMOSPHERE COMPOSITION

The most reliable data on the composition of the planet's atmospheres comes from spectroscopy. These data reveal great differences in the atmospheres of terrestrial planets and the Jovian planets. Jupiter's spectra reveals enormous quantities of hydrogen and lessër amounts of ammonia, methane, ethane, acetylene, silane, deuterium hydride, methyl deuteride, hydrogen cyanide, and ethylene. Kuiper [Ref. A-40] theorized that the Jovian atmospheres are chemically reducing while terrestrial atmospheres are oxidizing. Also, the Jovian planets are direct descendants of the protoplanets which were condensations of the original solar nebula and contained, like the sun, a great predominance of hydrogen together with substantial amounts of helium. The theory states that the terrestrial atmospheres are secondary in origin.

The detection of molecular hydrogen by spectrograph was not a simple matter and came only a few years ago even though its presence had long been suspected. The hydrogen molecule (H_2), like the nitrogen molecule (N_2), has no dipole moment and, therefore, displays no ordinary spectrum. The detection of molecular hydrogen was made possible by observations of Herzberg [Ref. A-41]. He noted that molecular hydrogen has a quadrupole moment with possible energy transitions producing a "quadrupole rotation-vibration spectrum"; however, large amounts would have to be present. He even predicted the wave lengths and the approximate strength of the various lines making up the bands expected in the visible and infrared. The highest resolutions are necessary to detect the quadrupole lines for they are exceedingly narrow or sharp and are practically unaffected by pressure boardening.

Kiess, et al., [Ref. A-42] identified four weak lines lying in the near-infrared spectrum of Jupiter. Comparing the strength of these lines to theoretical values, a rough estimate of the amount of molecular hydrogen present can be derived. Several investigators have suggested values which range from about 5 km-atm* of hydrogen above the cloudtop of Jupiter to 270 km-atm. These estimates are based on the underlying assumptions that: (1) the cloudtop is an even spherical reflecting surface, (2) the quadrupole lines are unsaturated, and (3) the temperature along the atmospheric column is constant. The large deviation in the quantity of hydrogen is related to the extent to which these assumptions are employed. An equilibrium rotational temperature of about 170° K. was used in the more abundant estimates and it is possible that the temperature is as high as 230° K, if the clouds form towers rather than a smooth surface.

Perhaps the best estimate concerning the abundance of hydrogen is found in a recent review by Field [Ref. A-43]. Acceptable values are 30 to 80 km-atm of hydrogen with 30 km-atm being the most probable.

The structure of the strong bands of Jovian spectra have been carried on for many years. Wildt [Ref. A-44] succeeded in identifying many lines and bands. Kuiper [Ref. A-40] compared these bands with laboratory spectra of pure gases in pipes. Under the assumption that the observed atmosphere of Jupiter is a clear (Rayleigh) layer overlying a reflecting cloudtop, he found values of 7 m-atm of ammonia and 150 m-atm of methane. Since Jupiter's upper atmosphere may not be clear as assumed, in which case scattering may

* The amount of gas in a single vertical column through the atmosphere of the planet is equivalent to 5 kilometers of hydrogen at atmospheric pressure (1 atm STP).

complicate the normal formation of the absorption lines, and reemission (sky luminescence) may be present, these values could be about 10 m-atm of ammonia and about 500 m-atm of methane.

Modern high-dispersion spectrography has resolved the fine structure of Jupiter's orange, red, and near-infrared bands. Wildt [Ref. A-45] considered the ultraviolet photodecomposition of methane and ammonia as well as the stability of the methane and ammonia concentrations. The ultraviolet photodecomposition of these two compounds produces free radicals CH_3 (methyl) and NH_2 (amino), and others, as well as producing secondary chemical reactions such as hydrogenation, recombination, and polymerization.

Several authors have speculated as to possible compounds and free elements that might be present. These include, along with the probable upper limit abundance: acetylene (C_2H_2), 3 m-atm, ethylene (C_2H_4), 2 m-atm, ethane (C_2H_6), 2.5 m-atm, methylamine (CH_3NH_2), hydrogen cyanide (HCH), 2 m-atm, silane (SiH_4), 20 m-atm, methyldeuteride (CH_3D), 20 m-atm, deuterium hydride (HD), 500 m-atm. The concentration of deuterium to hydrogen may be as much as five times that of the terrestrial value because of less escape of deuterium hydride than hydrogen in the early history of Jupiter.

Since the inert gases are known to be abundant in the solar atmosphere, it is expected on cosmological grounds to find an abundance of helium. Jupiter's low mean density (1.6) and its stratospheric mean molecular weight (3 to 4) strongly suggest helium is of the same order of magnitude as abundant as hydrogen. Nitrogen (N_2) in the free state is also suspected to be present, but no upper limit of its abundance has been established. Neon (Ne) and argon (Ar) are also assumed to be present.

The composition of the upper atmosphere leads to speculation of the mean molecular weight, total pressure, and a proposed "working" atmosphere. Spinrad and Trafton [Ref. A-46] used a hydrogen abundance of 27 km-atm, a total pressure of 2.8 atmospheres, and a mean molecular weight of 3.4 to present the composition in Table A-4. The major gas hydrogen, at about 60 percent of the total, followed by helium, at about 36 percent in this composition, is similar to that of the sun and stars.

A further comment might be in order on the total pressure used in Table A-4. Speculations on the optical properties of Jupiter's disk coupled with Baum and Code [Ref. A-47] star occultation results lead to a total pressure at cloudtop of about 13 atmospheres. All this discrepancy indicates the great uncertainties in the data and in the assumptions made.

TABLE A-4. PROBABLE ATMOSPHERIC COMPOSITION *

<u>Gases in the visible Jovian atmosphere</u>	<u>Molecular Weight</u>	<u>Abundance Percent</u>	<u>Abundance km-atm</u>
Hydrogen (H ₂)	2	60	27
Helium (He)	4	36	16
Neon (Ne)	20	3	0.7
Methane (CH ₄)	16	1	0.2
Ammonia (NH ₃)			

* Based on mean molecular weight = 3.4
total pressure = 2.8 atm
hydrogen abundance 27 km-atm

ATMOSPHERIC AND INTERNAL STRUCTURE

The atmospheric structure of Jupiter can conveniently be divided into an upper atmosphere and a lower atmosphere separated by the visible cloud-top or visible surface. Present data suggest a hot interior and deep atmosphere which is unlike the classical view of Jupiter's being a cold planet with a relatively shallow atmosphere.

Several models have been proposed for the upper atmosphere. These are based on available radiometric (temperature) and spectral (chemical composition) data. Gross and Rasool [Ref. A-48] have proposed two extreme models based on the two values of the hydrogen to helium mixing ratio which were 20 to 1 by Urey [Ref. A-49] and 0.03 to 1 by Opik [Ref. A-3]. The former will be Model I while the latter is Model II. Smith and Vaughan in NASA TM X-53521 [Ref. A-50] report these models with the following specifications:

Model I

Temperature - visible surface to 187 km

$$T = 153 (1/2)^{1/4} (1 + e^{-z/2.251795 \times 10^6})^{1/4} \text{ } ^\circ\text{K} - 187 \text{ to } 350 \text{ km}$$

$$T = 128.69 + (z - 1.87 \times 10^7) 6.93988 \times 10^{-7} \text{ } ^\circ\text{K} - 350 \text{ to } 500 \text{ km}$$

$$T = 140^{\circ}\text{K}$$

Molecular Weight - surface to 187 km

$$M = 2.2 - 187 \text{ to } 200 \text{ km}$$

$$M = 2.2 - (z - 1.87 \times 10^7) 5.3846 \times 10^{-7} - 200 \text{ to } 500 \text{ km}$$

$$M = 1.5$$

Pressure - cloudtop

$$P = 3 \text{ atm}$$

Model II

Temperature - visible surface to 104 km

$$T = 153 (1/2)^{1/4} (1 + e^{-z/1.1840026 \times 10^6})^{1/4} \text{ }^{\circ}\text{K} - 104 \text{ to } 224 \text{ km}$$

$$T = 128.68 (z - 1.04 \times 10^7) 5.269 \times 10^{-7} \text{ }^{\circ}\text{K} - 224 \text{ to } 500 \text{ km}$$

$$T = 135^{\circ}\text{K}$$

Molecular Weight - surface to 104 km

$$M = 3.95 - 104 \text{ to } 120 \text{ km}$$

$$M = 3.95 - (z - 1.04 \times 10^7) 1.53125 \times 10^{-6} - 120 \text{ to } 500 \text{ km}$$

$$M = 1.5$$

Pressure - cloudtop

$$P = 3 \text{ atm}$$

Where: T is temperature in degrees Kelvin

M is grams per gram mole

z is in centimeters

p is pressure in atmospheres

Table A-5 shows a summary of these data for the two models for the upper atmosphere of Jupiter, i. e., above the cloudtop. These data were computed using the hydrostatic equation, the equation of state, and the work of Gross and Rasvol [Ref. A-46].

TABLE A-5. TWO ATMOSPHERIC MODELS OF
JUPITER'S UPPER ATMOSPHERE

z (km)	Density (gm/cm ³)		Temperature (° K)		Pressure (dynes/cm ²)	
	Model I	Model II	Model I	Model II	Model I	Model II
0	5.188x10 ⁻⁴	9.315x10 ⁻⁴	153	153	3.000x10 ⁶	3.000x10 ⁶
1	5.004x10 ⁻⁴	8.733x10 ⁻⁴	152	151	2.878x10 ⁶	2.784x10 ⁶
2	4.825x10 ⁻⁴	8.177x10 ⁻⁴	151	150	2.760x10 ⁶	2.581x10 ⁶
3	4.651x10 ⁻⁴	7.647x10 ⁻⁴	151	149	2.646x10 ⁶	2.391x10 ⁶
4	4.481x10 ⁻⁴	7.144x10 ⁻⁴	150	147	2.537x10 ⁶	2.213x10 ⁶
5	4.316x10 ⁻⁴	6.666x10 ⁻⁴	149	146	2.431x10 ⁶	2.048x10 ⁶
6	4.156x10 ⁻⁴	6.214x10 ⁻⁴	148	145	2.329x10 ⁶	1.893x10 ⁶
7	4.000x10 ⁻⁴	5.786x10 ⁻⁴	148	144	2.232x10 ⁶	1.749x10 ⁶
8	3.849x10 ⁻⁴	5.382x10 ⁻⁴	147	143	2.137x10 ⁶	1.615x10 ⁶
9	3.703x10 ⁻⁴	5.001x10 ⁻⁴	146	142	2.047x10 ⁶	1.491x10 ⁶
10	3.561x10 ⁻⁴	4.644x10 ⁻⁴	143	141	1.960x10 ⁶	1.375x10 ⁶
15	2.915x10 ⁻⁴	3.165x10 ⁻⁴	143	137	1.572x10 ⁶	9.119x10 ⁵
20	2.370x10 ⁻⁴	2.119x10 ⁻⁴	140	134	1.256x10 ⁶	5.988x10 ⁵
25	1.915x10 ⁻⁴	1.401x10 ⁻⁴	138	132	9.999x10 ⁵	3.904x10 ⁵
30	1.539x10 ⁻⁴	9.177x10 ⁻⁵	136	131	7.934x10 ⁵	2.533x10 ⁵
35	1.231x10 ⁻⁴	5.971x10 ⁻⁵	135	130	6.279x10 ⁵	1.638x10 ⁵
40	9.805x10 ⁻⁵	3.868x10 ⁻⁵	134	130	4.957x10 ⁵	1.056x10 ⁵
45	7.783x10 ⁻⁵	2.498x10 ⁻⁵	133	129	3.907x10 ⁵	6.803x10 ⁴
50	6.161x10 ⁻⁵	1.610x10 ⁻⁵	132	129	3.074x10 ⁵	4.377x10 ⁴
60	3.834x10 ⁻⁵	6.667x10 ⁻⁶	131	129	1.896x10 ⁵	1.808x10 ⁴
70	2.370x10 ⁻⁵	2.753x10 ⁻⁶	130	129	1.165x10 ⁵	7.461x10 ³
80	1.459x10 ⁻⁵	1.136x10 ⁻⁶	130	129	7.144x10 ⁴	3.077x10 ³
90	8.954x10 ⁻⁶	4.684x10 ⁻⁷	129	129	4.373x10 ⁴	1.269x10 ³
100	5.485x10 ⁻⁶	1.931x10 ⁻⁷	129	129	2.675x10 ⁴	5.229x10 ²

TABLE A-5. TWO ATMOSPHERIC MODELS OF
JUPITER'S UPPER ATMOSPHERE (Continued)

<u>z (km)</u>	<u>Density (gm/cm³)</u>		<u>Temperature (°K)</u>		<u>Pressure (dynes/cm²)</u>	
	Model I	Model II	Model I	Model II	Model I	Model II
110	3.355x10 ⁻⁶	6.474x10 ⁻⁸	129	129	1.635x10 ⁴	2.292x10 ²
120	2.051x10 ⁻⁶	1.928x10 ⁻⁸	129	130	9.986x10 ³	1.384x10 ²
130	1.253x10 ⁻⁶	1.375x10 ⁻⁸	129	130	6.099x10 ³	9.912x10 ¹
140	7.655x10 ⁻⁷	9.824x10 ⁻⁹	129	131	3.724x10 ³	7.110x10 ¹
150	4.675x10 ⁻⁷	7.028x10 ⁻⁹	129	131	2.74x10 ³	5.107x10 ¹
160	2.854x10 ⁻⁷	5.034x10 ⁻⁹	129	132	1.388x10 ³	3.673x10 ¹
170	1.743x10 ⁻⁷	3.611x10 ⁻⁹	129	132	8.474x10 ²	2.645x10 ¹
180	1.064x10 ⁻⁷	2.593x10 ⁻⁹	129	133	5.173x10 ²	1.907x10 ¹
190	6.035x10 ⁻⁸	1.865x10 ⁻⁹	129	133	3.173x10 ²	1.377x10 ¹
200	2.977x10 ⁻⁸	1.343x10 ⁻⁹	130	134	2.138x10 ⁻²	9.956
225	1.281x10 ⁻⁸	5.946x10 ⁻¹⁰	131	135	9.327x10 ¹	4.449
250	5.576x10 ⁻⁹	2.667x10 ⁻¹⁰	133	135	4.112x10 ¹	1.996
275	2.453x10 ⁻⁹	1.196x10 ⁻¹⁰	135	135	1.833x10 ¹	8.950x10 ⁻¹
300	1.090x10 ⁻⁹	5.364x10 ⁻¹¹	137	135	8.251	4.014x10 ⁻¹
325	4.897x10 ⁻¹⁰	2.406x10 ⁻¹¹	138	135	3.753	1.800x10 ⁻¹
350	2.221x10 ⁻¹⁰	1.079x10 ⁻¹¹	140	135	1.724	8.075x10 ⁻²
375	1.025x10 ⁻¹⁰	4.840x10 ⁻¹²	140	135	7.956x10 ⁻¹	3.622x10 ⁻²
400	4.732x10 ⁻¹¹	2.171x10 ⁻¹²	140	135	3.672x10 ⁻¹	1.624x10 ⁻²
425	2.184x10 ⁻¹¹	9.736x10 ⁻¹³	140	135	1.695x10 ⁻¹	7.285x10 ⁻³
450	1.008x10 ⁻¹¹	4.367x10 ⁻¹³	140	135	7.822x10 ⁻²	3.267x10 ⁻³
475	4.652x10 ⁻¹²	1.958x10 ⁻¹³	140	135	3.610x10 ⁻²	1.466x10 ⁻³
500	2.147x10 ⁻¹²	8.784x10 ⁻¹⁴	140	136	1.666x10 ⁻²	6.573x10 ⁻⁴

In both models the vertical temperature gradient above the clouds was calculated on the basis of radiative equilibrium and a gray atmosphere* from the simplified radiative transfer equation:

$$T_z^4 = T_e^4 (1/2 + 3/4 \tau_z) \quad (9)$$

Where: T_z is the temperature at any level z

T_e is the effective blackbody temperature of the planet

τ_z is the average optical thickness above level z

Taking the optical thickness (opacity) at cloudtop level, $z = 0$, to be τ_0 , the total optical thickness at any level is given by

$$\tau_z = \tau_0 - e^{-z/h} \quad (10)$$

Where: H is the total scale height. The optical thickness found was

$$\tau_0 = 0.66.$$

A more recent, more complete model of the upper atmosphere was developed at the Marshall Space Flight Center, Huntsville, Alabama, and is summarized in Table A-6. The planetary atmosphere development program uses assumed temperature profile, molecular weight profile, and surface pressure as well as the following constants as input:

Planet radius = 69 000 km

Boltzmann's constant = 1.380259×10^{-16}

Coefficient of viscosity constants:

Beta = 1.458×10^{-6}

Sutherland = 110.40

Speed of sound constant = 1.410

Universal gas constant = 8.31438994×10^7

* A gray atmosphere is one whose radiation absorption is independent of wavelength.

TABLE A-6. MODEL OF JOVIAN UPPER ATMOSPHERE

<u>Geometric Altitude (km)</u>	<u>Geopotential Height (G/AM)</u>	<u>Kinetic Tem- perature (°K)</u>	<u>Molecular Tem- perature (°K)</u>	<u>Molecular Wt. (unit less)</u>
0	0.0	153.00	153.00	2.2
2	2.0	151.86	151.87	2.2
4	4.0	150.73	150.73	2.2
6	6.0	149.60	149.60	2.2
8	8.0	148.47	148.47	2.2
10	10.0	147.33	147.33	2.2
20	19.99	141.67	141.67	2.2
30	29.99	136.01	136.01	2.2
40	39.98	134.34	134.34	2.2
50	49.96	132.67	132.67	2.2
60	59.95	131.01	131.01	2.2
70	69.93	130.34	130.03	2.2
80	79.91	129.67	129.67	2.2
90	89.88	129.01	129.00	2.2
100	99.86	129.00	129.00	2.2
120	119.79	129.00	129.00	2.2
140	139.72	129.00	129.00	2.2
160	159.63	129.00	129.00	2.2
180	179.53	129.00	129.00	2.2
200	199.42	130.16	188.21	1.53
300	298.70	136.91	200.80	1.5
400	397.69	140.00	205.33	1.5
500	496.40	140.00	205.33	1.5
600	594.83	284.14	416.74	1.5
700	692.97	433.31	635.53	1.5
800	790.83	582.06	853.69	1.5
900	888.41	730.39	1071.23	1.5
1000	985.71	878.28	1288.15	1.5

TABLE A-6. MODEL OF UPPER JOVIAN ATMOSPHERE
(Continued)

<u>Geometric Altitude (km)</u>	<u>Pressure (dynes/cm²)</u>	<u>Density (g/cm³)</u>	<u>Pressure Scale Height (km)</u>	<u>Density Scale Height (km)</u>
0	3.00x10 ⁶	5.188x10 ⁻⁴	22.77	24.86
2	2.747x10 ⁶	4.785x10 ⁻⁴	22.60	24.68
4	2.513x10 ⁶	4.412x10 ⁻⁴	22.43	24.50
6	2.298x10 ⁶	4.065x10 ⁻⁴	22.26	24.31
8	2.099x10 ⁶	3.743x10 ⁻⁴	22.09	24.13
10	1.917x10 ⁶	3.444x10 ⁻⁴	21.93	23.95
20	1.205x10 ⁶	2.249x10 ⁻⁴	21.09	23.03
30	7.425x10 ⁵	1.445x10 ⁻⁴	20.25	21.43
40	4.518x10 ⁵	8.899x10 ⁻⁵	20.01	20.52
50	2.733x10 ⁵	5.451x10 ⁻⁵	19.77	20.27
60	1.643x10 ⁵	3.318x10 ⁻⁵	19.53	19.88
70	9.832x10 ⁴	1.996x10 ⁻⁵	19.43	19.63
80	5.896x10 ⁴	1.198x10 ⁻⁵	19.34	19.53
90	3.495x10 ⁴	7.169x10 ⁻⁶	19.26	19.53
100	2.079x10 ⁴	4.265x10 ⁻⁶	19.25	19.25
120	7.358x10 ³	1.501x10 ⁻⁶	19.26	19.26
140	2.606x10 ³	5.345x10 ⁻⁷	19.27	19.27
160	9.233x10 ²	1.893x10 ⁻⁷	19.28	19.28
180	3.274x10 ²	6.715x10 ⁻⁸	19.29	19.27
200	1.303x10 ²	1.832x10 ⁻⁸	28.16	16.65
300	4.315	5.687x10 ⁻¹⁰	30.14	29.69
400	1.644x10 ⁻¹	2.118x10 ⁻¹¹	30.90	30.91
500	6.497x10 ⁻³	8.373x10 ⁻¹³	31.00	30.99
600	6.837x10 ⁻¹	4.340x10 ⁻¹¹	63.09	47.37
700	1.916x10 ⁻¹	7.976x10 ⁻¹⁵	96.48	72.45
800	7.896x10 ⁻⁵	2.439x10 ⁻¹⁵	129.98	97.60
900	3.969x10 ⁻⁵	9.805x10 ⁻¹⁶	163.57	122.8
1000	2.277x10 ⁻⁵	4.676x10 ⁻¹⁶	197.26	148.13

TABLE A-6. MODEL OF UPPER JOVIAN ATMOSPHERE
(Continued)

<u>Geometric Altitude (km)</u>	<u>Speed of Sound (m/sec)</u>	<u>Gravity (m/sec²)</u>
0	902.94	25.400
2	899.59	25.398
4	896.23	25.397
6	892.85	25.395
8	889.46	25.394
10	886.46	25.394
20	868.86	25.385
30	851.32	25.378
40	846.08	25.371
50	840.82	25.636
60	835.53	25.356
70	833.39	25.349
80	831.26	25.341
90	829.13	25.334
100	829.10	25.326
120	829.10	25.312
140	829.10	25.297
160	829.10	25.282
180	829.10	25.268
200	1000.15	25.254
300	1034.43	25.181
400	1046.03	25.108
500	1046.03	25.036
600	1490.20	24.964
700	1840.26	24.892
800	2132.87	24.821
900	2389.22	24.750
1000	2619.98	24.679

TABLE A-6. MODEL OF UPPER JOVIAN ATMOSPHERE
(Continued)

<u>Geometric Altitude (km)</u>	<u>Number Density (/cm³)</u>	<u>Atmospheric Mean Free Path (m)</u>	<u>Coefficient of Vis- cosity (kg/m-sec)</u>	<u>Columnar Mass (g/cm²)</u>
0	1.421x10 ²⁰	1.189x10 ⁻⁷	1.048x10 ⁻⁵	1.181x10 ³
2	1.310x10 ²⁰	1.289x10 ⁻⁷	1.040x10 ⁻⁵	1.081x10 ⁻³
4	1.208x10 ²⁰	1.399x10 ⁻⁷	1.033x10 ⁻⁵	9.896x10 ²
6	1.113x10 ²⁰	1.518x10 ⁻⁷	1.026x10 ⁻⁵	9.049x10 ²
8	1.025x10 ²⁰	1.649x10 ⁻⁷	1.018x10 ⁻⁵	8.269x10 ²
10	9.429x10 ¹⁹	1.792x10 ⁻⁷	1.012x10 ⁻⁵	7.552x10 ²
20	6.160x10 ¹⁹	2.743x10 ⁻⁷	9.753x10 ⁻⁶	4.745x10 ²
30	3.955x10 ¹⁹	4.272x10 ⁻⁷	9.385x10 ⁻⁶	2.926x10 ²
40	2.437x10 ¹⁹	6.934x10 ⁻⁷	9.276x10 ⁻⁶	1.781x10 ²
50	1.492x10 ¹⁹	1.132x10 ⁻⁶	9.166x10 ⁻⁶	1.078x10 ²
60	9.085x10 ¹⁸	1.859x10 ⁻⁶	9.056x10 ⁻⁶	6.479x10 ¹
70	5.465x10 ¹⁸	3.092x10 ⁻⁶	9.019x10 ⁻⁶	3.879x10 ¹
80	3.279x10 ¹⁸	5.153x10 ⁻⁶	8.967x10 ⁻⁶	2.316x10 ¹
90	1.963x10 ¹⁸	8.608x10 ⁻⁶	8.923x10 ⁻⁶	1.379x10 ¹
100	1.167x10 ¹⁸	1.447x10 ⁻⁵	8.923x10 ⁻⁶	8.209
120	4.132x10 ¹⁷	4.089x10 ⁻⁵	8.923x10 ⁻⁶	2.907
140	1.463x10 ¹⁷	1.155x10 ⁻⁴	8.923x10 ⁻⁶	1.030
160	5.186x10 ¹⁶	3.259x10 ⁻⁴	8.923x10 ⁻⁶	3.652x10 ⁻¹
180	1.838x10 ¹⁶	9.191x10 ⁻⁴	8.923x10 ⁻⁶	1.296x10 ⁻¹
200	5.015x10 ¹⁵	2.345x10 ⁻³	1.261x10 ⁻⁵	5.159x10 ⁻²
300	1.558x10 ¹⁴	7.399x10 ⁻²	1.333x10 ⁻⁵	1.714x10 ⁻³
400	5.800x10 ¹²	1.986	1.359x10 ⁻⁵	6.547x10 ⁻⁵
500	2.292x10 ¹¹	5.025x10 ¹	1.359x10 ⁻⁵	2.595x10 ⁻⁶
600	1.188x10 ¹⁰	9.693x10 ²	2.353x10 ⁻⁵	2.739x10 ⁻⁷
700	2.184x10 ⁹	5.276x10 ³	3.132x10 ⁻⁵	7.696x10 ⁻⁸
800	6.678x10 ⁸	1.725x10 ⁴	3.772x10 ⁻⁵	3.170x10 ⁻⁸
900	2.685x10 ⁸	4.292x10 ⁴	4.326x10 ⁻⁵	1.604x10 ⁻⁸
1000	1.281x10 ⁸	8.998x10 ⁴	4.819x10 ⁻⁵	9.225x10 ⁻⁹

Avogadro number = 6.022570×10^{26}

Mean air molecule collision diameter = 3.650×10^{-8}

Geopotential height = 0.60

Pressure = 3.00×10^6 millibars

Kinetic temperature = 153.00°K

Gravity = 2.540×10^3

Molecular weight = 2.200

Since this model presents more extensive coverage and is between the previous two models, it is considered to be the best approximation.

The lower atmosphere has much more uncertainty associated with it than does the upper atmosphere for the obvious reason that it is obscured by the clouds. Gallet's [Ref. A-51] model, supplemented by Peeble's [Ref. A-53] calculations, is somewhat reminiscent of semi-stellar atmospheres, being deep and hot at the base. Figure A-8 shows a cross section of this model.

Hydrogen, helium, neon, water, ammonia, and methane are the main chemical constituents. The ammonia and water form a succession of clouded and clear layers whose vapor saturation is controlled by the prevalent atmospheric pressure and temperature. Descending from the visible cloudtop, the layers are as follows: ammonia crystal clouds, ammonia droplet clouds, unsaturated ammonia-vapor clear region, water (ice) crystal clouds, water droplet clouds, unsaturated water-vapor clear region, and the surface of the planet.

Gallet assumed a cloudtop temperature of 150°K and pressure of 1 atmosphere. The temperature at the planet's surface will be dependent upon the amount of ammonia present, a higher temperature indicating a less amount of ammonia. Gallet also assumed a mixing ratio of ammonia (in the higher cold layer) to be decidedly greater than that of nitrogen in the sun and predicts a planet surface temperature of 400°K .

The composition of the liquid and solid portions of Jupiter are dependent on several quantities. These include the known planetary parameters such as the mass, radius, and the second and fourth-harmonic coefficients of the gravitational field, as well as reasonable cosmogonic arguments on the chemical composition and an assumed equation of state of the planetary material. The equation of state is based on experimental data at high pressure extrapolated to the much higher pressures existing on Jupiter.

Several investigators developed models of the internal structure based mainly on an equation of hydrogen. DeMarcus [Ref. A-54] assumed a hydrogen model and compared the Jovian planets to pure hydrogen planets and pure hydrogen white dwarfs. The density of Jupiter differs from that of a pure hydrogen planet by a factor of less than two. Peebles [Ref. A-59] extended DeMarcus's calculations to include the effect of varying the helium abundance over a wide range to investigate the different assumptions of depth, temperature, density of the atmosphere, and various harmonic coefficients of the gravitational field.

All acceptable models have percentages by weight of hydrogen greater than 75 percent. Also, according to Peebles, satisfactory models of Jupiter can be obtained by assuming either a very deep or a very shallow atmosphere. Figure A-8 shows the Gallet and Peebles Jovian interior and Table A-7 is Peeble's model planet for Jupiter. This model assumes an adiabatic atmosphere, 3 atmospheres pressure and 150° K at the visible surface, and a hydrogen abundance of 0.80 in the material above the core. The Peeble's model, however, is most consistent with Jupiter's data has a cloudtop of 150° K and 1 atmosphere and the surface at about 2000° K and 200 000 atmosphere with hydrogen abundance of about 76 percent by mass and a helium abundance of 22 percent by mass.

It is generally accepted that the lower atmosphere is very thick (on the order of 1000 km). Thus, a high probability exists that because of the intense Jovian gravity and accumulated weight of the atmosphere that there is a gradual transition between gaseous, liquid, and solid phases with an ill-defined oceanic interface at the bottom of the atmosphere. It is not clear if continents or icebergs of solidified substances such as hydrogen, water-ice, ammonia-ice, or simple C-H-N compounds exist. The surface may even be slushy because of periodic atmospheric precipitation of ammonia and water and liquid water and methane may be present. Also, some heavier rock-like materials (silicates) might exist in places. It might be noted that it has been suggested that the Great Red Spot overlies a solid continent.

There may exist a relative number of radioactive isotopes in Jupiter's interior. If these are assumed to be at least as large as that of the sun, the radioactive heat flux generated would be sufficient to drive convection in the lower atmosphere. A very rough estimate of the heat flow expected from the decay of the radioactive isotopes (K^{40} , U, Th) results in a very great atmospheric depth consistent with the Gallet and Peebles model.

ATMOSPHERIC CIRCULATION

The complete specification of any hydrodynamical system requires detailed knowledge of the physical properties and chemical composition of the fluid

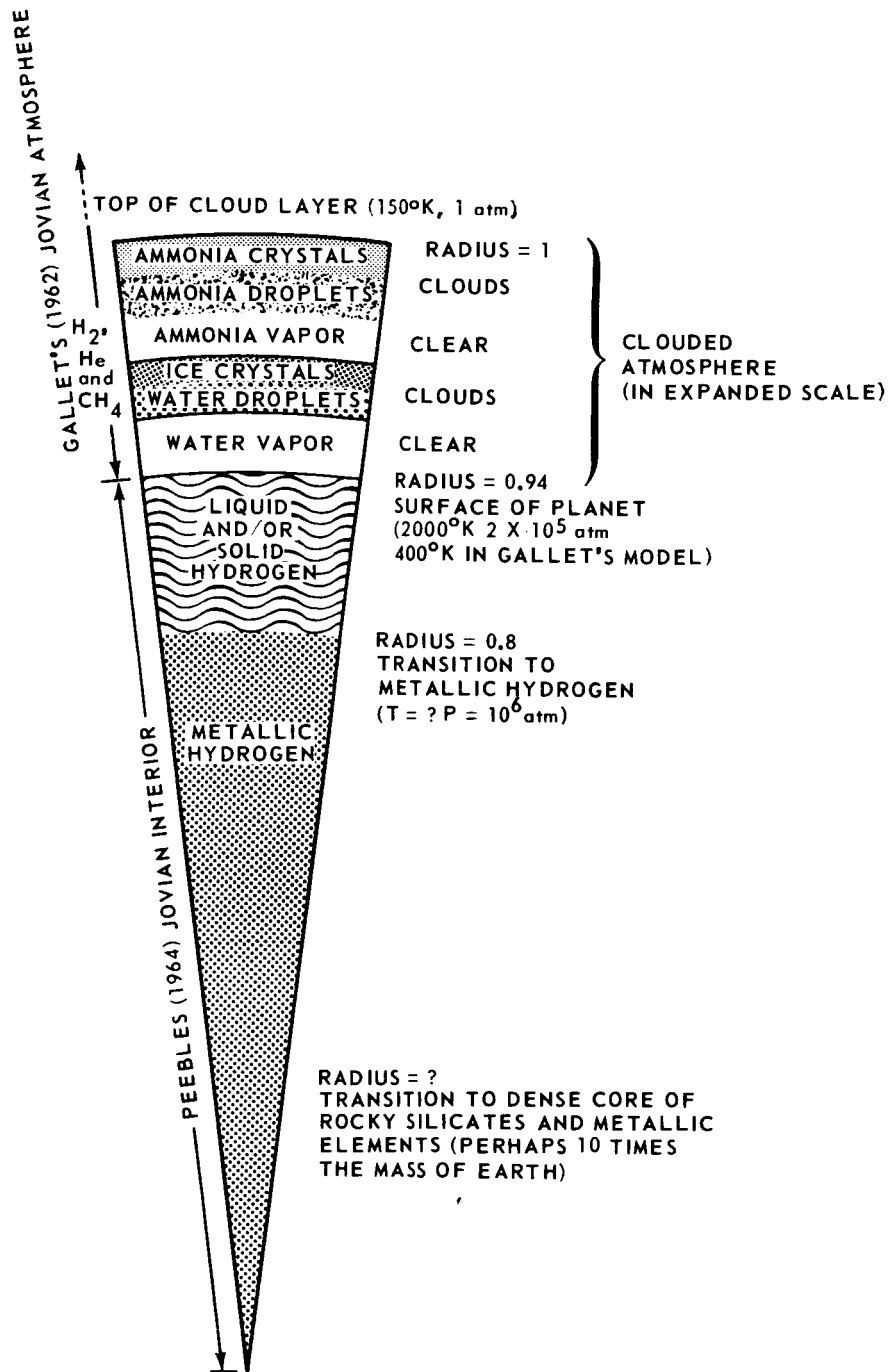


FIGURE A-8. JOVIAN CLOUD LAYERS PROPOSED BY GALLET OVERLYING JOVIAN INTERIOR BY PEEBLES

TABLE A-7. MODEL PLANET FOR JUPITER'S INTERIOR

<u>Relative radius</u> <u>r/R</u>	<u>Pressure, P</u> $\times 10^{12}$ <u>dynes/cm²</u>	<u>Density, P</u> g/cm ³	<u>Relative mass</u>
1.0	3.0×10^{-6}	5.5×10^{-4}	1.0
0.995	3.7×10^{-1}	0.0164	0.99995
0.99	2.8×10^{-3}	0.055	0.9996
0.98	0.020	0.147	0.997
0.96	0.095	0.28	0.988
0.94	0.23	0.40	0.973
0.92	0.38	0.47	0.957
0.9	0.57	0.55	0.941
0.85	1.29	0.76	0.878
0.8	2.2	0.96	0.815
0.75	3.5	1.39	0.74
0.7	5.2	1.63	0.64
0.65	7.2	1.84	0.55
0.6	9.5	2.1	0.46
0.55	11.9	2.3	0.38
0.5	15.0	2.5	0.30
0.4	20.5	2.9	0.19
0.3	26.0	3.3	0.11
0.2	34.0	3.7	0.05

as well as geometry of the system and the nature and distribution of the energy sources. Even if these were well known a complete solution of the mathematical equations, such as the Navier-Stokes equations, would most certainly be impossible without many simplifying assumptions. Added to these difficulties is the fact that no solid surface can be seen on Jupiter which would eliminate badly needed boundary conditions. Thus, the study of the circulation of Jupiter's atmosphere is most complicated and leaves much to be desired.

Since a solid surface cannot be seen, there is no well-established, fixed zenographic coordinate system. There are, however, three general methods used for determining the rotation rate of Jupiter and hence, atmospheric circulation. There are: (1) the optical [visual] method, (2) the spectroscopic [Doppler shift] method, and (3) the radioemission method.

The optical method is used for the cloud surface and consists in the timing of successive transits of well-defined and long-lived markings, such as spots, ends of streaks, etc., which are rotating across the central meridian of the Jovian disk. The rotational period of a cloud feature, resulting from the erratic motions of the cloud band in which it lies, is measured. The results of many years of observations by both amateurs and professionals were compiled by Peek [Ref. A-27].

The spectroscopic method measures the Doppler shift of Fraunhofer lines of the solar spectrum which is reflected by the clouded planet (Jupiter has a high albedo). This method, however, is of low accuracy and is seldom used.

The radio emission method makes use of the decameter radio burst which emanate from Jupiter. By assuming that these radio signals were emitted from fixed locations, a reference coordinate system can be established.

In 1962, the International Astronomical Union adopted as the official system, known in the literature as System III, a period of rotational of $9^{\text{h}}55^{\text{m}}29^{\text{s}}.37$. This system and the quasi-constant radio period of rotation is claimed by many to be linked to the actual solid-liquid body of Jupiter and is the best base reference for atmospheric circulations studies.

Atmospheric motions on Jupiter may derive their kinetic energy from both solar heating and internal sources. Opik [Ref. A-55] and others suggest the internal sources supply between 80 and 160 percent of that associated with solar radiation. These internal sources may be due to gravitational energy release because the ratio of the gravitational energy to the total solar energy intercepted by Jupiter in four billion years is 50. The corresponding ratio for Earth is about 0.03.

Hide [Ref. A-56] suggests four parameters which characterize the dynamics of a rapidly rotating planet. There are:

$$\text{The "Rossby" number} \quad \mu R = \frac{1}{2L\Omega} \quad (11)$$

$$\text{A rotational mach number} \quad M \equiv \frac{L\Omega}{c} \quad (12)$$

$$\text{A parameter} \quad B \equiv \frac{\omega^2}{4\Omega^2} \quad (13)$$

$$\text{A parameter} \quad D \equiv \frac{2d}{a} \quad (14)$$

$$\text{Where:} \quad \omega = \frac{-g\Gamma}{\rho}$$

ω is the so-called Brunt-Vaisala frequency

ν is a typical horizontal wind speed

L is a length characteristic of the horizontal scale of the motion

c is the speed of sound in the atmosphere

g is the acceleration of gravity

Γ is the vertical gradient of potential density

ρ is the actual density

Ω is the basic rotation of the planet

a is the radius of the planet

d is a characteristic length of the vertical structure of the atmosphere.

When Γ is negative (i.e., sub-adiabatic lapse rate), ω is real and B is positive. A fluid particle displaces vertically by a small amount from its equilibrium position and oscillates about that position with angular velocity. When Γ is positive (i.e., super-adiabatic lapse rate), ω is imaginary and B is negative. The hypothetical equilibrium state of such an atmosphere is then unstable to vertical fluid disturbances.

For comparison, Earth's atmosphere has values of $R \sim 0.1$, $M \sim 1$, $D \sim 0.001$, and B is stable. Jupiter's atmosphere has values of $R \sim 0.01$ in the equatorial regions of 10^{-5} at higher latitudes, $M \sim 10$ or higher, and the sign and value of B is unknown. If internal energy sources are comparable with solar heating, B may well be negative, in which case vertical overturning associated with a super-adiabatic lapse rate might constitute the principal mode of hydrodynamical flow.

The low values of R suggest that the effects of quite shallow topographic features of any bounding surface underlying the atmosphere will extend upward throughout the atmosphere. A simple example of this phenomenon is the "Taylor column."* This also has been used by Hide [Ref. A-57] to explain the Great Red Spot. The implications of this suggestion in regard to (a) the physical and chemical nature of the region underlying Jupiter's atmosphere, (b) the angular momentum transfer between different parts of the planet to account for the Red Spot's variations in longitude, and (c) the nature of the "topographical feature" are not settled and are fairly controversial at the present time.

Rapid equatorial currents in the fluid layers are bound to exist on the rapidly rotating Jupiter as they do on Earth.** These currents should be of the order of Rossby number $R^{1/2}$ and if these currents represent "sinks" of kinetic energy and angular momentum originating at higher altitudes, they may only build up to $R \sim D$.

Over the years there have been many attempts at theoretical explanations of general circulation theories. Schoenberg [Ref. A-58], ignoring solar heating, assumed that the sole source of energy which drives the atmospheric circulation was internal heat energy released by volcanic eruptions. Other investigators used a more classical fluid mechanics approach bringing in conservation of angular momentum and vorticity and correlating their theories with observations of Earth's atmosphere. Large-scale eddies (at least on Earth) of preferred shape and orientation act to transport angular momentum against the prevailing fluid gradients thereby permitting jet streams to be maintained despite frictional dissipation. Owen and Staley [Ref. A-59], using System III, have shown that the wind at the equator at the visible surface is westerly at 105 meters per

* A Taylor column in a rotating, homogeneous, incompressible column of fluid which will move two-dimensionally in planes perpendicular to the axis of rotation

**On Earth there is the Cromwell current in the ocean and the Berson westerlies in the atmosphere.

second; at 20° latitude the wind is easterly at 4 m/sec, and poleward of 20° the easterlies diminish. These two investigators also showed that there existed high-level winds relative to System III. These have varied from -6700 m/sec in 1934 to -3900 m/sec in 1961, to +100 m/sec in 1962, while the low level winds remained relatively constant at +100 m/sec where the sign change indicates a reversal in their direction.

Mintz [Ref. A-60] suggested that since Jupiter has little equatorial tilt, it received more solar heat at its equator than at its poles thereby setting up a potential temperature gradient. The energy transport must then occur in the form of large-scale eddies since the winds are mainly parallel to the equator.

Focas and Banos [Ref. A-61] suggested that the bands of Jupiter, even though they give the impression of symmetry, indicate strong thermal convection and their fine structure shows wave like disturbances. Many bright and dark spots, wisps, rifts, and other features which are more prevalent near the equator are influenced by the Great Red Spot and are deflected around it. This again supports the contention that the Great Red Spot is some sort of a barrier.

Shapiro [Ref. A-62] identifies the dark spots with cyclones and the light spots with anticyclones. A cyclone is a descending motion at high altitudes which carries the ammonia clouds deeper into the atmosphere while an anticyclone is an ascending motion at high levels which brings the ammonia clouds into prominence. (It might be noted that terrestrial clouds show the opposite effect, that is, bright cyclones and dark anticyclones. This is because the anticyclones are relatively cloudfree, permitting Earth's surface to be visible.)

There is some evidence of climate zones on Jupiter as there are on Earth. Shapiro [Ref. A-62] suggests that the conventional climate zones of Earth be shifted toward the equator on Jupiter as seen in Table A-8.

TABLE A-8. CLIMATE ZONES

<u>Zone</u>	<u>Zenographic latitude, deg</u>	<u>Terrestrial latitude, deg</u>
Equatorial	0 - 6	0 - 10
Tropic and subtropic	7 - 12	10 - 30
Temperate	13 - 25	30 - 60
Subpolar and polar	26 - 90	60 - 90

The Great Red Spot has captured the imaginations of many investigators and numerous theories have been proposed. Earlier investigators seem to favor an underlying solid surface while later investigators suspect some sort of a floating body. As previously mentioned, Hide [Ref. A-63] proposed that the Great Red Spot is a Taylor column. He showed that this Taylor column could exist if the atmosphere were no deeper than 2800 kilometers and, if its depth were only 1000 kilometers where the topographical feature causing it could be as low as 1 kilometer. The longitudinal drift of the Great Red Spot is then explained by assuming that Jupiter consists of a fluid core with a thin, solid mantle and a deep, massive atmosphere. Momentum exchanges between the atmosphere and mantle could cause a changing rotation rate. On the other hand, Sagan [Ref. A-35] attributed the red color of the Great Red Spot to the active of electrical discharges on the atmospheric gases.

SATELLITES

Jupiter has 12 known satellites which can be divided into two subgroups according to their proximity to the giant planet. The inner system consists of five bodies, four of which are very large and are known as Galilean satellites. The remaining seven satellites constitute the outer system. This system is sometimes divided into two sub-groups which describe the relative motion of the subgroup, i. e. , either the motion is directed forward or backward with respect to the planet. Table A-9 lists some data on the Jovian satellites.

The inner system of five bodies lie within 2×10^6 kilometers of Jupiter and are, with one exception, large in size. All five revolve in nearly circular equatorial orbits with the same direct motion as the planets (counterclockwise when seen from the North Pole of the ecliptic).

The first two satellites, Io (J I) and Europa (J II), are similar to the moon in size. Ganymete (J III) is larger than the planet Mercury while Callisto (J IV) is almost the size of Mercury. Almalthea (J V) is very small and close to the planetary surface making observation difficult because of its rapid rotation.

The motion of J I, J II, and J III are very tightly coordinated. These three satellites have orbital planes which are very near to that of the Jovian equator and make only a small angle with the orbital plane of Jupiter. Therefore they pass, once every revolution, behind Jupiter's globe and enter its shadow cone. Satellites J I, J II, and J III may all be visible at one time from Earth, or two may be eclipsed or occulted and the third passing in front of the

TABLE A-9. SATELLITES OF JUPITER

Number	Name	Distance kmx10 ³	Distance in Jupiter Radii	Period (Days)	Inclination to Orbit Degrees	Radius km	Mass 10 ⁻²⁴ g	Semi- Major Axis of Orbit in Jupiter Radii	Eccentric- ity	Absolute Semi-Major Axis km*	Absolute Density gm/cm ³
I	Io	421.8	5.905	1.769138	3° 8'	1660	79	5.9	0.0	421 560	2.5
II	Europa	671.4	9.396	3.551181	3° 8'	1440	47.8	9.4	0.0003	670 780	3.0
III	Ganymede	1071	14.99	7.154553	3° 8'	2470	153	15.0	0.0015	1 070 140	1.7
IV	Callisto	1884	26.36	16.689018	3° 8'	2340	90	26.4	0.0075	1 881 800	1.3
V	Almalthea	181	2.539	0.498179	3° 8'	80	?	2.5	0.0038	181 260	?
VI	Hestia	11 500	160.7	250.62	28.5°	60	?	161	0.155	11 472 000	?
VII	Hera	11 750	164.4	259.8	28.0°	20	?	165	0.155	11 736 000	?
VIII	Poseidon	23 500	326	738.9	33.0° retrograde	20	?	330	0.25--.4	23 273 000	?
IX	Hades	23 700	332	755.0	24.0° retrograde	11	?	332	0.1--.4	23 701 000	?
X	Demeter	11 750	164	260.0	28.3°	10	?	165	0.08	11 708 000	?
XI	Pan	22 500	343	696.6	16.6°	12	?	315	0.21	22 345 000	?
XII	Andrastae	21 000	290	625.0	?	10	?	-	-	20 703 000	?

* R₁ = 71390
km

planet. J IV has an orbit such that it can pass above or below Jupiter and its shadow. Sampson [Ref. A-64] and DeSitter [Ref. A-65] have developed detailed, complex theories to describe the movement of the inner satellites.

The Galilean satellites are subject to very strong mutual perturbations, causing librations in their orbits.* The optical parameters, such as color and magnitude, are also well known. Spectroscopic data suggests the presence of atmospheres around them although these may be extremely thin. Radiometric temperatures have indicated values of 135° K for J I, 141° K for J II, 155° K for J III, and 168° K for J IV. These show some departure from Planckian distribution of emitted radiation.

The outer direct revolving satellites are approximately 0.08 astronomical units from Jupiter. Their orbital motion is inclined $\sim 28^\circ$ to Jupiter's orbit and periods of revolution of ~ 250 days. The outer retrograde revolving satellites are similarly inclined but have longer periods (620 to 760 days) around Jupiter. The great perturbations from the sun and the closeness of Saturn influence these small, outer satellites. Their motion is unpredictable and the orbits do change, all of which indicates they are captured asteroids.

* Perturbations are the deviations from a reference orbit or gross motion that are occasioned by forces not included in the integration of the reference orbit.

REFERENCES

1. Michaux, C. M.; Fish, F. F., Jr.; Murray, F. W.; Santina, R. W. and Steffey, P. C.: Handbook of the Physical Properties of the Planet Jupiter. NASA SP-3031, 1967, p. 142.
2. Clemence, G. M.: Quoted anonymously in Astronomical Notes from Hamburg - 2, Sky and Telescope, vol. 29, no. 1. January 1965, pp. 19-22.
3. Opik, E. J.: Jupiter: Chemical Composition, Structure, and Origin of a Giant Planet, Icarus, vol. 1, no. 3. October 1962, pp. 200-257.
4. Wildey, R. L.; Murray, B. C. and Westphal, J. A.: Thermal Infrared Emission of the Jovian Disk. J. Geophys. Res., vol. 70, no. 15, August 1, 1965, pp. 3711-3719.
5. The American Ephemeris and Nautical Almanac. Issued in annual volumes by year. Nautical Almanac Office, U. S. Naval Observatory (Washington, D. C.) Government Printing Office.
6. Brouwer, D. and Clemence, G. M.: Orbits and Masses of Planets and Satellites, ch. 3, vol. 2, The Solar System. G. P. Kuiper and B. M. Middlehurst, eds., The University of Chicago Press, 1961, pp. 31-44.
7. Shain, C. A.: Location on Jupiter of a Source of Radio Noise, Nature, vol. 176, no. 4487, October 29, 1955, pp. 836-837.
8. Zhelenzniakov, V. V.: On the Theory of the Sporadic Radio Emission from Jupiter. Astron. Zh., vol. 35, no. 2, March-April 1958, pp. 230-240.
9. Gallet, R. M.: Radio Observations of Jupiter II, Planets and Satellites, ch. 14, vol. 3 of the Solar System. G. P. Kuiper and B. M. Middlehurst, eds., University of Chicago Press, 1961, pp. 500-533.
10. Strom, S. E. and Strom, K. M.: A Possible Explanation for Jovian Decameter Bursts. Astrophys. J., vol. 136, no. 1, July 1962, pp. 307-310.

REFERENCES (Continued)

11. Sagan, C. and Miller, S. L.: (Abstract) Molecular Synthesis in Simulated Reducing Planetary Atmospheres. *Astron J.*, vol. 65, no. 9, November 1960, p. 499.
12. Warwick, J. W.: Dynamic Spectra of Jupiter's Decametric Emission, 1961. *Astrophys. J.*, vol. 137, no. 1, January 1963, pp. 41-60.
13. Hirschfield, J. L. and Bekefi, G.: Decameter Radiation from Jupiter. *Nature*, vol. 198, no. 4875, April 6, 1963, pp. 20-22.
14. Ellis, G. R. A. and McCullough, P. M.: Decametric Radio Emission of Jupiter. *Nature*, vol. 198, no. 4877, April 20, 1963, p. 275.
15. Chang, D. B.: Amplified Whistlers as the Source of Jupiter's Sporadic Decameter Radiation. *Astrophys. J.*, vol. 138, no. 4, November 1963, pp. 1231-1241.
16. Six, N. F., Jr.: Characteristics and Origin of the Nonthermal Radio Emission from Jupiter, Scientific Research Laboratories. Brown Engineering Company, Incorporated, Hunstville, Alabama, Technical Note R-60, July 1963, p. 62.
17. Slonaker, R. M.: (Abstract) Apparent Temperature of Jupiter at a Wavelength of 10 cm. *Astron. J.*, vol. 64, no. 8, October 1959, p. 346.
18. Chang, D. B. and Davis, L., Jr.: Synchrotron Radiation as the Source of Jupiter's Polarized Decimeter Radiation. *Astrophys. J.*, vol. 136, no. 2, September 1962, pp. 567-581.
19. Field, G. B.: The Source of Radiation from Jupiter at Decimeter Wavelengths. 3 Time Dependence of Cyclotron Radiation. *J. Geophys. Res.*, vol. 66, no. 5, May 1961, pp. 1395-1405.
20. Warwick, J. W.: Dynamic Spectra of Jupiter's Decametric Emission, 1961. *Astrophys. J.*, vol. 137, no. 1, January 1963, pp. 41-60.

REFERENCES (Continued)

21. Berge, G. L. and Morris, D.: Decimeter Measurements Relating to the Possible Displacement of Jupiter's Magnetic Dipole. *Astrophys. J.*, vol. 140, no. 3, October 1964, pp. 1330-1332.
22. Axford, W. I.; Dessler, A. J. and Gatllieb, B.: Termination of Solar Wind and Solar Magnetic Field. *Astrophys. J.*, vol. 137, no. 4, May 1963, pp. 1268-1278.
23. Mead, G. D. and Beard, D. B.: Shape of the Geomagnetic Field Solar Wind Boundary. *J. Geophys. Res.*, vol. 69, no. 7, April 1964, pp. 1189-1190.
24. Radhakrishnan, V. and Roberts, J. A.: Polarization and Angular Extent of the 960-Mc/sec Radiation from Jupiter. *Phys. Rev. Letters*, vol. 4, no. 10, May 15, 1960, pp. 493-494.
25. Hide, R.: Planet. *Space Science* 14, 1966, p. 579.
26. Hove, L. E. and others: Final Technical Report of a Study of Jupiter Flyby Missions. FZM-4625, General Dynamics, May 17, 1966.
27. Peek, B. J.: *The Planet Jupiter*. Faber and Faber (London), 1958, p. 283.
28. Rice, F. O.: *The Chemistry of Jupiter*, vol. 194, no. 6, 1956, pp. 119-128.
29. Rice, F. O.: Colors on Jupiter. *J. Chem. Phys.*, vol. 24, no. 6, June 1956, p. 1259.
30. Rice, F. O. and Cosgrave, D. P.: Some Experiments on Rice's Blue Material: Colors on Jupiter. *Nature*, vol. 188, 1960, p. 1023.
31. Papazian, H. A.: The Colors of Jupiter. *Publ. Astron. Soc. Pacific*, vol. 71, no. 420, June 1959, pp. 237-239.
32. Wildt, R.: On the Chemical Nature of the Colouration in Jupiter's Cloud Forms. *Monthly Notices Roy. Astron. Soc.*, vol. 99, no. 8, June 1939, pp. 616-623.

REFERENCES (Continued)

33. Abelson, P. H.: Pabeobiochemistry, Inorganic Synthesis of Amino Acids. Carnegie Institute of Washington Year Book, vol. 55, 1956, p. 171.
34. Heyns, K.; Walter, W. and Meyer, E.: Modelluntersuchungen zur Bildung Organischer Verbindungen in Atmosphären einfacher Gase durch Elektrische. *Nature.*, vol. 44, 1957, pp. 385-389.
35. Sagan, C.: Exobiology: A. Critical Review in Life Sciences and Space Research II. M. Florkin and A. Dollfus, eds. North-Holland Publ. Co. (Amsterdam) 1964, pp. 35-53.
36. Siegel, S. M and Giurmarro, C.: Survival and Growth of Terrestrial Micro-organisms in Ammonia-rich Atmospheres. *Icarus*, vol. 4, 1965, pp. 37-40.
37. Hess, S. L.: Variations in Atmospheric Absorption Over the Disks of Jupiter and Saturn. *Astrophys. J.*, vol. 118, no. 1, July 1953, pp. 151-160.
38. Squires, P.: The Equatorial Clouds of Jupiter. *Astrophys. J.*, vol. 126, no. 1, July 1957, pp. 185-194.
39. Sharonov, V. V.: Physical Interpretation of Jupiter. *Doklady Akad. Nauk SSSR*, vol. 39, no. 5, 1943, pp. 173-175.
40. Kuiper, G. P.: Planetary Atmospheres and their Origin, The Atmospheres of the Earth and Planets, ch. 12. G. P. Kuiper, ed., University of Chicago Press, 1952, 434 pp., pp. 306-405.
41. Herzberg, G.: On the Possibility of Detecting Molecular Hydrogen and Nitrogen in Planetary and Stellar Atmospheres by their Rotation-Vibration Spectra. *Astrophys. J.*, vol. 87, no. 4, May 1938, pp. 428-437.
42. Kiess, C. C.; Corliss, C. H. and Kiess, H. K.: High-Dispersion Spectra of Jupiter. *Astrophys. J.*, vol. 132, no. 1, July 1960, pp. 221-231.

REFERENCES (Continued)

43. Field, G. B.: Hydrogen Molecules and Astronomy: A Review. W. B. Somerville, et al., eds. Princeton University Observatory, 1962, p. 32.
44. Wildt, R.: Absorptionsspektren and Astmosphären der grossen Planeten, Nachr. Ges. Akad. Wiss. Gottinger, vol. 1, 1932, pp. 87-96.
45. Wildt, R.: Photochemistry of Planetary Atmospheres. Astrophys. J., vol. 86, no. 3, October 1937, pp. 321-336.
46. Spinrad, H. and Trafton, L.: High Dispersion Spectra of the Outer Planets. I. Jupiter in the Visual and Red. Icarus, vol. 2, no. 1, June 1963, pp. 19-28.
47. Baum, W. A. and Code, A. D.: Photometric Observations of the Occultation of ϵ Arietis by Jupiter. Astron., J., vol. 58, no. 4, May 1953, pp. 108-112.
48. Gross, S. H. and Rasool, S. I.: The Upper Atmosphere of Jupiter. Icarus, vol. 3, no. 4, November 1964, pp. 311-322.
49. Urey, H. C.: The Atmospheres of the Planets, In Astrophysics III: The Solar System, vol. 52 of Handbuch der Physik (Encyclopedia of Physics), S. Flugge, ed., Springer-Verlag (Berlin), 1959, pp. 363-418.
50. Smith, R. E. and Vaughan, O. H., Jr.: Space Environment Criteria Guidelines for Use in Space Vehicle Development 1967 Revision. NASA TMX-53521. February 1961.
51. Gallet, R.: (quoted by Peebles, 1964) a paper presented at NASA Institute for Space Studies, New York, October 1962. To be published in Proc. Conf. Planet Jupiter, H. J. Smith, ed.
52. Peebles, P. J. E.: The Big Planets. Intern. J. Sci. Tech., no. 35, November 1964, pp. 32-38 and p. 79.

REFERENCES (Continued)

53. Peebles, P. J. E.: The Structure and Composition of Jupiter and Saturn. *Astrophys. J.*, vol. 140, no. 1, July 1964, pp. 328-347.
54. DeMarcus, W. C.: Theoretical Pressure-Density Relations with Applications to the Constitution of the Planets. PhD Thesis, Yale University, 1951.
55. Opik, E. J.: *Icarus* I, 1962.
56. Hide, R.: On the Circulation of the Atmospheres of Jupiter and Saturn. *Planet Space Sci.* 1966, vol. 14, pp. 669-675.
57. Hide, R.: *Nature*. London 190, 1961, p. 895.
58. Schoenberg, E.: Zur Dynamik der Jupiteratmosphäre, *Astron. Nachr.*, vol. 273, 1943, pp. 113-123.
59. Owen, T. C. and Staley, D. O.: A Possible Jovian Analogy to the Terrestrial Equatorial Stratospheric Wind Reversal. *J. Atm. Sci.*, vol. 20, no. 4, 1963, pp. 347-350.
60. Mintz, Y.: The General Circulation of Planetary Atmospheres. Appendix 8 to *The Atmospheres of Mars and Venus*, Publication 944, National Academy of Sciences - National Research Council, 1961, pp. 114-146.
61. Focas, J. H. and Banos, C. J.: Photometric Study of the Atmospheric Activity on the Planet Jupiter and Peculiar Activity in its Equatorial Area. *An. Astrophs.*, vol. 27, no. 1, January-February 1964, pp. 36-45.
62. Shapiro, R.: A Quantitative Study of Bright and Dark Spots on Jupiter's Surface. *The Study of Planetary Atmospheres*. Final Report, Lowell Obs., 1952 a and b, pp. 97-126.
63. Hide, R.: On the Hydrodynamics of Jupiter's Atmosphere. (Physics of Planets) *Mem. Roc. Roy. Sci. Liege, Series V*, vol. 7, 1963, pp. 481-505.

REFERENCES (Concluded)

64. Sampson, R. A.: Theory of the Four Great Satellites of Jupiter. Mem. Roy. Astron. Soc., vol. 63, 1921, p. 270.
65. DeSitter, W.: Jupiter's Galilean Satellites. Monthly Notices Roy. Astron. Soc., vol. 91, no. 7, May 1931, pp. 706-738.

BIBLIOGRAPHY

Glasstone, S.: The Sourcebook on the Space Sciences. Van Nostrand Co., 1965.

APPENDIX B

INTERPLANETARY SPACE ENVIRONMENT



APPENDIX B

INTERPLANETARY SPACE ENVIRONMENT

DEFINITION OF SYMBOLS

A	Spacecraft exposed area (m^2)
a	Semi-major axis (km)
C_t	Sonic velocity (km/sec)
c	Speed of light (km/sec)
E	Proton energy (joules)
e	Eccentricity (dimensionless)
e	Proton charge (coulombs)
$F_{>}$	Mass cumulative mean influx of cometary meteoroids
f	Frequency (cycles/sec)
k	Factor dependent of solar flare energy spectrum
k_t	Material parameter
I	Number of meteoroid impacts
i	Inclination, angle between the planets of the orbit and plane of the equator (rad)
$M_0 C^2$	Proton rest energy (joules)
N	Number of protons (protons/cm ²)
$N_{max.}$	Maximum number of particles (cm ² -sec)
P	Radiation pressure (dynes/m ²)

DEFINITION OF SYMBOLS (CONTINUED)

P	Moment of unit charge (volts)
P*	Period (year)
P ₀	Constant (volts)
P _t	Specific gravity
p	Material thickness
R	Astronomical units from sun
r	Geocentric radius (cm)
S	Solar constant
T	Spacecraft flight time (sec)
t	Delay time (sec)
t _{max.}	delay time to N _{max.} (sec)
w	Argument of perigee (radians)
Z	Atomic number
α	Meteoroid flux intensity (number of particles)
β	Meteoroid flux gradient
λ	Geomagnetic latitude (radians)
φ	Meteoroid flux $\left(\frac{\text{number of particles}}{\text{m}^2 - \text{sec}} \right)$
$\bar{\phi}$	Mean number of meteoroid punctures
ρ	density (gm/cm ³)
Ω	Longitude of node (degrees)

GENERAL FEATURES

A spacecraft on a mission to Jupiter must pass through several hostile environments. Some of these may adversely affect the mission causing a decrease in the probability of success. The major environments of interplanetary space* include meteoroids, asteroids, comets, galactic cosmic radiation, space magnetic fields, solar winds, solar flares, and solar thermal radiation.

A major restriction to any Jupiter mission is the time required to perform the mission. A longer mission means a greater exposure of the spacecraft to the hazards of space. The factor of time is, of course, a matter for overall mission planning for it is coupled in the many "trade-off" factors that must be made.

Space hazards can be separated into two general categories. Those of macroscopic particles and bodies and those of microscopic particles. The environments of meteoroids, asteroids, and comets are in the first group while magnetic fields, cosmic, and solar radiation are in the second group.

The meteoroid environment is not constant throughout a Jupiter mission. Meteoroid quantity and energy spectra varies with the region in space and they usually occur in streams. There is a greater frequency of encounter in the Asteroid Belt than in the near-Earth, near-Jupiter, or elsewhere in interplanetary space.

The Asteroid Belt is the remains of the "missing" planet. It is thought to be a direct result of Jupiter's tremendous mass and the asteroids are the farthest from the sun of the terrestrial bodies. The probability of direct encounter with one of these 6000 or more bodies is remote; however, the meteoroid debris which is carried along in the belt is the primary hazard.

As with the asteroids, the comet hazard to the spacecraft is minimum. For both environments, however, the principal value to a mission is the opportunity to observe and investigate them as supplemental information.

* Interplanetary space is defined as the region from the sun to the outer limits of the solar system exclusive of those regions that are under the influence of individual planetary systems.

Within the solar system, nature has provided several different accelerated particles. These particles are from many sources and represent a wide range of energies. Within the solar system, the acceleration of particles covers a range of over 10 decades of energy. Perhaps the most dramatic of these particles are the cosmic rays. Solar flares represent the only direct observation of the birth of the cosmic-ray particles. Solar flares also release lower-energy particles in great abundance.

Figure B-1 gives an indication of the energy spectra of particles from different sources as they are known at the present time. Spectrum I of the cosmic radiation, mostly from the galaxy, has been derived from a series of measurements extending over 15 years. Spectrum II is protons from the large solar flare which occurred in 1956 and particles derived from acceleration within the solar system. Spectrum III is also from a solar flare which produced much lower energy protons. Spectrum IV represents the recent measurement of the Van Allen trapped radiation close to Earth. Spectrum V is the trapped electrons in Earth's magnetic field. The dash lines indicate unknown extension of the spectrum.

The principal danger resulting from the microscopic environments is damage to the electronic components and instrumentation. Also some damage might occur to the propellants and other subsystems.

The purpose of this Appendix is to give the reader a brief overview of the major environments that a Jupiter mission will encounter from launch to near-Jupiter.

METEOROID ENVIRONMENT

General Discussion

Meteoroids are permanent members of our solar system. Their orbits are similar to those of the planets, being essentially parallel to or slightly inclined to the ecliptic plane. Information regarding meteoroids has been obtained from visual, telescopic, photographic, and radar observations. These data are used to estimate meteoroid sizes, velocities, and frequencies.

Meteoroids appear to originate in the region of the minor planets and are associated with comets. It is postulated that there should have been a planet

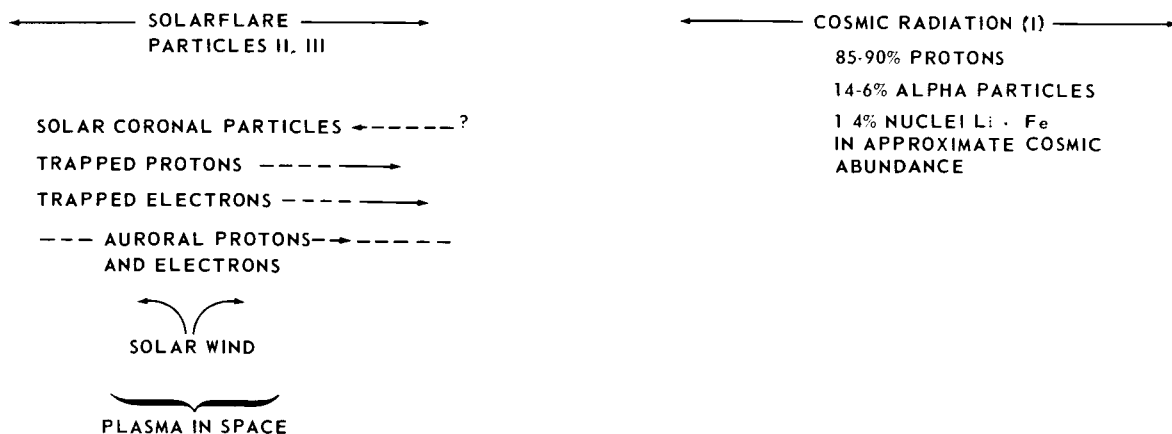
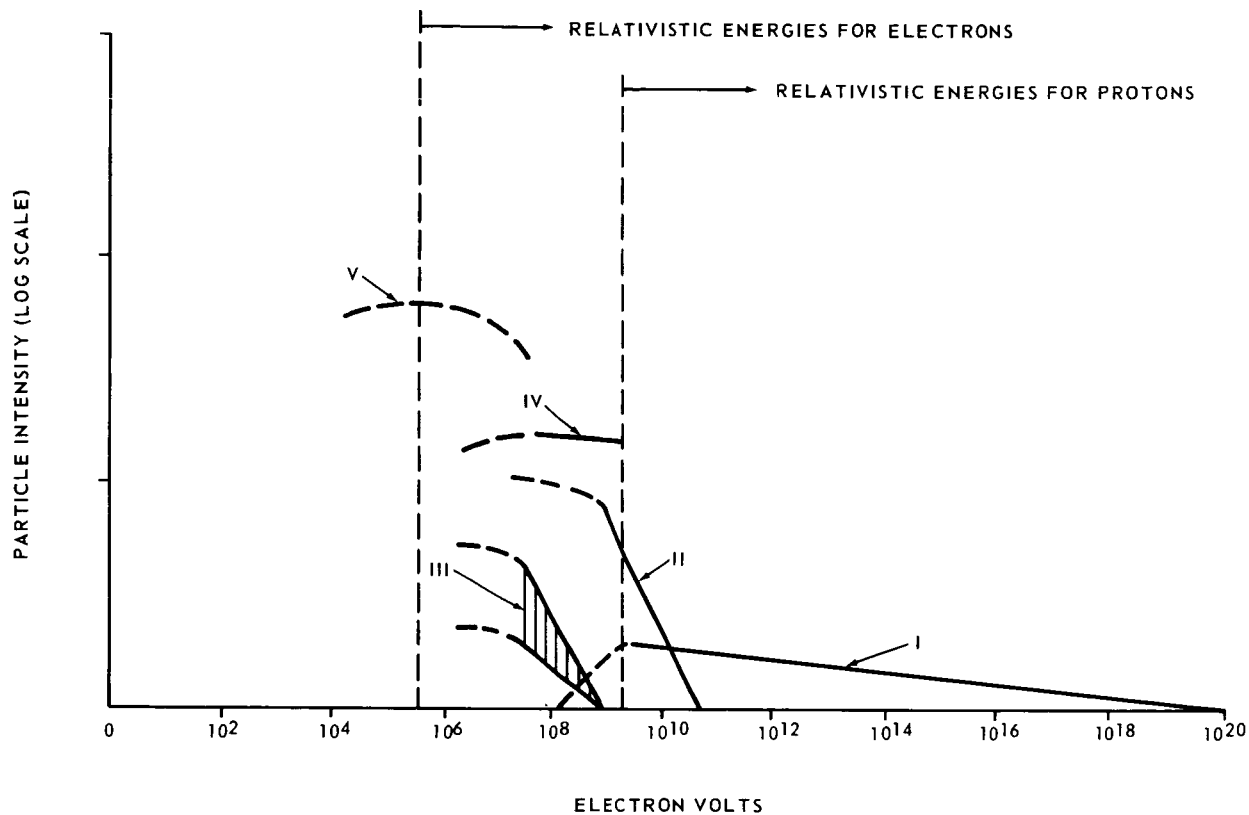


FIGURE B-1. SPECTRA OF ENERGETIC PARTICLES OBSERVED IN THE SOLAR SYSTEM

form in the asteroid belt but for some unknown reason it failed to coalesce; hence, the region is filled with minor planets and meteoritic matter. Few, if any, meteoroids originate from without the solar system.

Theoretically, particle velocities relative to Earth range from about 11 280 m/sec to about 71 940 m/sec. The size may vary from several centimeters down to micrometers. The frequency of encounter varies greatly with location in space and the duration of spacecraft exposure to the environment. About 99 percent of the particles are believed to be porous and have a rather low density (approximately 0.05 gm/cm³). The remaining 1 percent are believed to be much denser with the stony variety having a density of about 3.2 gm/cm³ and the iron variety having a density of about 7.7 gm/cm³.

Volkoff [Ref. B-1] defines a meteoroid flux for a given portion of space as

$$\phi = \alpha m - \beta = \frac{\text{number of particles of mass } m \text{ or greater}}{m^2 - \text{sec}} \quad (1)$$

where the flux intensity, α , and the flux gradient, β , are constants to determine the number of expected impacts, I , on the spacecraft of particles having mass m or greater; the following equation is used,

$$I = \phi AT \quad (2)$$

where A is the spacecraft exposed area and T is spacecraft flight time in the particular region.

In addition to the parameters α and β , two other parameters are of interest. These are the density, ρ , and the average relative velocity, V .

It is convenient to consider four different meteoroid environments for a Jupiter mission. These are the near-Earth, interplanetary, asteroid, and near-Jupiter which are different regions of the spacecraft trajectory.

The near-Earth meteoroid flux intensity and gradient have been examined by several investigators, such as Alexander, et al. [Ref. B-2], Volkoff [Ref. B-1], and Whipple [Ref. B-3]. Meteoroid influx to Earth are sporadic in nature with meteor streams recurring annually with flux densities up to ten times the average. The particle flow in the near-Earth region is assumed to be isotropic.

The interplanetary region extends from near-Earth to near-Jupiter and consists of both cometary and asteroidal debris. The cometary debris

exists throughout the entire region from Earth to Jupiter (1.0 to 5.2 AU) while the asteroidal debris primarily is located in the region 2.15 to 3.65 AU.

The cometary debris in interplanetary space is thought by McCoy [Ref. B-4] and Parkinson [Ref. B-5] to differ from the terrestrial mean influx of meteor-making and Pegasus-puncturing particles. Dalton [Ref. B-6] set the terrestrial mean influx to be

$10^{-14.49} \text{ m}^{-1.34}$ per square meter per second for particles more massive than m grams. This places the corresponding value elsewhere in Earth's orbit to be 75 percent of this value or

$$10^{-14.61} \text{ m}^{-1.34}$$

McCoy preferred Beard's estimate that the flux of these particles in interplanetary space should vary inversely with the $3/2$ power of the heliocentric distance, i. e., 1.05 order of magnitude lower at Jupiter's orbit. On the other hand Parkinson preferred a more complicated formula giving a 1.92 order of magnitude decrement at Jupiter's orbit. Parkinson indicates that the Jovian and terrestrial gravitationally enhances flux factors in the ratio $170/2.1 = 81$. Using Dalton's value for Earth, the corresponding Jupiter value should be $81/0.75 = 108$, that is, the Jovian influx of cometary particles is about the same as for Earth. Table B-1 summarizes these values for the entire mission.

The asteroidal meteoroid flux of vehicle-puncturing particles was taken by Parkinson to be $10^{-15.91} \text{ m}^{-1}$ per square meter per second at Earth heliocentric distance, and terrestrial enhancement factor is 2.1 while the Jovian influx enhancement factor is 170. Actually these factors depend on a velocity distribution which is different from that for the usual meteor-making particles. Parkinson suggested the following flux enhancement factors with respect to heliocentric distance: Earth, 1.0; asteroids at 2.5 AU, 3×10^4 ; and Jupiter, 20. Table B-1 tabulates these values as well as the total flux caused by both cometary and asteroidal meteoroids.

The asteroidal environment is the region from about 2.15 to 3.65 AU. Objects in this belt that have an absolute photographic magnitude greater than 18 can be observed from Earth. Data on the Asteroid Belt are extrapolated on various theoretical grounds [Ref. B-3].

Most investigators suggest that the Asteroid Belt has the shape of a torus with a major radius of approximately 2.90 AU and a minor radius of approximately 0.75 AU. There exists some uncertainty as to whether the asteroidal particles travel in circular or elliptical orbits. In any event this region is a major source of meteoroids.

TABLE B-1. METEOROID ENVIRONMENT PARAMETERS

<u>Region</u>	<u>Distance</u>	<u>Flux Intensity</u> \propto	<u>Flux Gradient</u> ρ	<u>Particle Density</u> $\rho(\text{gm/cm}^3)$	<u>Particle Velocity Relative to Spacecraft</u> (km/sec)
Near-Earth	1.0 to 65 Earth radii or 6436 to 414 115 km	10^{-17}	1.7	0.433	22
Interplanetary	1.0 AU to 5.2 AU	$10^{-13.3}$	1.0	0.433	12.1
Asteroidal I	2.15 AU	10^{-15}	0.667	3.0	14.9
Asteroidal II	3.65 AU	10^{-9}	1.0	3.0	14.9
Near-Jupiter	1.0 to 400 Jupiter radii or 69 890 to 27 956 800 km	10^{-14}	1.7	0.433	41

Two values of flux intensity and gradients are noted, one being extreme and the other nominal. Also there is general agreement that particle densities range from 1.0 to 7.0 gm/cm³ with 3.0 to 3.5 gm/cm³ being the average. Spacecraft exposure time in this region is estimated at 2.

Little is known about the near-Jupiter meteoroid environment. It is assumed [Ref. B-7] that the particle flux intensity in this region is approximately 3 orders of magnitude more dense near-Jupiter than near-Earth. This increase is attributed to the increased gravitation field of Jupiter. The flux intensity, α , is assumed to be 10^{-14} while the flux gradient, β , is assumed to be the same as that of near-Earth, 1.70. The debris is considered to be about half cometary with a density of 0.433 gm/cm³. This value may be too low because Jupiter's meteoric debris is believed to extend to the planet's tidal radius which is approximately equal to 400 Jupiter radii.

Particle impact velocity is assumed to be larger than Jupiter's escape velocity (one heliocentric velocity) which is 61 km/sec at the surface. Also, particle flow direction in the near-Jupiter region is assumed to be isotropic.

Table B-1 summarizes the four basic meteoroid environment parameters as well as four regions considered. Another summary of flux intensity particles whose mass is equal to or greater than one microgram is shown in Table B-2. Figure B-2 summarizes the meteoroid environment listed in Table B-1.

TABLE B-2. PARTICLES PER SQUARE METER PER SECOND PER 2π STERADIAN UNSHIELDED FROM MASS \geq ONE MICROGRAM

<u>Location</u>	<u>Cometary</u>	<u>Asteroidal</u>	<u>Total</u>
Earth's Orbit	2.69×10^{-7}	1.17×10^{-10}	2.69×10^{-7}
Earth's Influx	3.55×10^{-7}	2.46×10^{-10}	3.55×10^{-7}
Asteroids 2.5 AU	6.76×10^{-8}	3.55×10^{-6}	3.62×10^{-6}
Jupiter's Orbit	3.24×10^{-9}	2.34×10^{-9}	5.58×10^{-9}
Jupiter's Influx	3.55×10^{-7}	4.00×10^{-7}	7.55×10^{-7}

For a mission time of 800 days, it is roughly estimated that a 1976 launch sphere of influence (exposed time) in the near-Earth region is 1 day, the interplanetary region is 710 days, the asteroidal region is 215 days, the near-Jupiter is 86 days.

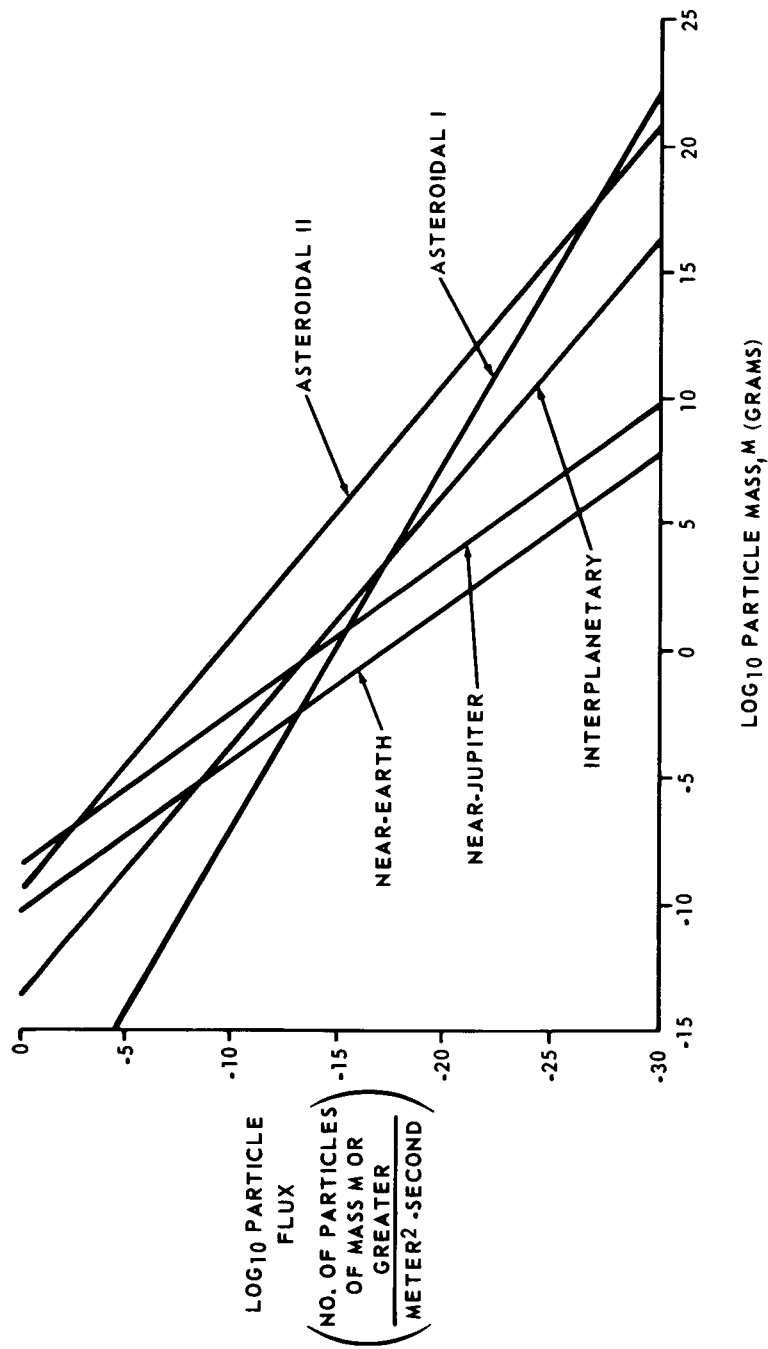


FIGURE B-2. PARAMETRIC ANALYSIS OF METEOROID PARTICLE ENVIRONMENT

A final comment on the puncture bayard. Dalton [Ref. B-6] suggests that sheets of materials from 0.00254 to 0.0416 centimeter thickness are punctured by cometary meteoroids of from 0.23 to 7.4 micrograms. Asteroidal particles of higher density should puncture somewhat more readily. The puncture flux is from 3 to 5 times the flux of nominally puncturing meteoroids because of the statistical variation of the just-puncturable mass.

Several types of meteoroid protection can be employed. The most notable ones are the armor-type and the "bumper" shield. Aluminum is usually considered for the armor-type protection; however, other materials, such as titanium, have merit. Titanium gives a slightly lighter structure for the same penetration protection, but the fabrication processes are considerably more complicated.

Bumper shields consist of two metal sheets separated by a specific space which may or may not contain a filler material. An 80 percent weight savings over the armor-type can be realized by the proper selection of sheet thickness, separation distances, and filler material.

Summary for Design Purposes

The following are Dalton [Ref. B-7] suggested cometary and asteroidal meteoroid flux and puncture models. The nominal cometary meteoroid flux model is given by

$$\begin{aligned} \log F_{>} = & -14.20 - 1.386 (\log m) \\ & -0.331 (\log m)^2 + 0.00051 (\log m)^3 \\ & - \frac{3}{2} \log R \end{aligned} \quad (3)$$

where $F_{>}$ is the mass cumulative mean influx per unshielded square meter per second of cometary meteoroids with mass greater than m in grams. This model is considered accurate to within factor 2 probable error, normally distributed. To obtain 99.86 percent one-sided confidence (3σ level) value, $F_{>}$ should be multiplied by 9. R is the heliocentric distance in astronomical units. It might be noted that the photographic meteoroid density = 0.34 gm/cm^3 .

Dalton gives the cometary meteoroid puncture flux model to be

$$\begin{aligned} \log \bar{\phi} = & - 13.03 - 3.81 (k_t + \log p) - \\ & - 0.384 (k_t + \log p)^2 - 0.017 (k_t + \log p)^3 - \\ & - \frac{93}{38} \log R \end{aligned} \quad (4)$$

where $\bar{\phi}$ is the mean number of punctures per unshielded square meter per second and the material parameter, k_t , is

$$k_t = - 1.360 + \log \left(E_t^{1/18} P_t^{5/6} C_t^{2/3} \right) \quad (5)$$

with E_t the ductility (relative elongation), P_t the specific gravity, C_t the sonic velocity in km/sec and p the material thickness in cm.

For the asteroidal meteoroid flux model, Dalton uses

$$\log F_{>} = - 15.93 - \log m + 13.15 \log R \quad (6)$$

for $1 \leq R \leq 2$ AU

where $F_{>}$ is the number of impacts per unshielded square meter per second of particles with mass in grams exceeding M , the mass of an asteroidal particle and R is the heliocentric distance in astronomical units. The meteoroid density is taken to be 3.4 gm/cm^3 .

Similarly the asteroidal meteoroid puncture flux model is taken to

$$\log \phi = - (54/19) k_t + \log p) - 15.17 + 12.20 \log R \quad (7)$$

for $1 \leq R \leq 2$ AU

where ϕ is the mean number of puncture per unshielded square meter per second, and the material parameter k_t is given by equation (5).

There is a lack of definite data on erosion rates but for interplanetary space between 0.5 to 1.75 AU Reference B-8 suggests the following for aluminum or magnesium:

Depth rate of meteoroid erosion

$$1.5 \times 10^{-13} \text{ cm/sec}$$

Corpuscular sputtering:

$$2 \times 10^{-13} \text{ gm/cm}^2 - \text{sec}$$

Material sublimation:

$$10^{-13} \text{ gm/cm}^2 - \text{sec}$$

For design purposes, Figures B-3 through B-7 summarize the meteoroid penetration of aluminum sheet of various thickness for the average particle flux of the five space regions.

ASTEROID ENVIRONMENT

About 300 years ago it was noted by J. D. Titus that there existed a mathematical regularity in the distance of the planets from the sun. There was, however, one exception to the rule known as Bode's law. A planet was predicted at 28 AU from the sun, midway between Mars and Jupiter [Ref. B-7].

Kuiper, during the development of his protoplanet theory, suggested that this planet could not coalesce from the primeval substance because of the disrupting influence of Jupiter. Several small protoplanets formed in this region and later these collided which greatly increased the number of bodies. It was additionally proposed that further collisions followed resulting in the asteroid belt which is observed today. These "wandering rocks" may provide an important line to the origin of the solar system.

About 6000 asteroids* have been observed and about 1600 of whose orbits have been determined. There may be many more - perhaps tens or hundreds of thousands. The asteroids have been divided into five major families and several minor groups. There appear to be gaps in the belt and these gaps, along with the families, offer a strong argument in favor of the protoplanet hypothesis.

* Asteroids are sometimes called planetoids and minor planets.

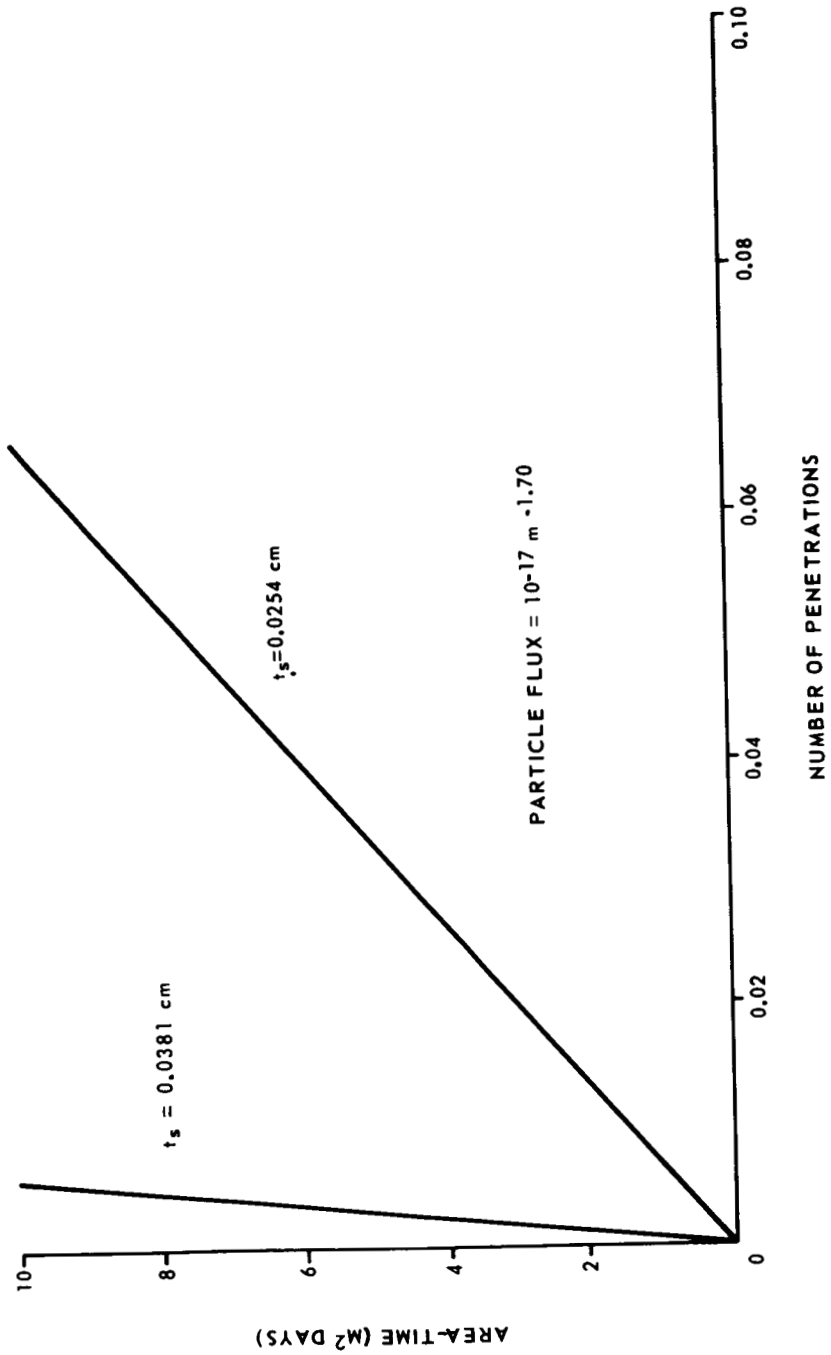


FIGURE B-3. METEROID PENETRATIONS OF ALUMINUM SHEET FOR NEAR-EARTH REGION

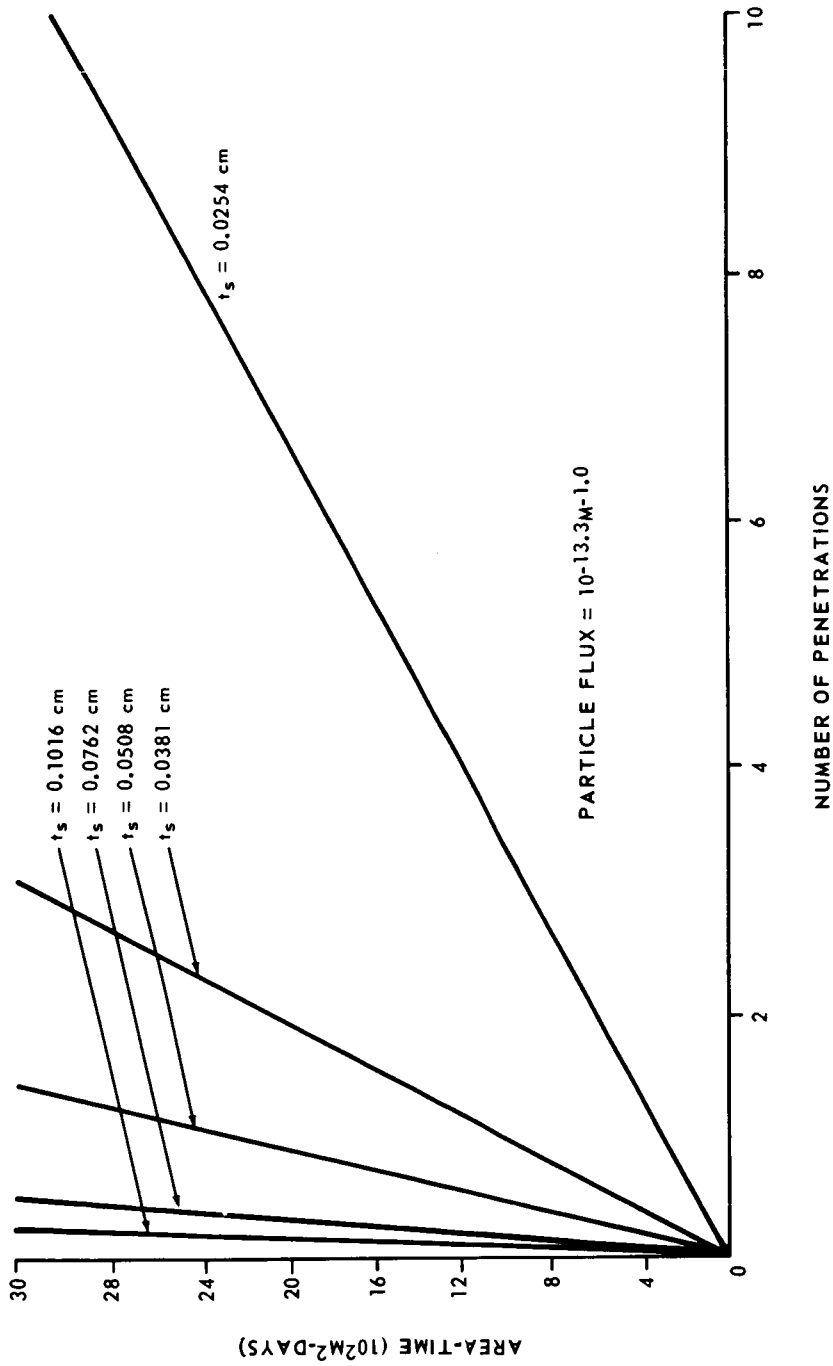


FIGURE B-4. METEOROID PENETRATIONS OF ALUMINUM SHEET FOR INTERPLANETARY REGION

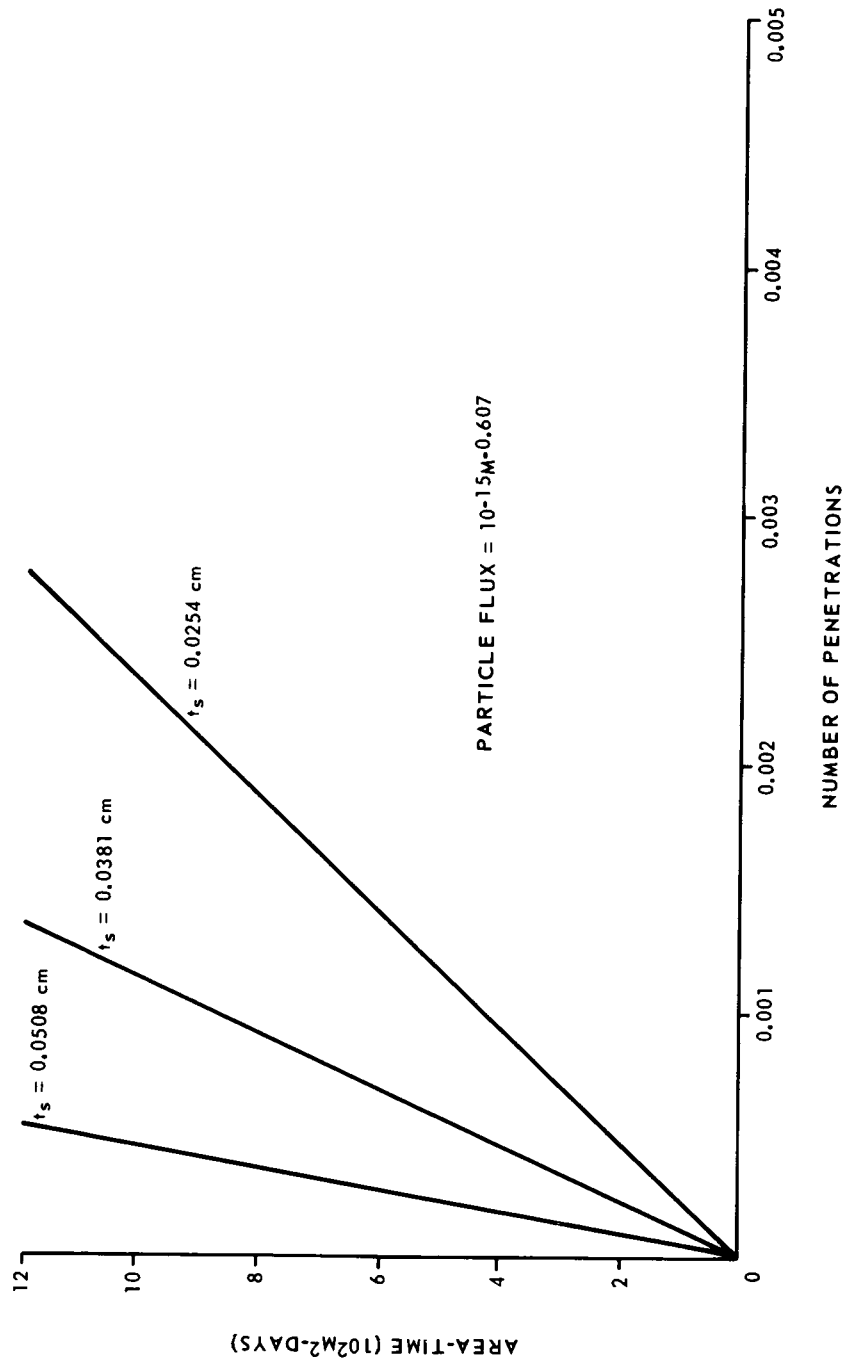


FIGURE B-5. METEOROID PENETRATIONS OF ALUMINUM SHEET FOR ASTEROIDAL REGION I

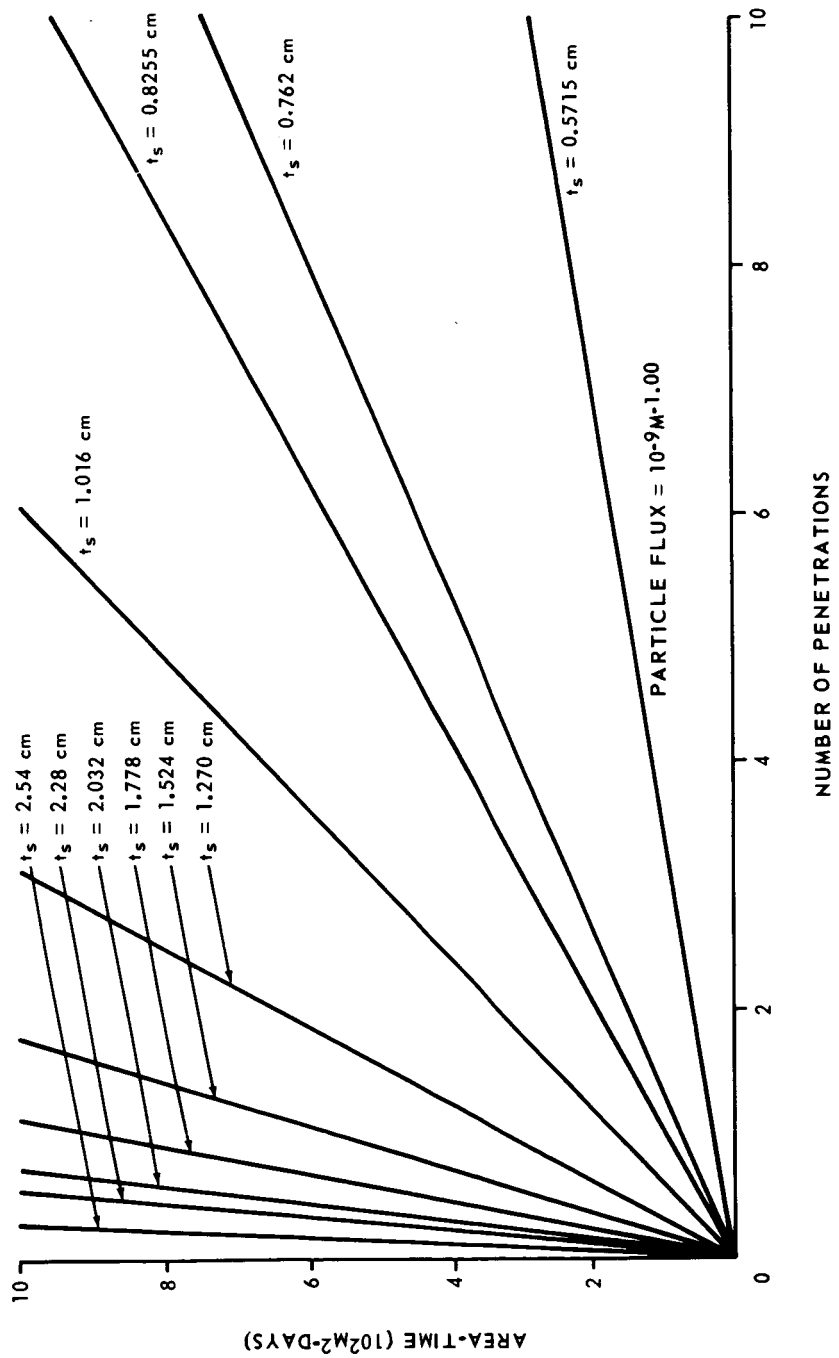


FIGURE B-6. METEOROID PENETRATIONS OF ALUMINUM SHEET FOR ASTEROIDAL REGION II

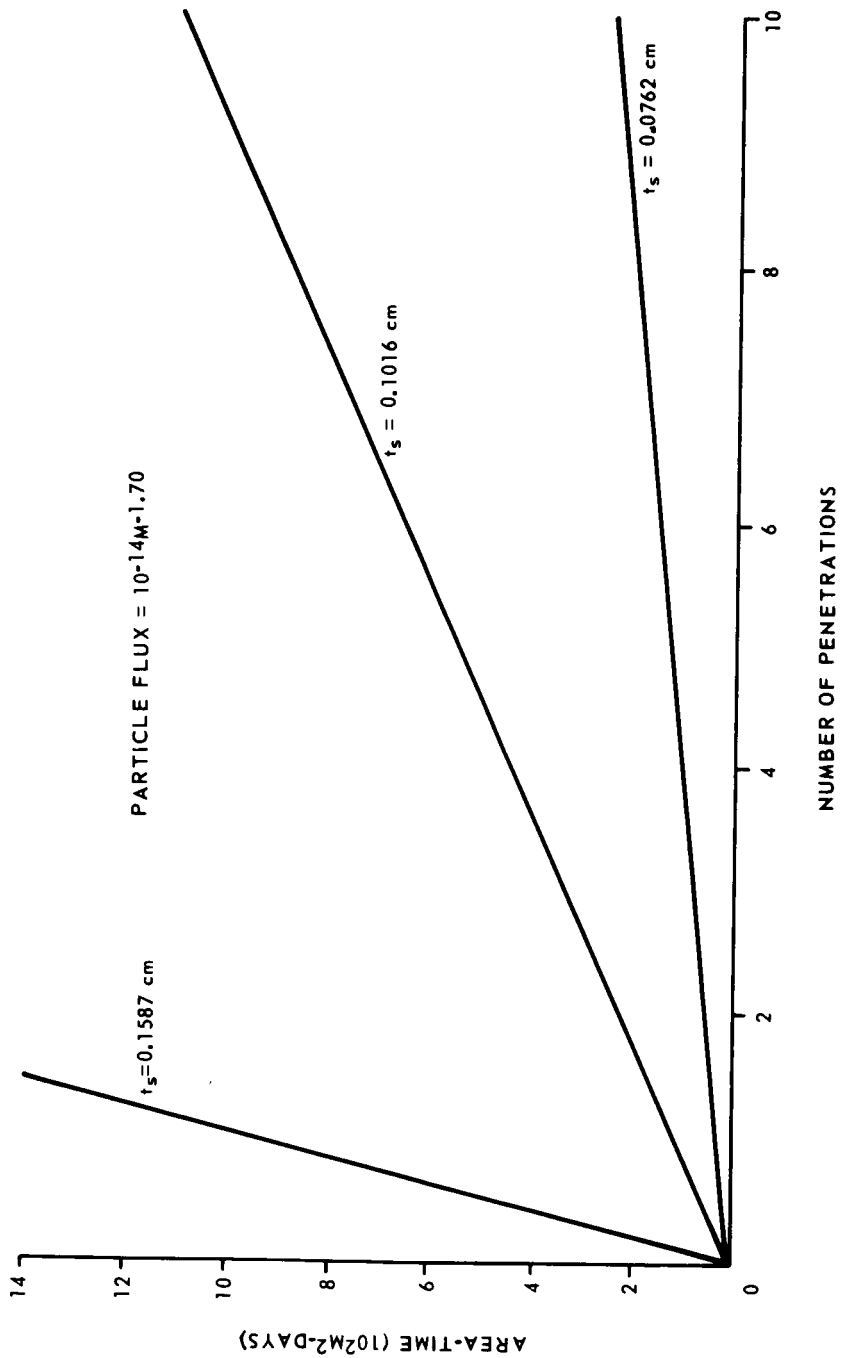


FIGURE B-7. METEOROID PENETRATION FOR ALUMINUM SHEET
NEAR-JUPITER REGION

Several studies have been undertaken to determine the number and frequency distribution of the asteroids. General conclusions of this work are: (1) There is presently insufficient data to be able to ascertain whether the obvious differences between the observed frequency distributions can be attributed to the mass loss of proto-Jupiter or whether another cosmogonic phenomenon is in evidence. (2) There is a definite tendency for the smaller asteroids to occur farther from the sun. The group of asteroids from 3.0 to 3.5 AU from the sun contains only 23 percent of the bodies in 2.0 to 3.5 AU belt having absolute brightness magnitudes between 4.0 and 8.0, whereas it contains 95 percent of those having absolute brightness magnitudes between 12.0 and 13.0.

Asteroids fluctuate in brightness. These fluctuations may be attributed to two general causes, i. e., spotty surface or irregular shape. It seems probable that most fluxuations in the absolute brightness are due to the periodic presentation of different aspects of an irregularly shaped body, one which resulted from collision.

Few of the basic physical parameters for any of the asteroids are known. A few diameters are accurately known but no single mass of an asteroid has been found. Thus the structure, composition, and density are still to be determined.

The composition of the asteroids has been a subject of considerable speculation. Present investigators suggest that the asteroids are more terrestrial than Jovian in nature. That is, the original asteroids had a metal inner core, a silicate outer core, a mantle of chondritic compotion compacted by sintering, and an unconsolidated surface layer [Ref. B-9]. There is much speculation concerning asteroid structure, and our understanding of the cosmogony of the Solar System is partially dependent on this.

Several individual asteroids and groups are of some interest. Table B-3 lists the orbital elements of some of the major asteroids. Hidalgo and a group known as the Trojans must always have been outside the 4 AU limit. It has been speculated that the decrease in the mass of Jupiter by a factor of about 20 would necessarily have removed satellites from Jupiter and forced many of them into the Trojan positions. There is a question of the orbital stability of the Trojan asteroids because of planetary perturbations. It is possible that bodies can escape from or be captured into the Trojan positions. The present number of Trojans is 13 with six other suspected members.

TABLE B-3. ORBITAL ELEMENTS FOR SOME ASTEROIDS

<u>Cat. No.</u>	<u>Name</u>	<u>Diameter (Miles)</u>	<u>Opposition Magnitude</u>	<u>Semi-Major Axis of Orbit (AU)</u>	<u>Orbital Period (Years)</u>	<u>Eccentricity</u>	<u>Inclination to Orbit (Degree)</u>
1	Ceres	478.5	7.4	2.767	4.6	0.0802	10.60
2	Pallas	304.5	8.0	2.770	4.61	0.2394	34.82
3	Juno	118	8.7	2.670	4.36	0.2574	13.02
4	Vesta	236	6.5	2.361	3.63	0.0889	7.14
5	Astraea	49.7	9.9	2.577	4.13	0.1862	5.33
6	Hebe	69.6	7.0	2.42	3.77	0.2019	11.65
7	Iris	77.7	6.7	2.386	2.69	0.2309	5.47
8	Flora	56	7.8	2.201	3.27	0.1567	5.88
9	Metis	77.7	8.1	2.387	3.69	0.1233	5.60
12	Victoria	37.3	8.1	2.334	3.57	0.2190	8.38
15	Eunomia	?	7.4	2.644	4.30	0.1870	11.76
18	Melpomene	59	7.7	2.296	3.48	0.2176	10.15
20	Massalia	65.9	8.2	2.409	3.74	0.1426	0.68
192	Nausicaa	46.6	7.5	2.403	3.72	0.2445	6.87
324	Bamberga	59	7.3	2.68	4.39	0.3346	11.30
387	Aquitania	66.5	8.2	2.74	4.53	0.2383	17.97
433	Eros	15.5	7.2	1.458	1.76	0.2230	10.83
719	Albert	2.5	12.0	2.58	4.16	0.54	10.82
851	Wladilena	?	12.7	2.362	3.63	0.274	23.0
944	Hildago	21.7	11.0	5.71	13.7	0.65	43.06
1036	Gangmede	?	12.5	2.665	4.35	0.54	26.2
1221	Amor	1.6	16.0	1.973	2.77	0.45	--
--	Apollo	1.2	17.0	1.486	1.81	0.566	6.4
--	Adonis	0.6	19.0	1.969	2.76	0.78	1.5
--	Hermes	0.9	18.0	1.290	1.47	0.474	4.7
1566	Icarus	0.9	12.6	1.078	1.12	0.827	23.0

Hidalgo has a peculiar orbit and has the largest known semimajor axis, 5.79 AU, the greatest inclination to the ecliptic, 42.5 degrees, and one of the largest eccentricities, 0.656. Its orbit takes it almost to Saturn at aphelion and to Mars at perihelion.

A number of asteroids are known to have a semimajor axis of less than 2 AU. The most interesting are Eros, Icarus, and Geographos. Eros, very irregularly shaped, is bright, easy to track, and passes within 2.3×10^7 km of the Earth.

Icarus which has the largest known eccentricity, 0.8266, passes within 5.7×10^6 km of Earth. It has the smaller semimajor axis, 1.0777 AU, and passes at perihelion within 2.8×10^7 km of the sun. This is the closest pass to the sun of any orbiting body except an occasional comet. These properties suggest it as a possible solar research bus to carry a payload toward the sun.

Geographos has the closest predictable approach to Earth, 4.8×10^6 km that has a good chance of recovery. It is small, less than 2 km in diameter.

The largest asteroids lie within the main body of the asteroid belt. There are at least 15 asteroids of more than 100 miles in diameter and 9 asteroids more than 120 miles in diameter. Some of these may be heated by short-lived radioactive elements and the study of these will undoubtedly give important and vital evidence toward an understanding of the origin of the Solar System.

COMET ENVIRONMENT

Comets are perhaps the most mysterious and unpredictable members of the solar system. It is generally agreed that they are periodic in nature and are permanent members of the solar system even though some of them have very long orbital periods. Fewer than 100 comets have periods shorter than 100 years and only 40 or 50 have periods between 100 and 1000 years. The periods of the remainder are very uncertain because their orbits are nearly parabolic.

Generally, comets with periods of less than 8 years are called short-period comets and are under the influence of the massive planet Jupiter while comets of periods greater than 1000 years are called long-period comets. Halley's famous comet is one of the few hybrids between the two classes.

The comets are believed to be very loosely constructed, low density objects from 1 to 100 km in diameter. They consist of a nucleus of a conglomerate of meteoric materials in an icy matrix of substances such as water, ammonia, methane, and carbon dioxide. This nucleus is surrounded by a gaseous sheath called the coma.

Comets arrive from all directions with about equal probability, that is, some of their orbits are highly inclined to the ecliptic. At about 5.0 AU comets become visible as the result of the sun's heating the frozen matter of the nucleus. This heating causes internal explosions which eject gas and dust in all directions. Solar radiation pressure and the solar wind force the gas and dust to stream from the nucleus in a direction outward from the sun forming tails which have been observed to be as much as 320 million kilometers long.

Although comets may be enormous in size, their masses are exceedingly small, probably less than 1/10 000 the mass of Earth. The mass is concentrated in the nucleus which is usually unobserved and is probably only a few miles in diameter.

Table B-4 lists several comets which have been observed at least three times and are expected to reappear as predicted [Ref. B-10, 11].

In this table P^* = period (in years).

w is the argument of perigee, or angle between the direction of the ascending node and the direction of the perigee (perihelion in heliocentric orbits).

Ω is the longitude of the node, measured in the plane of the equator from the direction of the vernal equinox to the direction of the ascending node, or intersection of the orbit with the equator.

i is the inclination, or angle between the plane of the orbit and the plane of the equator.

e is the eccentricity, or the ratio of the distance from the center of the orbit to the focus.

a is the semi-major axis or mean distance.

$q = a(1 - e)$ the perigee distance.

* The reader is directed to Reference 13 for further clarification of nomenclature.

TABLE B-4. OBSERVED COMETS [Ref. B-11]

Comet	Recent Perihelion Date and Return Number		Mean Orbital Elements Equinox 1950							
	P (Year)	w	Ω	i	e	q (AU)	a (AU)			
Encke	1961.10	46	3.30	185	335	12.4	0.847	0.339	2.21	
Grigg-Skjellerup	1957.09	9	4.90	356	215	17.6	0.704	0.855	2.89	
Temple	1957.10	12	5.28	191	119	12.5	0.545	1.38	3.0	
Kopff	1958.05	8	6.3	160	120	5	0.556	1.51	3.4	
Giacobini-Zenner	1959.82	7	6.5	172	196	30.8	0.72	0.94	3.5	
Schwassmann-Wachmann	1961.68	6	6.53	358	126	3.7	0.384	2.155	3.50	
Wirtanen	1961.29	3	6.67	343	86	13.4	0.543	1.62	3.55	
Reinmuth	1960.90	3	6.7	45	296	7.0	0.46	1.93	3.6	
Brooks	1960.46	10	6.75	197	177	5.6	0.50	1.76	3.6	
Finlay	1960.67	7	6.85	321	42	3.5	0.705	1.07	3.6	
Borrelly	1960.45	7	7.01	351	76	31.1	0.604	1.450	3.67	
Faye	1955.17	14	7.42	201	206	10.6	0.565	1.655	3.80	
Whipple	1955.91	4	7.42	190	189	10.2	0.356	2.450	3.80	
Reinmuth	1958.23	4	7.67	13	124	8.4	0.478	2.03	3.90	
Oterma	1958.44	Annual	7.89	355	155	4.0	0.144	3.39	3.96	
Schaumasse	1960.29	6	8.18	52	86	12.0	0.705	1.195	4.05	
Wolf	1959.22	10	8.42	161	204	27.3	0.396	2.505	4.15	
Comas Sola	1961.26	5	8.57	40	63	13.5	0.577	1.775	4.19	
Vaisala	1960.35	3	10.5	44	135	11.3	0.635	1.745	4.79	
Schwass-W.	1957.36	Annual	16.1	356	322	9.5	0.132	5.53	6.4	
Neujmin	1948.96	3	17.9	347	347	15.0	0.774	1.54	6.8	
Crommelin	1956.80	6	27.9	196	250	28.9	0.919	0.744	9.2	
Olbers	1956.45	3	69.6	65	85	44.6	0.930	1.18	16.8	
Pons-Brooks	1954.39	3	70.9	199	255	74.1	0.955	0.775	17.2	
Halley	1910.30	29	76.2	112	57	162.3	0.967	0.587	17.8	

GALACTIC COSMIC RADIATION

Cosmic radiation consists of atomic nuclei traveling through interstellar space at very high speeds. These particles fill our galaxy and appear to come to Earth from all directions all without showing a preference for any area of origin in interstellar space. The source of this radiation is thought to be predominately from supernoval stars.

Various investigators suggest various cosmic ray compositions. These range from about 85 to 90 percent to be hydrogen nuclei (protons), 14 to 60 percent to be helium nuclei (alpha particles), and 1 to 4 percent to be the nuclei of heavier elements from, say, lithium to iron. The electron content of cosmic rays is insignificant. The protons make up about 2/3 of the total weight.

The energy spectrum of the primary particles is very broad, ranging from somewhat below 10^2 MeV (million electron volts) per nucleon (all of the atomic nuclei) at high fluxes to well over 10^{13} MeV per nucleon at very low fluxes. Hess and Badentscher [Ref. B-7] report that the average energy is about 3.6×10^3 MeV per nucleon and that predominant energy range is from 10^3 to 10^7 MeV.

Figure B-8 shows a kinetic energy as a function of the charged particle intensity for galactic cosmic radiation from Reference B-12.

The high energy cosmic particles interact with atoms of the atmospheres of planets producing secondary particles which are trapped by the planet's magnetic field. These secondary particles spiral along the lines of force to reflection points in each hemisphere of the planets. The trapped particles are probably protons and electrons and are located in two belts known as Van Allen radiation belts. Earth's Van Allen belt consists of an inner belt that extends from about 800 to 5500 miles above Earth and reaches to between 20 and 30 degrees above and below the geomagnetic equator. Earth's outer belt extends from 5500 to 20 000 miles and between 50 and 60 degrees above and below the geomagnetic equator.

Since Jupiter has an atmosphere (although it is unlike that of Earth) and a very strong magnetic field (many times that of Earth's) it is reasonable to expect that it has an extremely strong Van Allen radiation belt. This Jovian radiation hazard is, perhaps, the greatest single limitation of reliability of a spacecraft venturing close to Jupiter. Jupiter's radiation belts and fields are discussed in Appendix A.

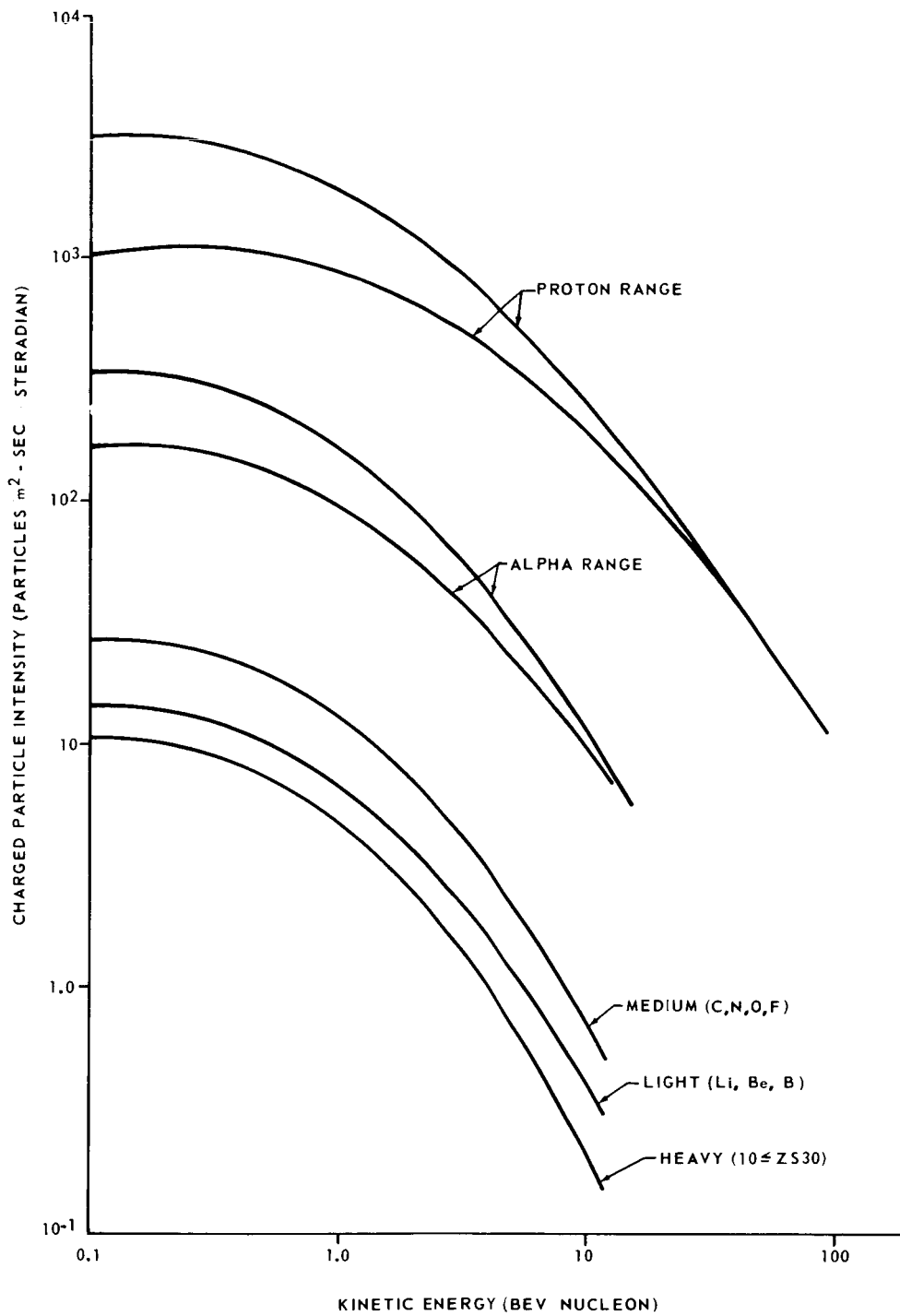


FIGURE B-8. INTEGRAL SPECTRA OF GALACTIC COSMIC RADIATION

Cosmic rays are affected by solar activity and are partially kept out of the solar system by some screening mechanism. This mechanism has been speculated to be the magnetic fields which travel with ejected solar gas and deflect away some of the cosmic rays. Peak values are observed during periods of low solar activity. Smith and Vaughan [Ref. B-10] suggest approximate galactic cosmic flux at minimum sunspot activity of $4 \text{ protons/cm}^2 - \text{sec}$ (assuming an isotropic flux) and an integrated yearly rate of about $1.3 \times 10^8 \text{ protons/cm}^2 - \text{sec}$ with an integrated yearly rate of about $7 \times 10^7 \text{ protons/cm}^2$.

Figure B-9 shows some of the more important components of the radiation environment in space in terms of the particle energy E , in MeV, and of the integrated particle flux above E , in particles/cm² - sec. These data include the cosmic ray primary flux and for the proton and electron fluxes at the center of Earth's inner and outer Van Allen belts. The intensity of the flux is affected by solar flare activity as indicated in the figure.

SOLAR WIND AND SPACE MAGNETIC FIELDS

Solar wind is one of three types of radiation emanating from the sun. The solar wind is a plasma which is composed of ionized hydrogen gas. Various estimates have been made for these proton intensities in the vicinity of Earth. Smith and Vaughan [Ref. B-10] give for the mean density:

$$0.5 \text{ AU} = \sim 20 \text{ hydrogen atoms/cm}^3$$

$$1.0 \text{ AU} = \sim 5 \text{ hydrogen atoms/cm}^3$$

$$1.75 \text{ AU} = \sim 2 \text{ hydrogen atoms/cm}^3$$

For the mean flux:

$$0.5 \text{ AU} = \sim 8 \times 10^8 \text{ hydrogen atoms/cm}^2/\text{sec}$$

$$1.0 \text{ AU} = \sim 2 \times 10^8 \text{ hydrogen atoms/cm}^2/\text{sec}$$

$$1.75 \text{ AU} = \sim 10^8 \text{ hydrogen atoms/cm}^2/\text{sec}$$

The mean velocity of the solar wind from 0.5 AU to 1.75 AU is taken to be 450 to 500 km/sec.

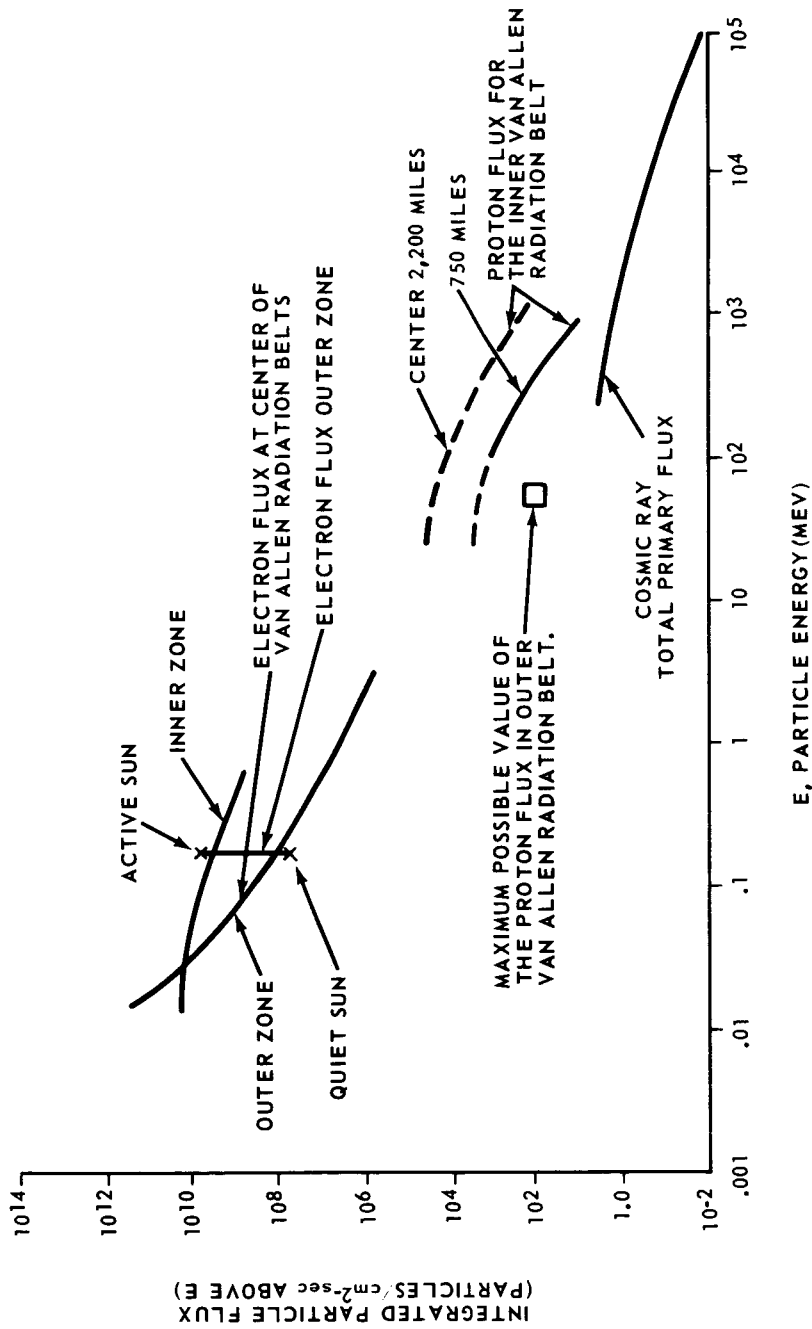


FIGURE B-9. PRIMARY COSMIC RAY AND VAN ALLEN BELT RADIATION ENVIRONMENT IN SPACE

Hare, et al. , have used for solar wind flux near Earth a range from 10^8 hydrogen atoms/cm² - sec with energy level of about 1 KeV for a quiet sun to about 10^{12} hydrogen atoms/cm² - sec of energy level of about 10 KeV for an active sun. The solar wind intensity is assumed to vary as the inverse of the square of the distance from the sun.

Interplanetary space contains magnetic fields. The sun possesses a well-ordered but relatively weak general field which has a magnitude of several gauss near the surface. Fast solar cosmic rays generated along with flares and solar winds are sometimes guided by this field to Earth and other planets.

The principal space magnetic field is from 0.5 to 1.75 AU solar distance; however, this does not exclude other fields. The strength of this field ranges from 0 to 100 gammas at 1.0 AU, averaging about 5 gammas. As expected, the strength of the field depends upon solar activity and fluctuations of one or two orders of magnitude may occur depending upon solar activity.

Figure B-10 shows the interaction of solar wind with a planetary magnetic field. The field is distorted by the wind with the principal features being the formation of a shock wave, a geomagnetic cavity which is produced by diffuse reflection of the solar wind, and neutral points where the total field vanishes. In the figure distorted field lines within the cavity are shown. The shock wave and the streamlines are drawn by analogy with fluid dynamics.

The magnetic field of Jupiter is extremely strong. Since the solar wind flux varies as the inverse of the distance from the sun, however, it is expected that some sort of a reaction as shown in Figure B-10 will occur in the Jovian field.

Earth's-trapped radiation provides a basis of developing estimates for the Jupiter-trapped radiation. Jupiter's radiation is discussed in Appendix A in some detail.

Earth-trapped radiation consists of two apparent belts, the inner and outer. The inner belt peak intensity occurs at something less than 2 Earth radii while the outer belt peak intensity occurs at more than 3.5 Earth radii at the geomagnetic equator. Figure B-11 shows the integral flux profiles for several energies of electrons and protons. The inner belt electron of the Van Allen belts are observed to have lifetimes of a year or more while the outer belt electrons have lives on the order of several days. The long lifetimes of the inner belt electrons suggest that their source may be from the interaction of cosmic rays and the atoms of the atmosphere.

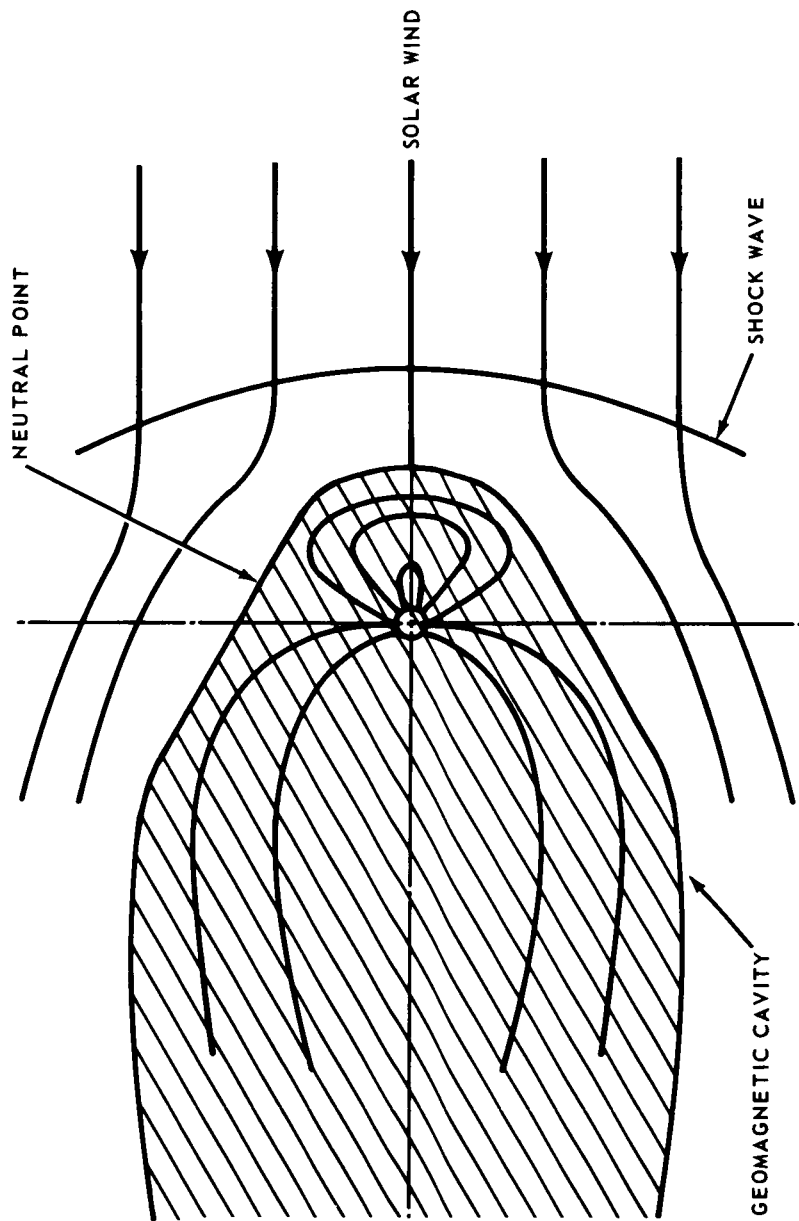


FIGURE B-10. INTERACTION OF SOLAR WIND WITH MAGNETIC FIELDS

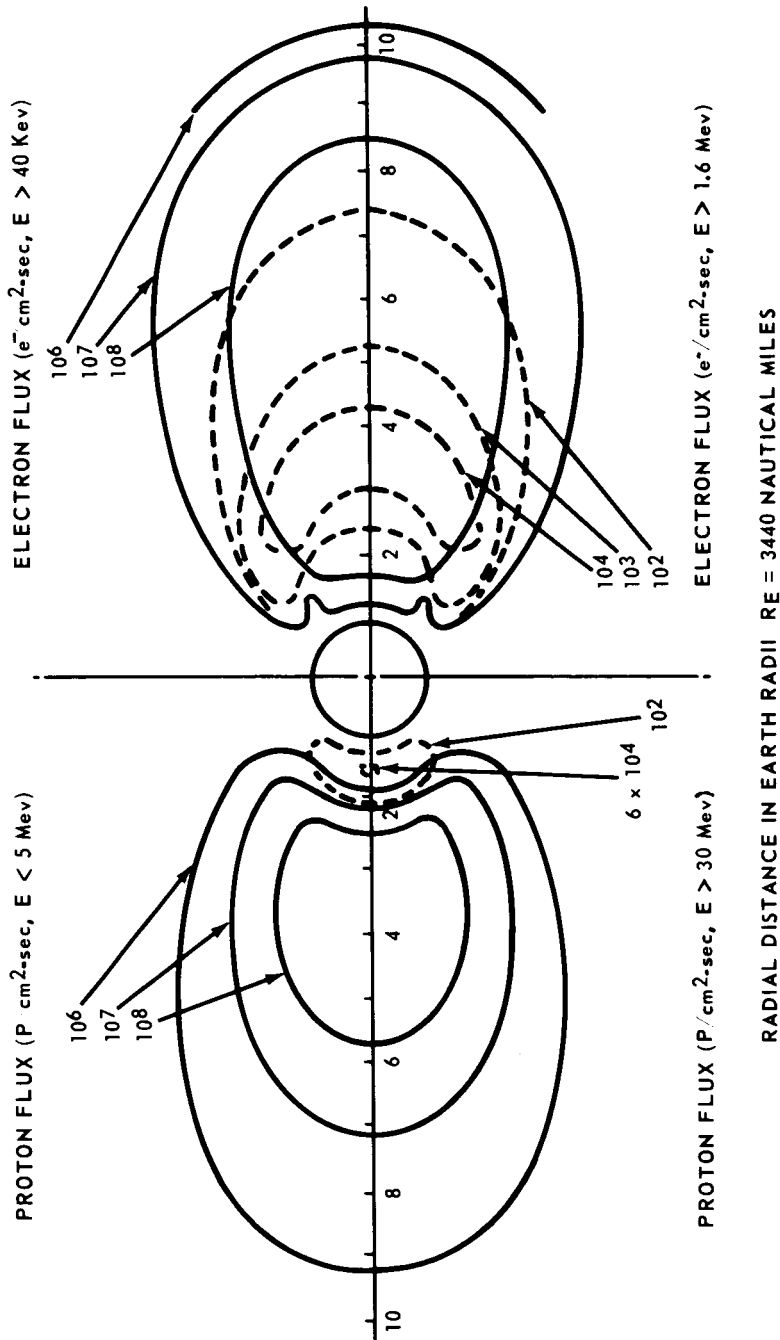


FIGURE B-11. EARTH TRAPPED RADIATION

One product of cosmic ray and atmospheric atoms is albedo neutrons which in turn decay, producing electrons and energetic protons. These particles are captured by the inner belt. The source of electrons for the outer belt is thought to be solar corpuscular radiation.

As previously discussed, a collisionless magnetohydrodynamic shock wave occurs at several Earth's radii beyond the Earth's magnetopause. This shock wave is the reaction between the Earth's magnetic field and solar wind. In the transition region between this shock wave and Earth's magnetosphere exist electron fluxes of 10^{10} electrons/cm² - second having energies between 1 and 10 KeV and proton fluxes of 10^7 protons/cm² - second having energies greater than 2 KeV. In this region the particles appear to be accelerated, have a random motion, originating from the solar plasma, and are presumably the source of outer-belt protons which are pumped into the belt during magnetic storms.

SOLAR FLARES

A potent hazard to space flight are high energy particles accelerated in flares on the sun. This radiation can be thought of as nonrelativistic flares and relativistic flares whose velocities are near the speed of light.

Intensities of nonrelativistic flares have exceeded 10^6 particles/cm² - sec with proton energies ranging from 10 to 500 MeV. Relativistic flares are uncommon, only 6 recorded between March 1942 and May 1960. The largest recorded in 1956 reached estimated peak intensities of 10^5 particles/cm² - sec for energies greater than 1 BeV. Figure B-12 shows an estimate for a severe nonrelativistic flare and an estimate for a relativistic flare.

Smith and Vaughan [Ref. B-10] and Roberts [Ref. B-12] report solar high energy particle radiation consisting predominately of hydrogen atoms (protons) and helium atoms (alpha particles) for an integrated yearly flux to be:

Energy > 30 MeV $N \sim 8 \times 10^9$ protons/cm² near solar maximum

$N \sim 5 \times 10^9$ protons/cm² near solar minimum

Energy > 100 MeV $N \sim 6 \times 10^8$ protons/cm² near solar maximum

$N \sim 1 \times 10^8$ protons/cm² near solar minimum

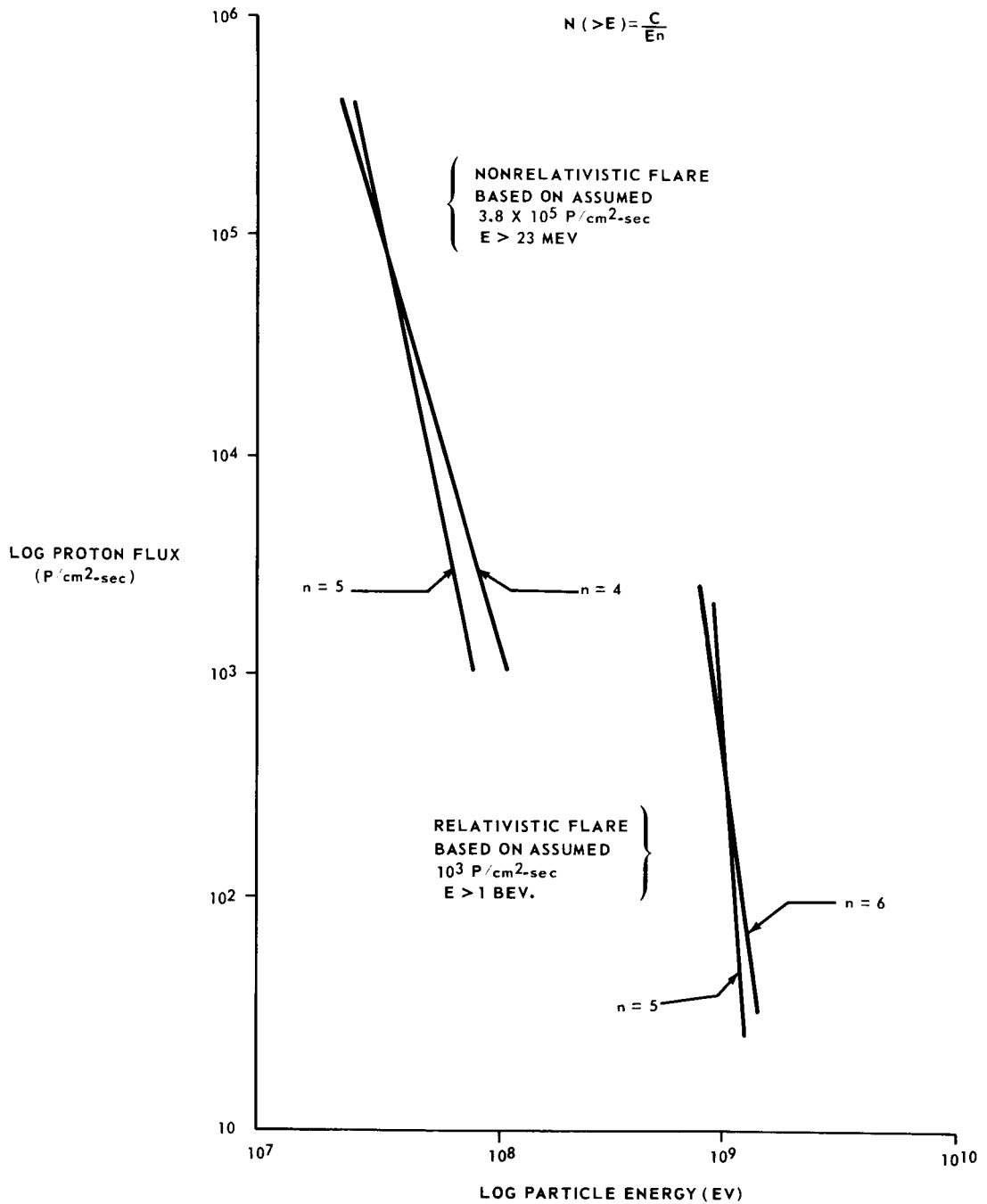


FIGURE B-12. ENERGY SPECTRUM OF TYPICAL RELATIVISTIC SOLAR FLARE AND A SEVERE NONRELATIVISTIC SOLAR FLARE

These data apply for a solar distance of 1.0 AU: For other distances, a rough estimate can be obtained by using a scale of R^{-2} for implied spatial continuity.

Solar flares seem to be closely associated with sunspot activity. Flares usually occur in the vicinity of sunspots, thus the probability, p , encountering a flare with total integrated flux, N , with energies greater than 30 MeV in one day is given in Figure B-13, where N_f is the number of occurrences of flares whose total integrated flux exceeded the largest recorded flare, and N_t is the time frame over which the flares were recorded. These data are from Roberts [Ref. B-13].

Solar flares last from hours to several days in duration. After a flare becomes visible, however, there are only a few hours at most before the corpuscular radiation arrives in the vicinity of the observer. To date, no satisfactory method or theory has been developed that will predict flare activity.

An attempt to predict solar flares is presented in Figure B-14. In this figure the last two solar cycles (16 and 17) have served as a model of the solar cycles 21 and 22. The minimum solar activity time for the 18th cycle was matched to the minimum for the 22nd cycle, and with this area as the reference, the 21st and 22nd cycle were plotted. The major solar flares on the new cycles are placed in the same positions they occupied on the previous cycles. This figure, taken from Reference 8, reflects only an estimate of the frequency of flares predicted for the time period 1972 to 1990.

Smith and Vaughan [Ref. B-10] report a spectral distribution model after the work of Roberts [Ref. B-13] and Smith [Ref. B-8]. This model flare event is:

$$N (>P) = N_o \exp (-p/p_o) \quad (8)$$

where

N = protons /cm² having rigidity greater than P ,

P = rigidity, or momentum per unit charge, in volts,

$P_o = 8 \times 10^7$ volts = constant, a value typical for large events

$$P = \sqrt{\frac{(E+MC^2)^2 - (M_o C^2)^2}{Ze}} \geq 0.235 \text{ bv} \quad (9)$$

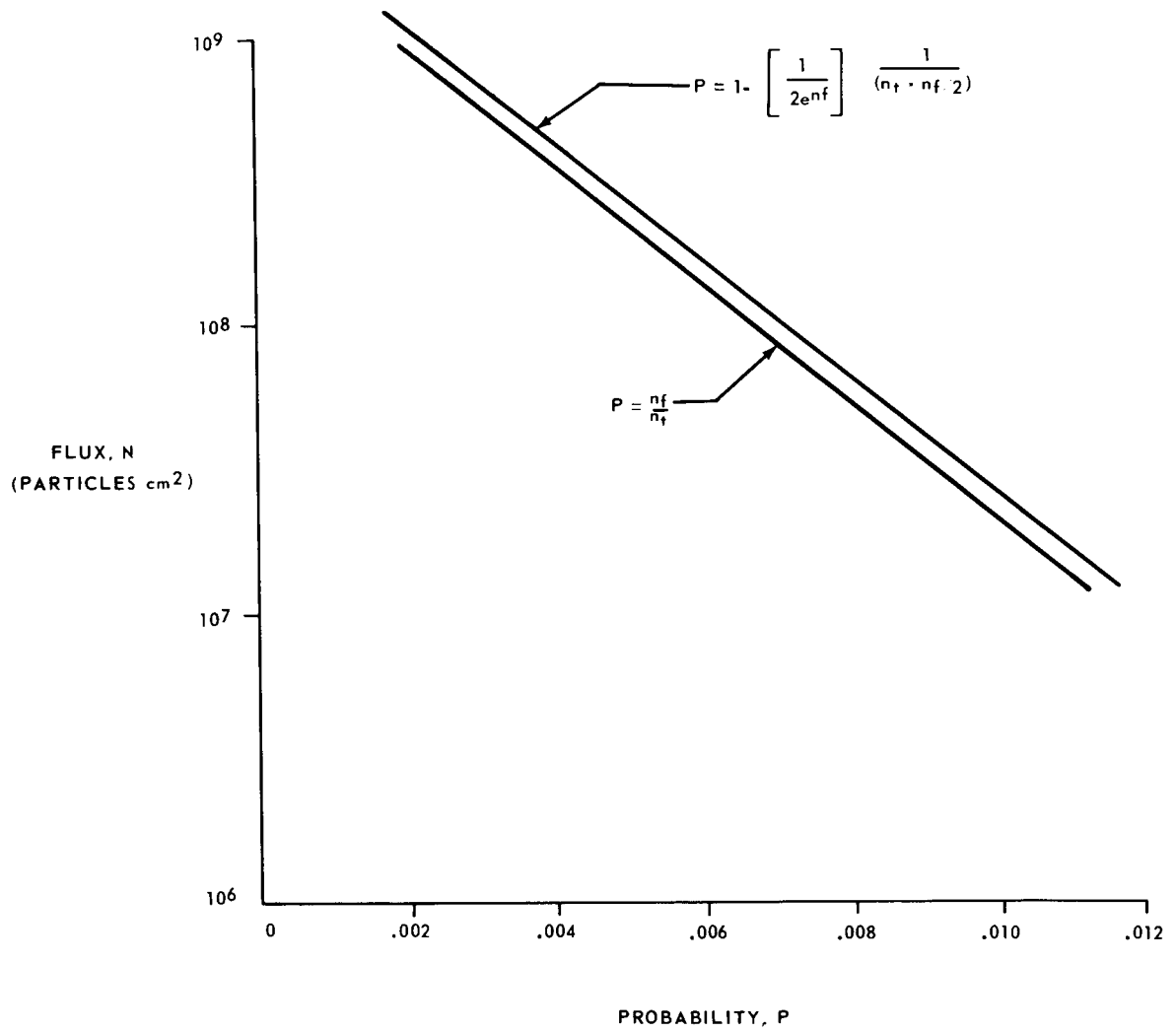


FIGURE B-13. THE PROBABILITY, p , OF THE OCCURRENCE OF A FLARE WHOSE FLUX IS EQUAL TO OR GREATER THAN N , AND WHOSE INDIVIDUAL PARTICLE ENERGIES ARE EQUAL TO OR GREATER THAN 30 MeV

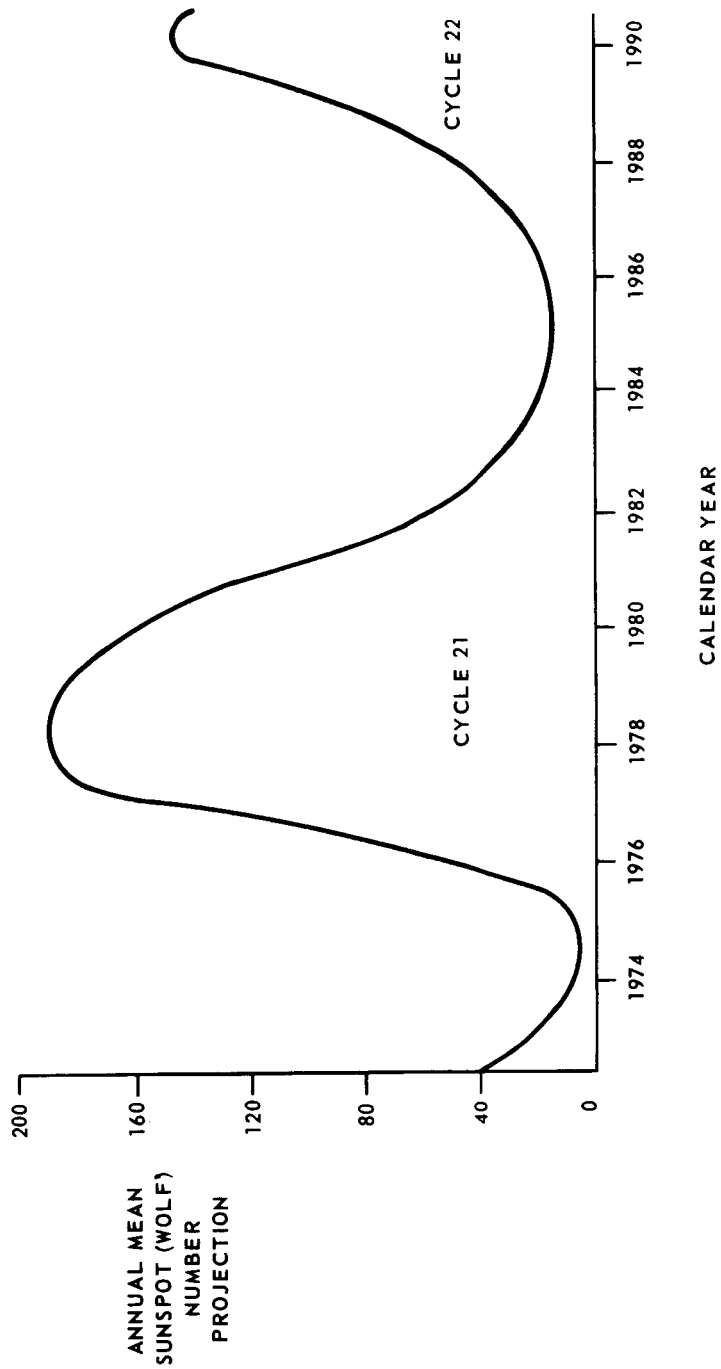


FIGURE B-14. SOLAR FLARE/SUNSPOT CORRELATION (CYCLES 21 AND 22 WERE PROJECTED FROM CYCLES 18 AND 19)

and

$E =$ proton energy in joules (4.8×10^{-12} joules = 30 MeV)

$M_0 C^2 =$ proton rest energy = 1.5×10^{-10} joules

$e =$ proton charge = 1.6×10^{-19} coulombs

$Z =$ atomic number (stripped of electrons)

$N_0 =$ value which changes with flare size and is dependent upon P_0 .

The time-dependent spectra is given by:

$$N = N_{\max.} e^{-k(t_{\max.}/t)}$$

where

$N =$ number of particles /cm²-sec

$N_{\max.} =$ maximum number of particles/cm²-sec occurring during the event

$t_{\max.} =$ onset - delay time to $N_{\max.}$

$t =$ onset - delay time to N

$k =$ factor dependent on type of energy spectrum exhibited by the flare.

Figure B-15 shows proton fluxes which exceed three typical energeticals as a function of time. As noted on the figure, the flux is very dependent on the energy level. These data are from Schulte and Shipley [Ref. B-14].

A model for the solar events near Earth has been suggested by Reference 16. The integral spectrum near Earth is given by

$$N (> P) = N_0 e^{-P/P_0}, \quad P \geq P_c \quad (11)$$

$$N (< P) = N_0 e^{-P_c/P_0}, \quad P \leq P_c \quad (12)$$

$P_c =$ cut-off rigidity.

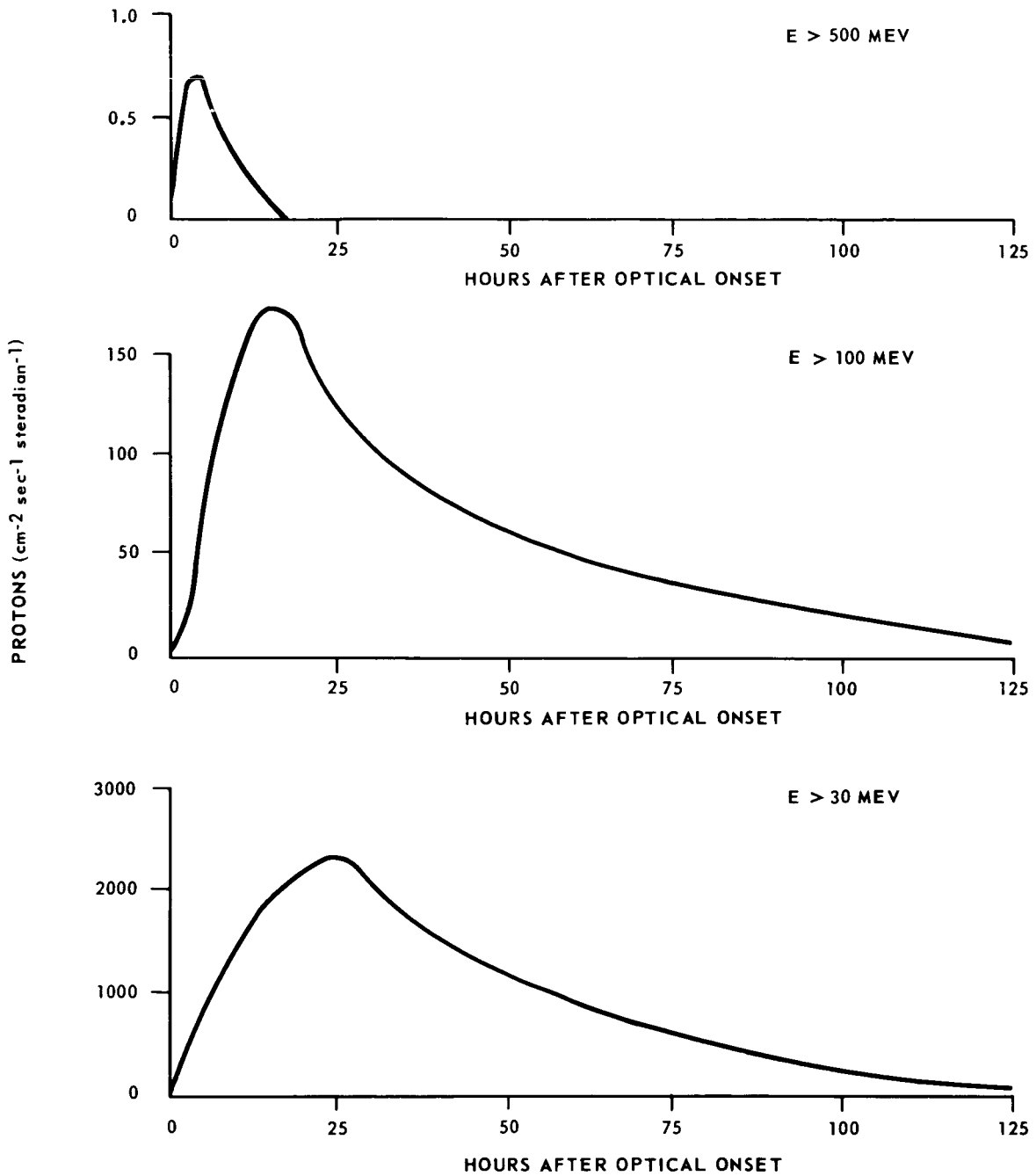


FIGURE B-15. TIME DEVELOPMENT OF MODEL FLARE EVENT

The intensity is zero for all rigidities below P_c .

The cut-off rigidity is

$$P_c = \frac{2.5 \times 10^9}{r^2} \left(\frac{2 + \cos^3 \lambda - 2(1 + \cos^3 \lambda)^{1/2}}{\cos^2} \right) \quad (13)$$

where

r = geocentric radius (cm)

λ = geomagnetic latitude.

In short, uncertainties in event frequency, event intensity, and particle transport make prediction of solar radiation incident in the spacecraft highly speculative.

RADIATION PROPERTIES OF THE SUN

The thermal radiation properties of the sun can be grouped in many ways. References B-8 and B-15 were the primary data sources in this section.

The solar radiation constant varies with solar distance. It is fairly well known from 0.5 AU to 1.75 AU and has the value at 1.0 AU to be 1400 watts/m² or 1.95 cal/cm²/min. This value should vary as the inverse of the square of R , the distance from the sun in astronomical units. The variation of the solar constant with R is given in Table B-5. The brightness of the sun is 200 000 candles/cm². The solar illumination can be found by

$$13.4R^{-2} \text{ lumen/cm}^2 = 1.34 \times 10^5 R^{-2} \text{ luxes} \quad (14)$$

Where R = distance from sun (astronomical units)

The visible and infrared radiation energy distribution can be approximated by that of a 6000° Kelvin black body. The fraction of solar radiation above 7000 Å (Angström) is equal to 52 percent about 4000 Å = 91 percent, and between 3000 Å and 30 000 Å = 97 percent.

The fraction of ultraviolet solar radiation below 4000 Å is 9 percent, below 3000 Å is 1.2 percent, below 2000 Å is 0.02 percent, and below 1000 Å is a variable 10⁻⁴ percent. The principal line emission fluxes at 1.0 AU are:

Lyman Alpha HI (1216Å)	:	60×10^{-8} watt/cm ²
HE II (304Å)	:	3×10^{-8} watt/cm ²
H I (1026Å)	:	2×10^{-8} watt/cm ²
C III (977Å)	:	2×10^{-8} watt/cm ²
Si II (1817Å)	:	2×10^{-8} watt/cm ²

TABLE B-5. VARIATION OF SOLAR CONSTANT WITH SOLAR DISTANCE

<u>SOLAR DISTANCE</u> (astronomical units)	<u>SOLAR CONSTANT</u> (watts/m ²)
0.5	5600
0.6	3889
0.7	2857
0.8	2187
0.9	1728
1.0	1400
1.1	1157
1.2	972
1.3	828
1.4	714
1.5	622
1.6	547
1.7	484
1.75	457
2.0	350
2.5	224
3.0	155
3.5	114
4.0	87.5
4.5	69
5.0	56
5.2	52

The X-ray flux will vary during periods of solar activity and one or two orders of magnitude increase may occur. In the 20 to 100 Å region the X-ray flux is 6×10^{-8} watt/cm², the 8-20 Å region it is 2×10^{-10} watts/cm², and the 2-8 Å region, the flux is 5.5×10^{-11} watts/cm².

The strength of line emission flux also varies as the inverse of R^2 so the flux at Jupiter in the 20- to 100-Å region is 2.22×10^9 watt/cm²; the 8- to 20-Å region the flux is 7.4×10^{-12} watt/cm²; and the 2-8-Å region the flux is 2.04×10^{-12} watt/cm².

The solar radiation pressure at 1 AU for a black body = 4.5×10^{-5} dyne/cm² and for a 100-percent reflecting body is 9×10^{-5} dynes/cm². To calculate the radiation pressure at any solar distance the following relation can be used:

$$P = S/c \text{ for black body}$$

$$P = 2S/c \text{ for 100 percent reflecting body}$$

Where P = radiation pressure

S = solar constant at specified solar distance

c = speed of light

The solar radio noise varies with sunspot activity and during solar storms may increase from 1 to 8 orders of magnitude. The variation with sunspots is greatest between wavelengths of 6 to 200 cm, with the spectral power showing a range of variation of 4 orders of magnitude. The solar radio noise power flux is given by

$$\text{Noise Power Flux} = \frac{(4.5 \times 10^{-31}) (f)^{1.1}}{R^2} \text{ watt/m}^2/\text{cps} \quad (15)$$

Where f = frequency, cycles/second

R = astronomical units distance from sun

For a quiet sun, the approximate noise power at 1.0 AU is

10^{-19} watt/m²/cps at 1.0 cm wavelength to

10^{-22} watt/m²/cps at 400 cm wavelength

The characteristics of the solar noise is dependent on solar activity. Roberts [Ref. B-16] classes these into 6 groups according to their origin (from nonthermal to synchrotron and thermal) and lists their frequencies.

REFERENCES

1. Volkoff, John J.: Protection Requirements for the Resistance of Meteoroid Penetration Damage of Interplanetary Spacecraft Systems. Technical Report Number 32-410, July 1964.
2. Alexander, W. M.; McCracken, C. W.; Secretan, L. and Berg, O. E.: Rocket, Satellite, and Space-Probe Measurements of Interplanetary Dust. Trans. Amer. Geophys. Union 43, 1962, pp. 351-360.
3. Whipple, Fred L.: On Meteoroid and Penetration. The Journal of Astronautical Sciences, vol. 10, no. 3, Fall, 1963.
4. McCoy, T.: MSFC Contract NAS 8-2550. Northrop, presented June 14, 1962.
5. Parkinson, J.: MSFC Contract NAS 8-11285. Aerojet General, presented May 26, 1965.
6. Dalton, C.: MSFC Working Paper Number R-AERO-Y-77-66, January 26, 1966.
7. Dalton, Charles C.: Meteoroid Flux and Puncture Models. Aero-Astrodynamic Laboratory Research Review Number 6, to be published, NASA-MSFC, Huntsville, Alabama.
8. Smith, R. E.: Space Environment Criteria Guidelines for use in Space Vehicle Development (1965 Revision). TM X-53273, MSFC, Huntsville, Alabama, May 27, 1965.
9. Fish, R. A.; Goles, G. G. and Anders, E.: The Record in the Meteorites, III. On the Development of Meteorites in Asteroidal Bodies. Astrophys. Journal 132.
10. Smith, R. E. and Vaughan, O. H.: Space Environment Criteria Guidelines for use in Space Vehicle Development, 1967 Revision, NASA TM X-53521, February 1, 1967.
11. Allen, C. W.: Astrophysical Quantities. Athlone Press, University of London, 1963.

REFERENCES (Concluded)

12. Hove, L. E. and others: Final Technical Report of a Study of Jupiter Flyby Mission. FZM-4625, General Dynamics, May 17, 1966.
13. Roberts, W. T.: Solar Flare Environment. NASA TM X-53216, MSFC, Huntsville, Alabama, March 12, 1965.
14. Schulte, H. J. and Shipley, E. N.: Models for Space Environmental Hazards. Radiation. Bellcom, Incorporated, Washington, D. C. January 31, 1963.
15. Nominal Nature Environment for Application to Advanced Manned Planetary Mission Program Studies. Planetary Atmosphere Section, ASTD, Space Environment, Manned Spacecraft Center, Houston, Texas, July 1, 1964.
16. Roberts, W. T.: Space Radiations: A Compilation and Discussion. NASA TM X-53018, MSFC, Huntsville, Alabama, March 5, 1964.

BIBLIOGRAPHY

Berkner, L. V. and Uishaw, H.: Science in Space. McGraw-Hill, Inc., 1961.

Broadway, N. J.; King, R. W. and Palinchak, S.: Space Environmental Effects on Materials and Components, vol. I. Redstone Scientific Information Center, RSIC-150, Redstone Arsenal, Alabama, April 1964.

Heitchue, R. D.: Space Age Fundamentals. Douglas Report SM-47656, Douglas Aircraft Company, Incorporated, 1964.

Hess, R. and Badentscher, R.: Space Radiation as an Environmental Constituent. Battelle Memorial Institute, REIC Memorandum Report Number 19, 1960.

Kendrick, J. B., ed.: TRW Space Data, Third ed., TRW Systems Group, TRW Incorporated, 1967.

LeGalley, D. P. and Rosen, A., eds.: Space Physics. John Wiley & Sons, Inc., 1964.

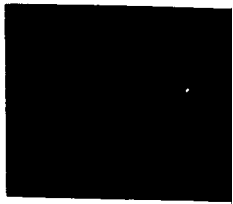
Natural Environment and Physical Standards for the Apollo Program. Office of Manned Space Flight, Washington, D. C., NASA, M-D E 8020.008B, SE 015-001-1, April 1965.

Ordway III, Frederick I., ed.: Advances in Space Sciences and Technology. Vol. 3, Academic Press, 1961.

Seifert, H. S., ed.: Space Technology, John Wiley & Sons, 1959.

Space Radiation Guide. TDR Number AMRL-TDR-62-86, August 1962.

APPENDIX C
RADIO OCCULTATION EXPERIMENTS



APPENDIX C

RADIO OCCULTATION EXPERIMENTS

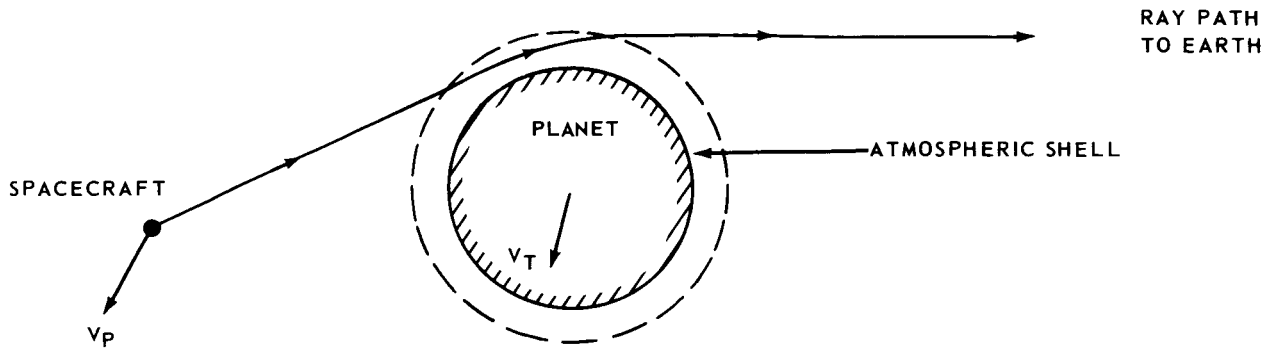
INTRODUCTION

Following the marked success of the Mariner 1964 flyby mission to Mars, the use of the radio occultation technique for probing planetary atmospheres has become a powerful tool in unmanned planetary exploration. This appendix discusses the application of these techniques to the study of the Jovian upper atmosphere. Specifically described are two probing methods, one using the occultation of a single orbiting spacecraft around Jupiter, while the second method employs two orbiting vehicles (sometimes referred to as the mother-daughter concept).

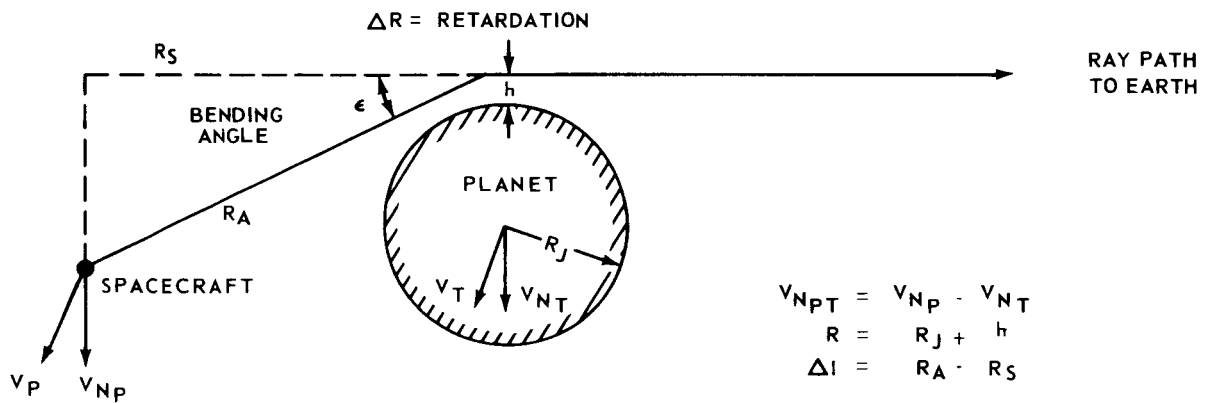
The use of the radio occultation technique was first suggested by Kliore, Cain, and Hamilton [Ref. C-1]. Fjeldbo and Eshleman [Ref. C-2] have also examined the single frequency bistatic radio occultation method, and in a companion paper [Ref. C-3], Fjeldbo et al. proposed a two frequency method for the study of planetary atmospheres and ionospheres. Sodek [Ref. C-4] has discussed a specific radio occultation experiment for a Jovian flyby mission. The reader is referred to these papers for details on the various techniques; this appendix will be confined to an examination of the feasibility of probing the Jovian upper atmosphere, and will present only requisite mathematical detail.

As long as a spacecraft is traveling in interplanetary space, the radio path from spacecraft to Earth will be a straight line, and the only Doppler component present will be due to the radial velocity of the spacecraft with respect to the earthbound communication station. As the spacecraft passes behind a planet, as illustrated schematically in Figure C-1 (a), the planetary atmosphere will be traversed by the radio ray path to Earth station. Because the planetary atmosphere will have a refractive index greater than unity, the ray path will be "bent," and the radio signal will be retarded because of the atmosphere. Referring to the simplified schematic of Figure C-1 (b), these effects are labeled ΔR for the retardation and Δl for the increase in path length. Following Kliore et al., and using the simplified geometry, it is seen that

$$R_s = R_a \cos \epsilon \quad (1)$$



(A) BASIC GEOMETRY OF OCCULTATION EXPERIMENT



(B) SIMPLIFIED GEOMETRY

FIGURE C-1. RADIO OCCULTATION GEOMETRY

which for small ϵ may be approximated as

$$R_s = R_a \left(1 - \frac{\epsilon^2}{2} \right) \quad . \quad (2)$$

The apparent increase in path length is then

$$\Delta l = R_a - R_s = \epsilon^2 \frac{R_a}{2} \quad . \quad (3)$$

Since for either a flyby or orbiter, the bending angle will be a function of altitude h and consequently a function of time, there will be a Doppler component given by

$$\dot{\phi}_l = \frac{d}{dt} (\Delta l) = \frac{d}{dt} (\Delta l) \frac{dh}{dt} \quad . \quad (4)$$

The retardation effect will also introduce a Doppler component, and the net Doppler shift for the radio signal will be

$$\begin{aligned} \dot{\phi} &= \frac{d}{dt} (\Delta l) + \frac{d}{dh} (\Delta R) \\ &= \frac{d}{dh} [\Delta l + \Delta R] \frac{dh}{dt} \\ &= \frac{d}{dh} \left[R_a \frac{\epsilon^2}{2} + \Delta R \right] \frac{dh}{dt} \quad . \end{aligned} \quad (5)$$

It is necessary to derive expressions for the bending angle ϵ and the retardation ΔR as functions of the altitude h . Using these expressions together with precise knowledge of position and velocity of both spacecraft and planets and an expression for $\frac{dh}{dt}$, it is possible to compute the scale height of the planetary atmosphere from Doppler and phase path increase measurements. The deviations of these expressions are beyond the scope of this appendix and necessary equations are simply summarized in the paragraph below.

Using a model atmosphere where refractivity is given by

$$N(h) = N_s e^{-\beta h} \quad (6)$$

where N_s = "surface" refractivity and β = inverse scale height, Kliore et al., have shown that

$$\epsilon \approx 2 \times 10^{-6} N_s e^{-\beta h} \beta \sqrt{\frac{\pi R}{2\beta}} \quad (7)$$

and

$$\Delta R \approx 2 \times 10^{-6} N_s e^{-\beta h} \sqrt{\frac{\pi R}{2\beta}} \quad (8)$$

The expression $\frac{dh}{dt}$ may be obtained from

$$t = \frac{1}{V_{n_{pt}} \left[1 - \left(\frac{\rho}{\gamma} \right)^2 \right]^{1/2}} \left[h + \frac{a}{\beta} \left(1 - e^{-\beta h} \right) \right] \quad (9)$$

where t is the time to occultation, and

$$a = 2 \times 10^{-6} R_a k N_s \left(\frac{\pi R_j}{2} \right)^{1/2} \quad (10)$$

The preceding brief resume of radio occultation methods was concerned with techniques specially derived for a Martian flyby. The expressions for ϵ and ΔR involve approximations where the product βR is assumed to be quite large. This approximation should hold also for the Jovian atmosphere above the cloudtops. Its validity for the atmosphere beneath the cloudtops is less certain, and lack of knowledge of even the gross characteristics of this region prevent further evaluation. Secondly, the derivations do not include the effects of losses. These losses are due to refractive defocusing primarily, but other loss mechanisms might be present in the lower Jovian atmosphere. It is not anticipated that either of these factors would limit the utility of the radio occultation method for probing the atmosphere above the cloudtops. In this case, the reference level, or "surface," refractivity N_s would be that of the cloudtop level.

OCCULTATION MEASUREMENTS FROM A SINGLE ORBITING VEHICLE

The performance of a single frequency radio occultation experiment using the JOVE vehicle is straightforward and is shown schematically in Figure C-1. The experiment is critically dependent only upon a sufficient communications margin. It is clear that a margin sufficient to maintain phase lock between spacecraft and DSIF must be available if telemetry is to be returned to Earth. An additional requirement is imposed, however, because of the refractive defocusing effects of the Jovian upper atmosphere.

The performance of the down link from JOVE to DSIF is summarized in Table C-1. The communications margin of 25.7 dB is probably somewhat conservative. This communications margin should be more than adequate for probing the atmosphere above the cloudtops.

There is one additional point which would separate Jovian occultation experiments from a Martian experiment. The radial velocities of a Jovian orbiter relative to Earth may be quite high with Doppler frequencies on the order of 40 KHz. This might require some modification of the DSIF tracking receivers.

OCCULTATION MEASUREMENTS USING AN ORBITAL PAIR OF VEHICLES

An attractive possibility for measurements on planetary atmospheres and ionospheres involves the use of a pair of orbiting vehicles as illustrated schematically in Figure C-2. Such a concept was dubbed the mother-daughter technique by Harrington et al. [Ref. C-5] and has been discussed in Reference C-6 as a tool for meteorological analysis.

The mother-daughter technique is particularly attractive for exploring Jupiter's atmosphere for two reasons. First, the possibility of a direct probe or lander is quite remote; consequently, information on the Jovian atmosphere must be obtained by indirect means. Second, the orbits dictated for the JOVE mission require periapses of five to seven Jovian radii, making the use of conventional topside sounders for obtaining ionospheric profiles impossible without

TABLE C-1. COMMUNICATIONS CIRCUIT CALCULATION
JOVE-TO-GROUND DOWN-LINK DISTANCE

5.5 AU, power = 100 watts, antenna gain = 40 dB (20 ft dish).

1.	Total transmitted power	=	20 dBw
2.	s/c circuit loss	=	-6.6 dB
3.	s/c antenna gain	=	+40.00 dB
4.	s/c pointing loss	=	-1.5 dB
5.	Space loss	=	-278.7 dB
6.	Polarization loss	=	-3.00 dB
7.	Ground antenna gain	=	+61.70 dB
8.	Ground transmission loss	=	-0.8 dB
9.	Net circuit loss	=	-188.90 dB
10.	Total received power	=	-169.9 dBw
11.	Receiver noise spectral density (T = 50° K)	=	-211.60 dB/cps
12.	Carrier modulation loss	=	-3.0 dB
13.	Carrier APC BW	=	+13.0 dB/cps
14.	Threshold SNR	=	+1.0 dB
15.	Threshold carrier power	=	-197.60 dB
16.	Performance margin	=	+25.70 dB

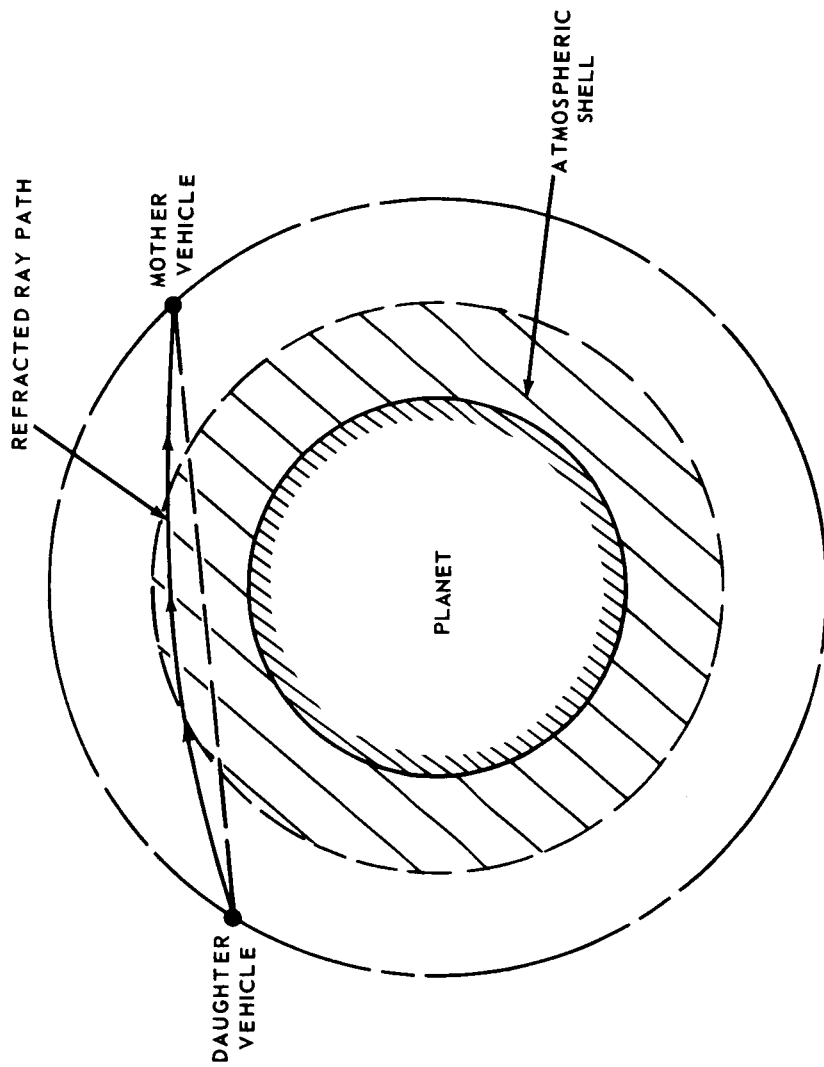


FIGURE C-2. ORBITAL PAIR OCCULTATION EXPERIMENT (SCHEMATIC)

orders of magnitude improvements in topside sounder capabilities. The use of Fjelbdo's two frequency method for obtaining ionospheric experiments between an orbital pair would overcome this difficulty.

The attractiveness of attempting such an experiment on a Jupiter mission is thus clearly established. It remains, however, to determine whether the required performance can be achieved within weight and power restrictions imposed on JOVE.

Several possibilities were examined for the orbital pair mission. One of the most attractive of the cases examined is summarized in Figure C-3. The JOVE vehicle is in the outer orbit and is carrying a small daughter vehicle before $T = 0$ (apoapsis). At apoapsis, the spin stabilized daughter is off-loaded and given a ΔV of -1 km/sec with respect to the mother (JOVE) vehicle. This establishes the daughter in the lower orbit shown on the diagram. Note that three occultations occur during the period from 12.88 days to 14 days after separation. Note also the large communications distance between the two vehicles at the times of atmospheric occultation. As will be shown in the subsequent discussions, these communications distances will, together with other constraints, be key factors in the decision not to attempt the two-vehicle experiment.

The performance data on the communications link between mother and daughter are summarized in Tables C-2 and C-3. Several key factors which should be noted are:

1. The daughter vehicle is spin stabilized and carries a Pioneer type 11 dB gain antenna. The vehicle is oriented such that omnidirectional coverage is in the plane of the orbits of the two satellites.
2. The daughter is assumed to carry a 10-watt transmitter in the data of Table C-2, and a 100-watt transmitter in the data of Table C-3.
3. The medium gain antenna (25 dB) on the JOVE spacecraft is assumed to track the daughter vehicle at all times.

Referring to the data of Table C-2, it is seen that the communications margin is -7.8 dB, which does not include any refractive defocusing losses. If the transmitter power is increased by 10 dB to 100 watts, the communications margin increases to $+2.2$ dB as shown in Table C-3. Neither of these figures would allow a high probability of mission success. While the 2.2 dB margin does make communication barely possible, any additional losses such as refractive losses would degrade this figure well below the marginal level. The requirement for providing 100 watts of RF power is also severe and would result in a much heavier daughter vehicle than could be accepted on a first Jovian mission.

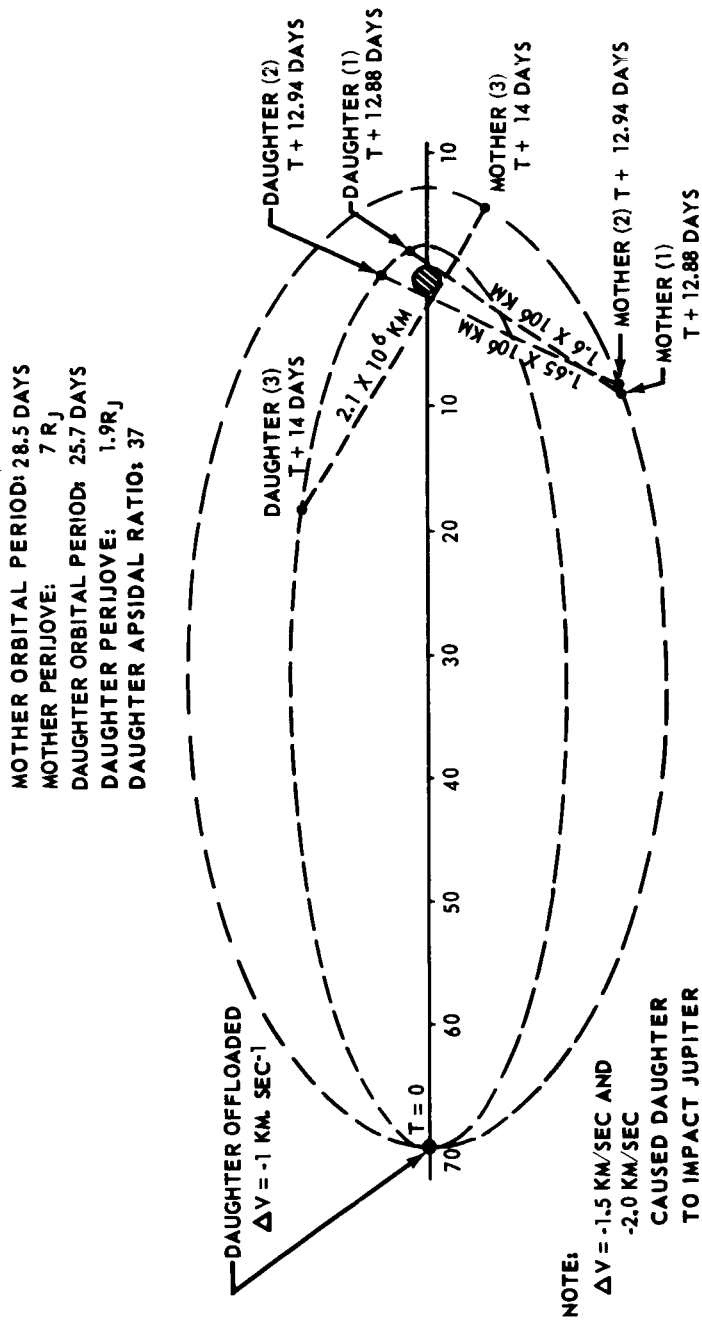


FIGURE C-3. OCCULTATION GEOMETRY FOR $R_{pm} = R_j$, APSIDAL RATIO = 10

TABLE C-2. COMMUNICATION CIRCUIT CALCULATION
(10 WATTS POWER)

Daughter-to-Mother Link

Distance = 2.0×10^6 km, = .0133AU

Antenna Gain = 11 dB (pioneer type turnstile)

1.	Total transmitted power	=	10 dBw
2.	Daughter circuit loss	=	-6.60 dB
3.	Daughter antenna gain	=	11.00 dB
4.	Daughter pointing loss	=	-1.00 dB
5.	Space loss	=	-225 dB
6.	Polarization loss	=	-3.00 dB
7.	Mother antenna gain	=	25.00 dB
8.	Mother transmission loss	=	-0.80 dB
9.	Net circuit loss	=	-192.30 dB
10.	Total received power	=	-182.40 dBw
11.	Receiver noise spectral density (T = 1000° K)	=	-198.60 dBw/cps
12.	Carrier modulation loss	=	-3.0 dB
13.	Carrier APC BW	=	13.0 dB/cps
	Carrier Performance Tracking (one-way)		
14.	Threshold SNR in $2B_L$	=	0.0 dB
15.	Threshold carrier power	=	-185.60 dBw
16.	Performance margin	=	-7.8 dB

TABLE C-3. COMMUNICATION CIRCUIT CALCULATION
(100 WATT POWER)

Daughter-to-Mother Link

Distance = 2.0×10^6 km = 0.0133AU

Antenna gain = 11 dB (pioneer type turnstile)

1.	Total transmitter power	=	20 dBw
2.	Daughter circuit loss	=	-6.60 dB
3.	Daughter antenna gain	=	11.00 dB
4.	Daughter pointing loss	=	-1.00 dB
5.	Space loss	=	225 dB
6.	Polarization loss	=	-3.00 dB
7.	"Mother" antenna gain	=	25.00 dB
8.	"Mother" transmission loss	=	-0.80 dB
9.	Net circuit loss	=	-192.40 dB
10.	Total received power	=	-172.40 dBw
11.	Receiver noise spectral density (T = 1000° K)	=	-198.60 dBw/cps
12.	Carrier modulation loss	=	3.0 dB
13.	Carrier APC BW	=	13.0 dB/cps
	Carrier performance tracking (one-way)		
14.	Threshold SNR in $2B_L$	=	0.0 dB
15.	Threshold carrier power	=	-185.60 dB
16.	Performance margin	=	+2.20 dB

SUMMARY AND RECOMMENDATIONS

The single vehicle occultation experiment has been shown to be feasible within constraints imposed on the JOVE vehicle. Since this is essentially a "free" experiment using the spacecraft telemetry system, it should be performed. A more detailed study of possible modifications required on the DSIF facilities (primarily tracking receivers) should be undertaken.

Present ground facilities do not permit the performance of the two-frequency experiments proposed by Fjeldbo. No detailed analysis of this method was done during the current study; however, the possibilities offered in determination of ionospheric profile in addition to atmospheric density profile make this experiment worthy of further consideration should ground stations become available. The inclusion of the necessary instrumentation on board a vehicle of the JOVE class should be possible with present configuration constraints.

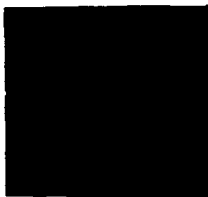
The mother-daughter concept is an effective one for studying planetary atmospheres and ionospheres provided low-altitude near circular orbits are possible for the orbital pair. Such orbits are not feasible on a first Jovian mission, and the large communications distances rule out the use of this technique for a daughter vehicle which could be accommodated on JOVE. It is therefore recommended that the measurements on the Jovian atmosphere not be undertaken with the mother-daughter technique. Such measurements should, however, be reconsidered if a nuclear upper stage becomes available, making possible two vehicles of the JOVE class in orbit about Jupiter. In this case, increased RF power availability and increased antenna gain could make the method quite attractive.

REFERENCES

1. A. Kliore; D. L. Cain and T. W. Hamilton: Determination of Some Physical Properties of the Atmosphere of Mars from Changes in the Doppler Signal of a Spacecraft on an Earth-Occultation Trajectory. JPL Tech. Rpt. 32-674, Oct. 15, 1964.
2. G. Fjeldbo and V. R. Eshleman: The Bistatic Radar Occultation Method for the Study of Planetary Atmospheres. J. Geophys. Res. 70, 3217-3225, July 1, 1965.
3. G. J. Fjeldbo; V. R. Eshleman; O. K. Garriott and F. L. Smith, III: The Two-Frequency Bistatic Radar-Occultation Method for the Study of Planetary Ionospheres. J. Geophys. Res. 70, 3701-3710, August 1, 1965.
4. B. A. Sodek: Jovian Occultation Experiment, submitted for publication. Brown Engineering Corp, Huntsville, Alabama.
5. J. V. Harrington, et al.: Electromagnetic Measurements of Planetary Atmospheres and Ionospheres by an Orbital Pair. Raytheon Rpt. FR-66-71, March 7, 1966.
6. Final Report. Project SPINMAP, School of Engineering, Stanford University, June 1966.

APPENDIX D

RTG ALTERNATE POWER SUPPLY SYSTEM



APPENDIX D

RTG ALTERNATE POWER SUPPLY SYSTEM

GENERAL DISCUSSION

Since the JOVE mission is well in the future, i. e. , the late 1970's or early 1980's, a long period of time is allowed for power technology to improve. The present designs of radioisotopic thermoelectric generators will undoubtedly be updated and, of course, larger systems will become readily available. With the advent of these greater magnitudes in power system outputs, more heat must also be rejected from the generator and, thus, present fin heat sinks will no longer be applicable. More heat must be rejected than fins are capable of handling, and an active coolant system must be applied to the system. This means that one must either pump a coolant, such as a liquid metal, through the system and let this coolant reject heat while it is away from the generator, or a heat pipe system must be devised. (A heat pipe is a closed system capable of transferring large quantities of thermal energy as latent heat of vapor between a source and a sink which exhibit only a small temperature difference [Ref. D-1].)

The reliability of a pump operating continuously for a three-year mission seems rather tenuous. Thus, heat pipes would be looked to as a means of solving the heat rejection problem. They seem to have excellent potential if development can continue to yield progress. Presently, one of the drawbacks was seen in the restriction of having the evaporator section at a level not much higher than the condenser section [Ref. D-2, D-3] and preferably much lower than the condenser section. This could present a tremendous problem, even in a 3-axis stabilized craft, since a simple rotation maneuver to lock on to a sensor reference item, such as Canopus, could mean that the mission might be a failure. This problem may not be as serious as has been stated here, but even if it is, a solution to it will hopefully soon be forthcoming.

An alternate power system to the one proposed in this report would then involve using two 320 W_e RTG's with heat pipes for cooling and for thermal control. Two RTG's would be used for redundancy but if one failed, it would be a serious problem to the overall mission capability. Of course, there would also be redundancy within the RTG itself so the possibility of one failing completely would be very small.

There is very little gain in specific power in going to an RTG system of this size [Ref. D-4] as compared to one of the $80 W_e$ size, which was considered the basic proposal for the JOVE mission. The size and weight of a larger $320 W_e$ dual power unit system leads to difficulty in the configuration of a spacecraft, since the two RTG's must be carefully placed with respect to the longitudinal axis and the center of gravity of the craft for stability considerations. This is more difficult with a larger, more massive object than with the smaller lighter $80 W_e$ RTG's. However, one of the difficulties involved with the placing of an $80 W_e$ RTG, i. e. , fin placement, is avoided since no fins would now be necessary. The heat rejection system for heat pipe cooled RTG's need not be close to the RTG unit. Of course, heat still must be dissipated to space.

One of the advantages of the larger RTG unit over the small unit, other than the obvious help in temperature control of the craft, is the fact that slightly less overall shielding is required. In the $320 W_e$ RTG system, the fuel is located only in two fuel capsules which, though they have four times as much fuel each, constitute an easier, more compact shielding problem than in small individual RTG units. This would cut down to some extent on the overall weight of the power system. At the same time it would allow the shield to be made of an ablative material with a very low thermal conductivity to aid in an abortive reentry of the RTG unit as an intact capsule. This is very important from both a political and nuclear safety standpoint.

Another advantage of a $320 W_e$ power system with active coolant would be that one would have much greater flexibility in arranging the fuel in the RTG with respect to the converter and shield sections. Several companies have probably looked into some of these possibilities, but it is difficult to determine their status since their reports on the subject are either confidential-restricted or classified. Several possibilities would include taking advantage of characteristics of an annular fuel capsule with converter units and heat sinks on both sides of it. Since this would be difficult to fabricate, small fuel capsule rods in an annular ring might serve the purpose. Several thin fuel plates could also be considered, though the use of a single fuel plate has been analyzed already.

SUMMARY

In summary, the use of two 320 Watt_e RTG's as a power supply system could have some very definite advantages for use on a space vehicle. Thermal control problems could be handled easily and much more efficiently than with a smaller power unit. There would be greater flexibility in overall RTG design. The shield could be entirely an ablative material, while the weight of units would be decreased in comparison to the weight of smaller RTG units generating the same amount of electrical power. No fins would be needed with such a system nor would the placement of the RTG's be as important as with the smaller finned units because of the absence of these fins.

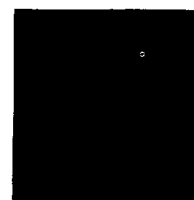
Offsetting these advantages for a 320 W_e RTG system are certain obvious disadvantages which hinder the concept. Pumping the coolant for a long duration mission is precarious from a reliability standpoint, while heat pipes seem to require that the evaporator section be placed at a lower level, and certainly at a level not much higher than the condenser section. The size and mass of a larger system would also lead to more difficult location problems. The most stringent problem, however, is simply that of properly developing the larger RTG unit.

Another possibility for the power system would be to use a heat pipe as a power flattening device with an isotope that has a shorter half-life than does Pu²³⁸. This would allow more readily available and less expensive fuels to be considered for the JOVE mission. As the heat is reduced because of a decrease in thermal output from the shorter-lived isotope, the hot length of the heat pipe is reduced, thus regulating power. Further increases in the efficiency of such a system could be realized from thermionic converters. This type of conversion has an inherently higher efficiency than does thermoelectric conversion, but it is not as well developed. Perhaps, by the late '70's it will be developed and could then be incorporated into the JOVE mission with either the 320 W_e or 80 W_e RTG units.

REFERENCES

1. Marcus, B. D.: On the Operation of Heat Pipes, 9895-6001-TU-000. Physical Electronics Laboratory, TRW Space Technology Laboratories, May 1965.
2. Deverall, J. E. and Kemme, J. E.: Satellite Heat Pipe, LA-3278-MS. Los Alamos Scientific Laboratory of the University of California, April 20, 1965.
3. Frank, S.; Smith, J. T. and Taylor, K. M.: Heat Pipe Design Manual, MND-3288. Martin Nuclear, February 1967.
4. Corliss, William, R. and Harvey, Douglas G.: Radioisotope Power Generation. Prentice-Hall, Inc., 1964.

APPENDIX E
ALTERNATE ANTENNA CONSIDERATIONS



APPENDIX E
ALTERNATE ANTENNA CONSIDERATIONS

DEFINITION OF SYMBOLS

β_x	Phase taper along x axis
β_y	Phase taper along y axis
β_z	Phase taper along z axis
λ	Wavelength
d	Element separation
θ_v	Vertical scan angle
θ_h	Horizontal scan angle

INTRODUCTION

Significant data rates from missions to the outer planets require that spacecraft transmitter power be increased or that the overall gain of the communication system be increased. Ground station antennas, in the neighborhood of 210- to 250-foot diameter, are nearing the practical limit for antenna aperture size; and the cryogenically-cooled traveling-wave masers, presently used in the ground station receivers, represent the ultimate in receiver sensitivity. Moderate increases in transmitter power may be expected through the use of multiple low-power traveling wave tubes or electrostatically focused klystron amplifiers. With increase in transmitter power, however, there is a corresponding increase in the power-supply requirements for the spacecraft.

Missions to the outer planets take the spacecraft into a region where the rapidly decreasing sunlight and low temperature combine to make the use of solar cells for electrical power impractical. The long mission lifetime rules out other power-supply sources except nuclear sources, such as the radio-isotopic thermoelectric generator or reactor power supplies. Present thermoelectric converters have a low efficiency resulting in high thermal (thermo-control problem) and high radiation levels which result in damage to semiconductor electronic components.

An obvious answer to the need for increased circuit gain is the use of larger spacecraft antenna gain. This introduces concomitant difficulties, however, with attitude control system. The antenna gain is proportional to the square of the aperture diameter in wavelength but the beam width is inversely proportional to the antenna diameter in wavelengths. If antenna pointing losses are to be avoided, precise control of the spacecraft attitude is required. As a rule of thumb, the pointing accuracy requirements for the attitude control system are roughly one-tenth of the antenna beam width, in order that the antenna pointing loss be kept to less than 1 dB. The attitude control systems are not normally implemented as proportional control systems, but they are of the on-off type and allow the spacecraft to wander through a dead-band region which constitutes a limit cycle.

Attitude control is obtained by means of orthogonal cold gas jets, and the cold gas reserve requirements depend upon the dead-band width. One method of relaxing the attitude control requirements, yet maintaining high pointing accuracy with no mechanical inertia effects, is the use of electronically scanned antennas. The next section discusses a brief survey of electronically scanned antennas with the view toward application to the JOVE vehicle.

ELECTRONICALLY SCANNED ANTENNAS

In an electronically scanned array each antenna element has an electromagnetic field that propagates through a relatively large angle, but when several elements are operated together their fields, which are vector quantities, cancel in certain directions and reinforce in other directions [Ref. E-1].

Phasing Requirements. The direction of principal reinforcement is the direction of maximum gain. The direction can be changed by changing the phase relationship between the elements. The direction of maximum radiation is such that each element of the antenna is electrically equidistant from the point of reception. Thus, if the separation between transmitting and receiving antennae is much greater than the dimensions of the antenna itself and if the antenna consists of a plane surface, the phasing requirement can be stated as follows:

"The rate of phase advance (known as phase taper) along any line across a plane aperture must be uniform."

A mathematical relationship between the direction of beam pointing and the phase tapers existing along orthogonal axes in the plane of the antenna array is needed. If x and y axes are chosen, as shown in Figure E-1, and the direction of beam pointing is measured as the angle formed between the beam direction and the two coordinate axes, β_x and β_y respectively, then in terms of β_x and β_y the phase tapers along the x and y axes are:

$$\cos \theta_x = \frac{\lambda \beta_x}{2\pi} \quad \text{and} \quad \cos \theta_y = \frac{\lambda \beta_y}{2\pi} \quad (1)$$

where λ is the wavelength in the same units as β .

Scan Volume and Gain. Two quantities which determine the sizing of an electronically scanned array are the scan volume and the gain. The maximum scan volume of an electronically scanned antenna is determined by the radiation pattern of the individual element, by the separation between elements to avoid multiple beams (known as grating lobes), and by excessive mutual coupling. The gain of an electronically scanned antenna is a function of the element spacing, the number of elements as well as the direction of beam pointing. A limitation which is placed upon the maximum element spacing to avoid grating lobes or multiple beams is

$$d_{\text{max.}} = \frac{1 - \frac{1}{N}}{1 + \sin \theta} \lambda \quad (2)$$

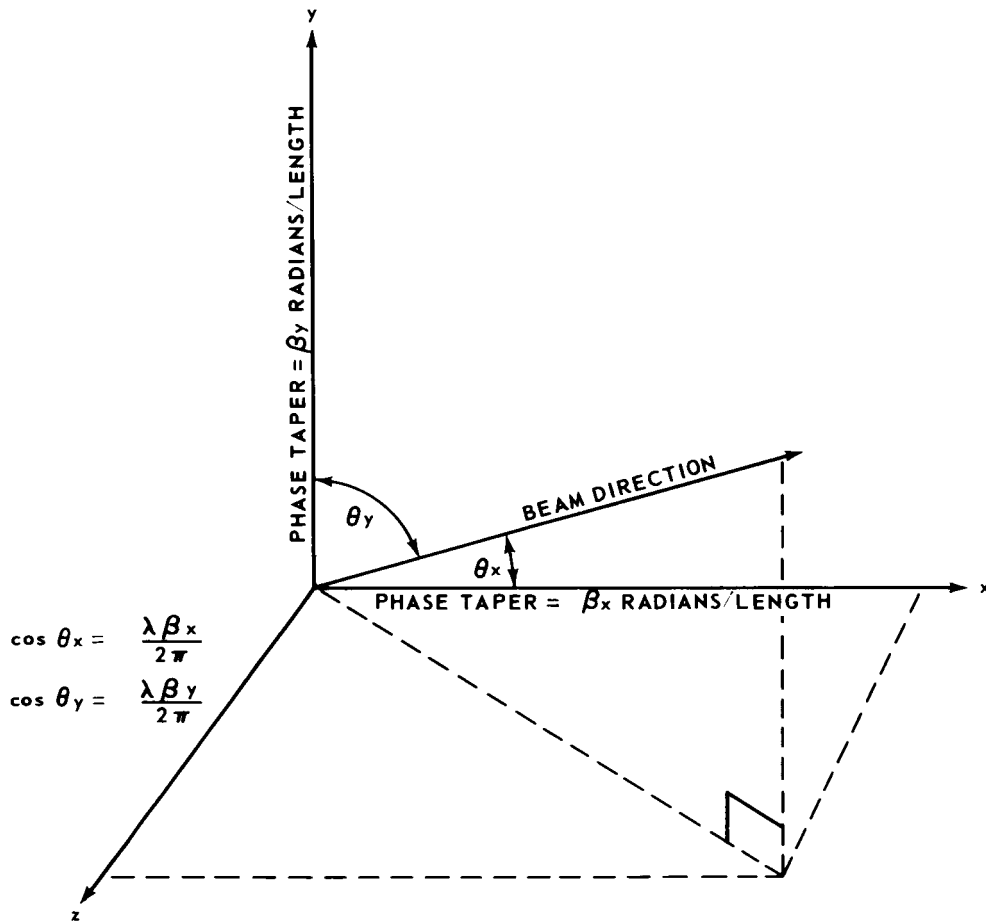


FIGURE E-1. COORDINATE SYSTEM

where d and λ are the element separation and wavelength respectively in the same units, n the effective number of rows or columns of elements evaluated as the equivalent numbers of rows or columns of elements for uniform excitation and equal beam width, and β is the maximum off-broadside scan angle.

For example, a large linear broadside array which does not scan has a maximum element spacing of λ . For a $\pm 90^\circ$ scan angle $d_{\max} = \frac{\lambda}{2}$. As another example, consider a two-dimensional array of antenna elements with the maximum diagonal dimension being 6.1 meters or 20 feet. The elements would form a square with sides of length 4.3 meters. If the scan angle is chosen as $\frac{\pi}{6}$ radians it can be shown that the maximum element spacing to avoid grating lobes is approximately 73 centimeters. The rectangular array then would require 7 rows and 7 columns of antenna elements; that is, a 49 element rectangular array.

The gain of an electronically scanned antenna is a function of the element spacing and the number of elements as well as the direction of beam pointing. Antenna gain increases with element spacing as long as no grating lobes are produced. Studies made by R. W. Bickmore [Ref. E-2] have shown that if the stated element spacing for grating lobe reduction is not exceeded, the effective aperture at broadside radiation is equal to the projection of the actual aperture upon a plane normal to the direction of radiation. In this case, the element gain is accounted for by extending the effective aperture area beyond the center lines of the outermost elements by a radius corresponding to the effective aperture area of the individual element. Mr. Bickmore furthermore shows that the projected area computation breaks down at a scan angle of approximately 80° . From hereon gain increases with scan angle until the value normally associated with end-fire gain is achieved. By limiting the off-broadside scan angle to $\pm 30^\circ$, we find that the gain will vary as the product $\cos \theta_v \cos \theta_h$

where θ_v is the vertical scan angle

and θ_h is the horizontal scan angle, measured with respect to the broadside beam axis. At the extreme beam angles the gain would be reduced by a factor of 0.75 for the antenna considered. The gain in the broadside beam position would be about 40 dB, with approximately a 3-dB reduction at the extreme angles: θ_v equals 30° , θ_h equals 30° .

Scanning Systems. There are three general types of electronically scanned antenna systems. These are:

1. Frequency Scanned Systems.
2. Phase Shifter Systems.
3. Beam Switching Systems.

7x7 Phase - Steered Array

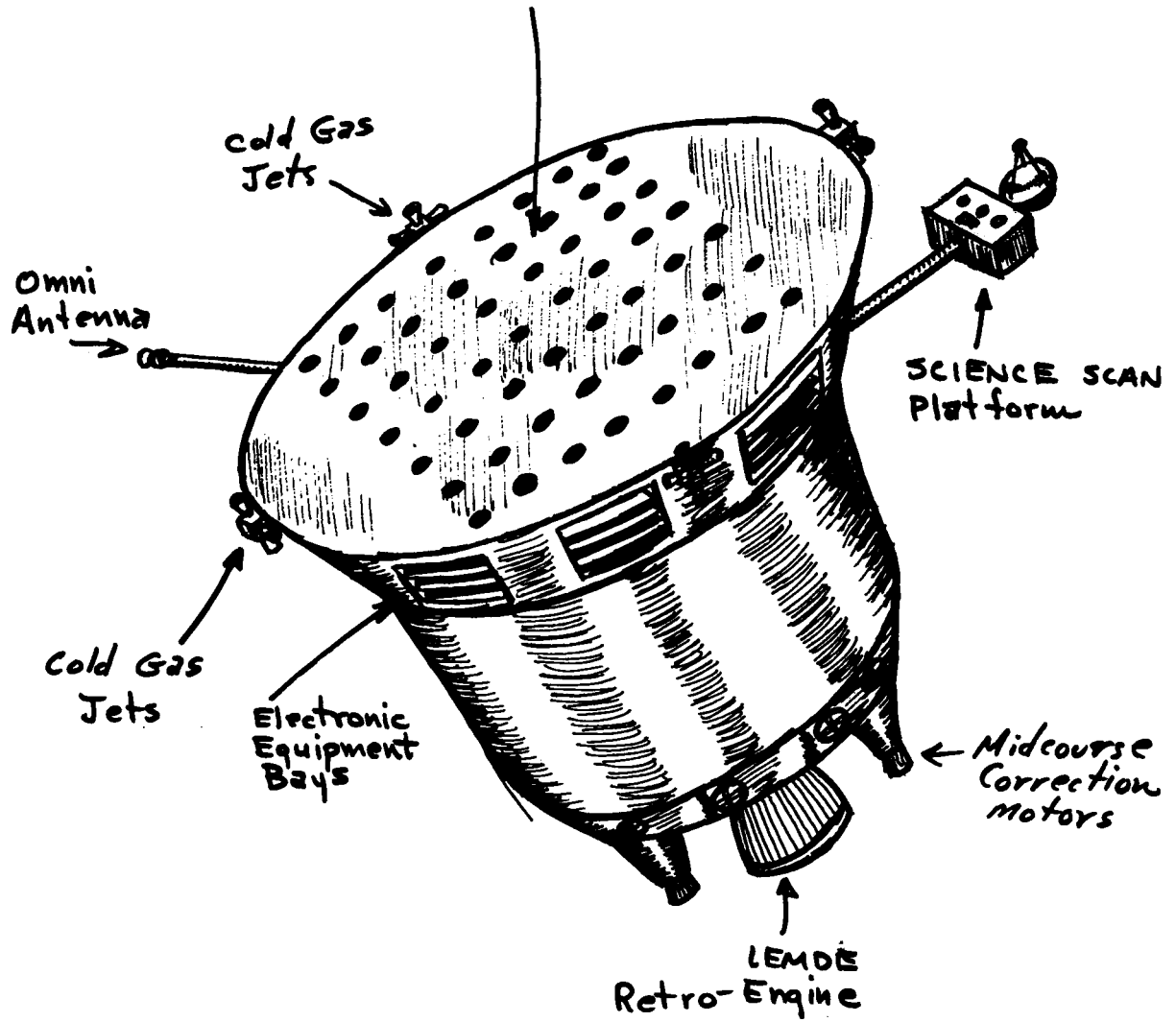


FIGURE E-2. JOVE PHASE STEERED ARRAY CONCEPT

The frequency scanned system represents the simplest mechanization and is the most compact since the antenna itself has no moving parts and no electronically circuit components. The frequency scanned system, however, requires a more complex transmitter and receiver which perform equally well over a broad-band of frequencies and which have provisions for accurate frequency control and readout. Although beam positioning with this system is extremely fast, as well as very accurate, the frequency scanned system would not appear to be compatible with the present DSIF Station since the VCO's in the phase locked loops of the station and spacecraft would be required to operate over a broad range of frequencies.

The phase shifter system is quite complex. It requires at least one phase shifter per radiating element. The phase shifters must be driven either mechanically or electrically from a central control point (usually a computer) to establish the required phase front for a collimated beam. This computer serves also as a beam position readout device as needed in direction finding. Phase tolerances of mechanical phase shifters are generally better than electronic phase shifters. For this reason, an all electronic antenna system can be expected to possess higher side lobes, loss in gain, and less beam positioning accuracy. The phase shifter antenna has the feature, an advantage in some applications, that the phase shift, and hence, the pointing angle of the beam, can be controlled over a continuous range.

The beam switching antenna is usually the largest of the three types of antennas considered. It is basically made up of a number of antennas pointed in different directions, but using the same aperture. In principle, a number of feeds, each corresponding to one beam direction, are connected to the same aperture in a manner that establishes the required aperture phase tapers. In addition, a multiport switch is essential for beam position selection unless a separate transmitter and/or receiver is provided for each of the beam positions. The advantages of this system are that the aperture phase accuracy is extremely good, it has low side lobes and high positioning accuracy. A disadvantage is that it does not scan uniformly, but step scans between predetermined positions as selected in design. This means, however, that the antenna pattern is more predictable than with a continuous phase shifter system.

Feed Systems. Of the three general types of electronically scanned arrays the frequency scanned antenna was rejected as incompatible with the DSIF. The phase shifter antenna and the beam switching antenna merited further consideration. The phase shifter antenna requires either a series or a parallel corporate feed to divide the power into correct amounts as dictated by the number of elements and the aperture illumination and is accomplished by means of

directional couplers or hybrids. The performance of the phase shifter antenna depends mainly upon the quality of the individual phase shifters employed and there are five major phase shifting techniques which meet the requirements for satisfactory operation of a phase shifter antenna. These are:

1. The mechanical phase shifter.
2. The ferrite phase shifter.
3. The semi-conductor phase shifter.
4. The frequency conversion phasing scheme.
5. The ferrite controlled radiating slot.

The mechanical phase shifter is effectively a line stretcher or variable delay line. A large number of mechanical phase shifters would be required. The notorious unreliability of mechanical systems plus the power limitation of a spacecraft would limit consideration of this technique.

The ferrite phase shifters make use of the variable rf permeability of ferrite materials to control the velocity of propagation and hence the time delay or phase shift in a length of wave guide. Ferrite phase shifters are plagued by temperature, frequency, and power level effects. The saturation magnetization of all ferrites is temperature sensitive and is known to vanish at a temperature termed the Curie temperature. Such Curie temperatures range from 80 to several hundred degrees centigrade, but significant temperature effects on the magnetization occur in the range to 35 to 80°C. The magnetic field for the ferrite phase shifter is maintained by means of a DC current through an external solenoid.

The semi-conductor phase shifter employs a number of silicon crystals or pn junction variable capacitance diodes, arranged to form an rf delay line or to terminate two ports of a hybrid junction. Bias voltages applied to silicon crystals effect their resistance. In the case of varactors the capacity is affected. In the hybrid circuit the diode impedance affects the phase of the reflection coefficient of branching lines. The diode phase shifter has somewhat higher loss than the values possible with ferrite phase shifters. In addition, crystals and their actors are not recommended for use at power levels in excess of several watts. The driving power required for semi-conductor phase shifters, however, is quite low.

A frequency conversion phasing scheme has been developed to use differential phase shifting at an intermediate frequency. This technique is useful primarily for either receiving or transmitting. Disadvantages are delicate phase balancing and phase stability requirements for the mixers, the dependence upon mixer crystals whose performance changes with age and the high cost of transmitting amplifiers. One transmitting amplifier is required for each radiation element.

Ferrite controlled radiating slots make use of wave guide radiating slots whose phase and amplitude are controlled electronically by means of ferrite discontinuities.

The discussion of beam switching antennas should be divided into two basic categories: the technique for establishing multiple antenna beams and the technique for switching between them. Multiple beams call for the establishment of multiple phase tapers as controlled by a number of input feed points. This can be accomplished by exciting a single antenna reflector or a single antenna lens with a number of primary feeds physically displaced so that collimation takes place in different space directions. Earlier attempts along this line made use of a parabolic reflector or lens, and a number of slightly defocused beams. The resulting increase in side lobe level thus limited the number of beams to something like a 4 by 4 cluster with adjacent beams crossing over at -3 dB. More recently a number of sophisticated schemes making use of the properties of certain geometric surfaces and inclined wire grids have appeared in the literature. Discrete scanning of a two dimensional array requires only incremental phase shifting which is possible with step digital diode phase shifters or with a matrix distribution system such as the Butler array. Recently a beam switching phased array satellite antenna has appeared in the literature [Ref. E-3]. This satellite antenna can be steered over 4π steradians, that is, the whole sphere. It has a measured beam width at 2200 MHz of 18° in elevation and 23° in azimuth. The measured gain is 13 dB and the package resembles a small oil drum 35 inches high and 18.7 inches in diameter. The antenna system itself forms part of the enclosing structure and the matrices and transmission lines are nearly all printed circuits. Therefore, most of the interior of the drum is open. The entire system weighs approximately 65 pounds.

DEPLOYABLE ANTENNAS

Another concept considered was the TRW Sunflower concept folding antenna [Ref. E-4]. This antenna has been designed, fabricated, and subjected to the

critical tests of deployment and vibration in a 32.2-foot diameter size. This high-gain antenna would open like a flower and could provide antenna gains which would not be limited by the shroud dimensions.

A JOVE spacecraft design based on the Sunflower concept for the primary high-gain antenna is shown in Figure E-3. This design concept was not pursued further when it was discovered that the 20-foot diameter resulted in adequate gain for the mission.

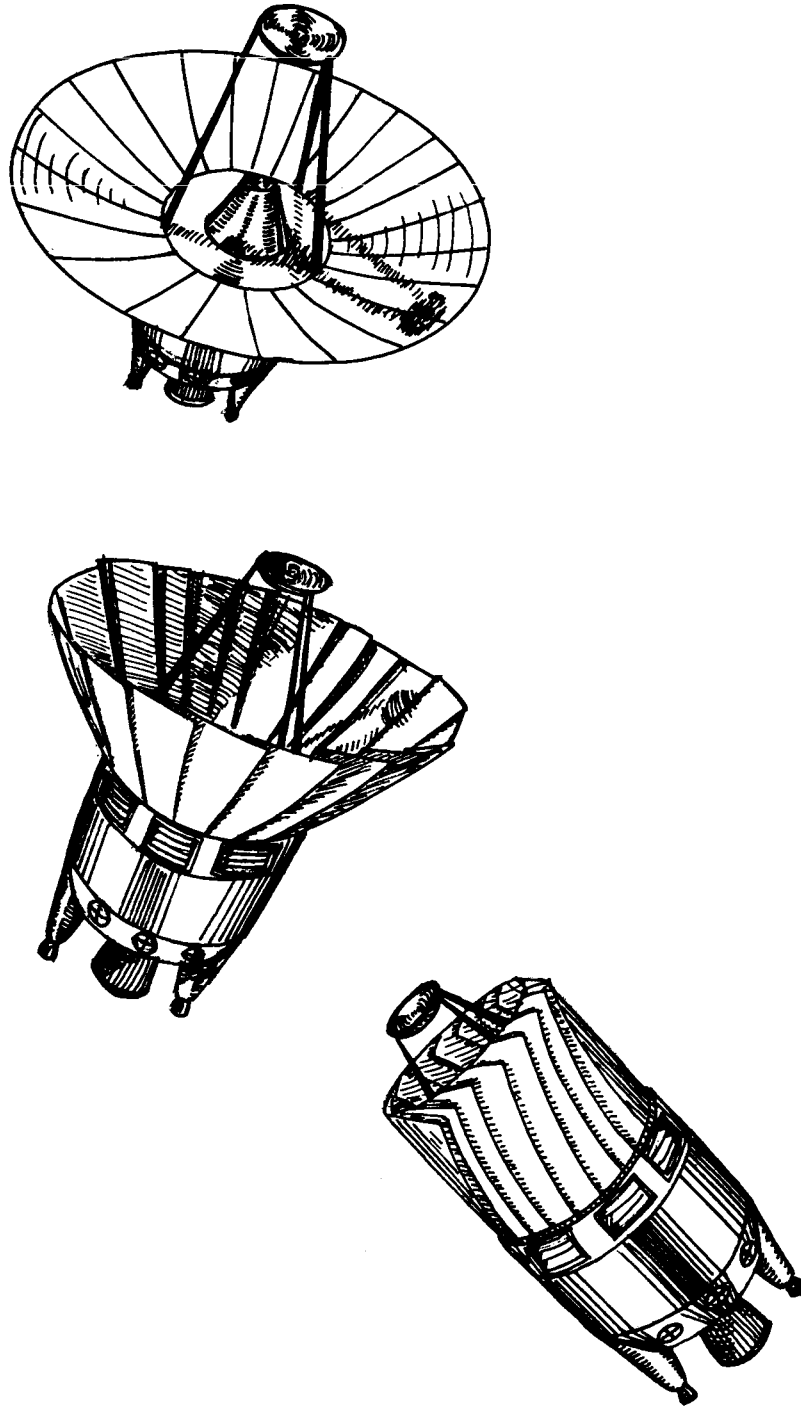


FIGURE E-3. JOVE DEPLOYABLE REFLECTOR CONCEPT

REFERENCES

1. Shnitkin, H.: Survey of Electronically Scanned Antennas. Microwave Journal, December 1960.
2. Bickmore, R. W.: A Note on the Effective Aperture of Electrically Scanned Arrays. Transactions IRE, vol. AP-6, April 1958, pp. 194-196.
3. Korvin, William and Chadwick, George G.: The Latest Word in Space Talk - It Can Come from Anywhere. Electronics, McGraw-Hill Book Company, May 30, 1966, pp. 117-126.
4. TRW Systems. Advanced Planetary Probe Study. Final Technical Report, vol. 4, JPL Contract 951311, July 27, 1966.

APPENDIX F
DETAILED STRUCTURE CALCULATIONS



Boost Loads

For main boost use 6g limit longitudinal

1g " lateral

1200^{l-k} torque

BOOST SUPPORT MEMBERS

Uniform boost, vertical component ea. leg:

$$20^k / 9 \times 6g \times 1/12 = 10^k$$

$$\text{Axial load} = 10^k / \sin 46.2^\circ = 12.1^k$$

Lateral Load

Distribution:

$$2 @ 0.00 P = 0.00 P$$

$$4 @ 0.50 P = 2.00 P$$

$$4 @ 0.86 P = 3.44 P$$

$$2 @ 1.00 P = \underline{2.00 P}$$

$$7.44 P$$

$$P = \frac{20^k}{7.44} = 2.69^k$$

Axial force, worst member, from horiz. force:

$$2.69^k / \cos 46.2^\circ = 3.69^k$$

Moment

$$20^{\text{kips}} \times 30'' = 600^{\text{k-''}}$$

Distributed same as horiz. load; axial load induced, worst member = $600^{\text{k-''}} / 7.44 \times 120'' \times \sin 46.2^\circ = \underline{\underline{0.93^k}}$

Adding, Max compression, worst member = 16.92^k

Boost Support Members (contd)

Using F.S. = 1.25 and assuming Euler Column;
aluminium strut:

$$I_{reqd} = \frac{P_{cr} L^2}{\pi^2 E} \times 1.25 = \frac{16.92 \times 72.4^2}{\pi^2 \times 10^4 \text{ ksi}} = 1.4 \text{ in}^4$$

Try I section, 3" x 1/4" flanges, 2" x 1/8" web.

$$I = 2 \times 0.75 \times (1.125)^2 + (0.125)(2)^3 / 12 = 1.90 + 0.99 = 1.99 \text{ in}^4$$

Use - Main Boost Supports

12 - I's ; 3" x 1/4" flanges, 2" x 1/8" web

Weight

$$1.75 \text{ ft}^3 \times 73 \text{ lb/ft}^3 \times 0.1 \text{ #/in}^3 \times 12 = 154 \text{ lbs Main Supports}$$

Antenna End Shell

Assume shell around main supports carries
torque, 12,000 in-k.

$$\text{Shear flow, at boost vehicle} = \frac{12000 \text{ in-k}}{\pi \times 240 \text{ in} \times 120 \text{ in}} = 0.133 \text{ k/in}$$

$$\text{Shear flow, at equipment boxes} \approx \frac{12,000 \text{ in-k}}{\pi \times 184 \text{ in} \times 92 \text{ in}} = 0.226 \text{ k/in}$$

Taking as simply supported plate, 37" x 60" and
F.S. = 1.25:

$$N_{cr} = 0.226 \times 1.25 = 0.283 \text{ k/in}$$

Antenna End Bus Ring

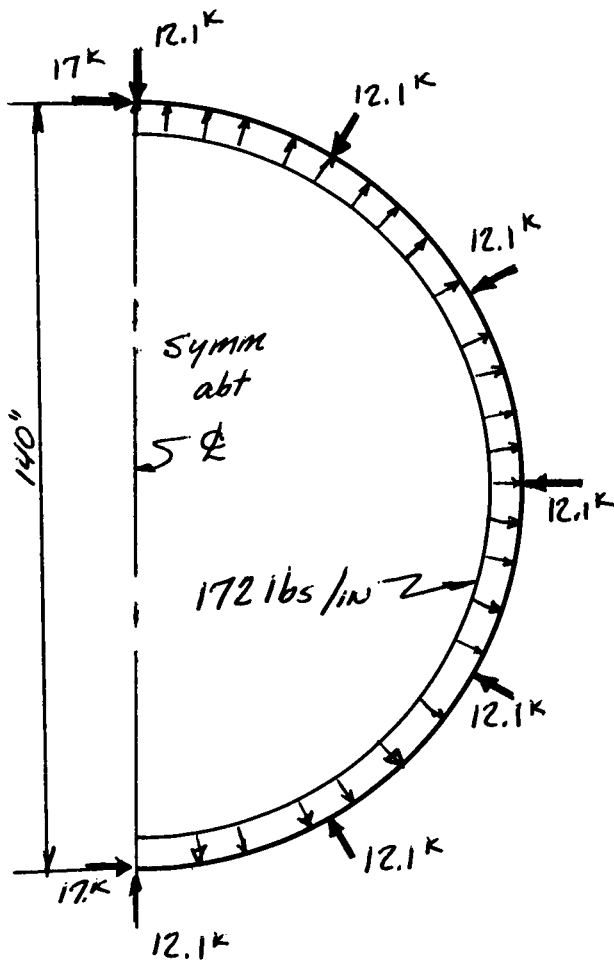
Loads

Since tank loads at boost act opposite to support structure loads and tend to compensate for lateral effects - take symmetrical boost, tank loads uniformly distributed.

From tanks:

$$\frac{14,286 \text{ lb}}{2} \times 6 \times \frac{1}{140\pi} = 97.5 \text{ lbs/in}$$

$$97.5 \times 1.25 \times 1 / \sin 45 = 172 \text{ lbs/in}$$



$$24.2^k (\sin 30 + \sin 60) = 33.1^k$$

$$24.2^k \sin 90 = \underline{-24.2}$$

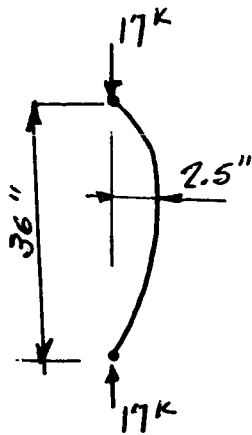
$$57.3$$

$$172^k / \text{in} \times 140'' = \underline{-24}$$

$$33.3^k$$

$$\frac{33.3^k}{2} \approx 17^k \text{ compression}$$

Taking one segment as Euler Column :



$$\text{Max Moment} = 47.5 \text{'' k}$$

$$\text{Try - } \left. \begin{array}{l} 3 \times \frac{1}{4} \text{ flanges} \\ 2 \times \frac{1}{4} \text{ web} \end{array} \right\} \begin{array}{l} \text{Area} = 2.00 \text{''}^2 \\ I \approx 2.07 \text{''}^4 \end{array}$$

$$P/A = 17/2 = 8.5 \text{ ksi}$$

$$M_c/I = 47.5 \times 1.125 / 2.07 = 25.8$$

$$\frac{P}{A} + \frac{M_c}{I} = 8.5 + 25.8 = 34.3 \text{ ksi}$$

$$\text{Check Euler Load, } P_u = \frac{\pi^2 EI}{L^2} = \frac{\pi^2 \times 10^7 \times 2.07}{36^2} = 160 \text{ k}$$

USE - Antenna End Ring

$3 \times \frac{1}{4}$ flanges ; $2 \times \frac{1}{4}$ web

Weight

$$200 \text{ in}^2 \times 0.1 \text{ #/in}^3 \times 138 \text{''} \times \pi = \boxed{86.5 \text{ lbs}}$$

Engine End Bus Ring

Obviously more lightly loaded than antenna end ring use same section.

Weight

$$\boxed{86.5 \text{ lbs}}$$

Bus Shell

Based on micrometeoroid requirements. Exposed lateral area:

$$140'' \times 60'' = 8.4 \times 10^3 \text{ in}^2$$

$$8.4 \times 10^3 \text{ in}^2 \times 6.45 \times 10^{-4} = 5.5 \text{ square meters.}$$

Assuming about 200 days in asteroid belt and worst case asteroid;

With 1000 m²-days about 1.4 cm \bar{t} reqd for maximum of 2 penetrations.

$$\bar{t} = \frac{t_1 + t_2}{k}. \text{ If spacing} = 2'', k = 0.2$$

$$t_1 + t_2 = (1.4)(0.2) = 0.28 \text{ cm} = 0.11 \text{ in.}$$

$$0.11/2 = 0.055'' \text{ say } \boxed{0.06'' \text{ each layer}}$$

check stress level -

$$q \text{ from boost } 19.5'' \times 6 \times 1/140 \pi = 0.266 \text{ K/in.}$$

$$q_{\text{max}} \text{ from moment } (19.5 \times 30'') / \pi (70)'' = \frac{0.040}{0.306 \text{ K/in.}}$$

$$\sigma_{\text{max}} = 2/t = \frac{0.306}{0.12} = 2.56 \text{ ksi}$$

Weights

$$\text{Aluminum } 0.06'' \times 140'' \times \pi \times 58'' \times 0.1 \text{ #/in}^3 \times 2 = 306$$

$$\text{Foam } 2.3 \text{ #/ft}^3 \times 0.166' \times \pi \times 11.65' \times 4.83 = 62$$

$$\text{Stiffeners } 0.01 \times 30 \times 60 \times 0.1 = \underline{2}$$

$$370 \text{ lbs}$$

Engine End Shells

Cone Frustrum (RTG Support)

Use - Double shell; 0.03" Al. faces, 1" spacing filled with foam.

Weight

$$(0.03" \times 44" \times 114 \times \pi \times 0.1) \times 2 = 94.5 \text{ \#}$$

Less RTG area:

$$8 \times 0.03 \times 0.1 \times 2 \times \pi \times 12^2 = \underline{21.8}$$

72.7 say

$$\begin{array}{r} 73 \\ \hline \end{array}$$

$$\text{Foam: } 0.083' \times 3.66' \times 9.5' \times \pi \times 2.3) \times \frac{72.7}{94.5} =$$

$$16 \text{ lbs}$$

Stiffeners

$$\underline{2}$$

$$\boxed{79 \text{ lbs}}$$

Engine Base

Use same as for cone frustrum.

Weight:

Aluminum:

$$0.03" \times 0.1 \text{ \#/in}^3 \times \pi (44^2 \times 15^2) \times 2 = 64.5 \text{ lbs}$$

Foam:

$$2.3 \text{ \#/ft}^3 \times 0.083' \times \pi (3.67^2 - 1.25^2) = \underline{7.1}$$

$$71.6$$

say

$$\boxed{72 \text{ lbs}}$$

Miscellaneous Weights

Equipment Boxes

Size of one box: 24" x 17" x 8.5"

$$2 \times (24 \times 17) = 8150"$$

$$2 \times (24 \times 8.5) = 4070"$$

$$2 \times (17 \times 8.5) = \underline{2890}"$$

$$15110" \times 0.05" \times 0.1 \text{ #/in}^3 = 7.555 \text{ lbs}$$

$$12 \times 7.555 = \boxed{90.5 \text{ lbs}} \quad \text{Attachment} - \boxed{10 \text{ lbs}}$$

Micrometeoroid & Heat Shield behind antenna:

$$\text{Aluminum: } 0.03" \times 0.1 \times \pi \times 120^2 = 130 \text{ lbs}$$

$$\text{Foam } 2.3 \text{ #/ft}^3 \times 0.04 \times 20^2 \times \pi = \underline{130}$$

$$\boxed{260 \text{ lbs}}$$

LEMDE FUEL TANKS

Based on 7460 lbs N_2O_4 ; Sp Gr = 1.37 \Rightarrow 87.3 ft³

3640 lbs 50/50 UDMH/ N_2H_4 ; Sp Gr = 0.8 \Rightarrow 72.8 ft³

If l = length of straight section req'd (4' ϕ spherical ends):

$$Vol = \frac{4}{3}\pi r^3 + \pi r^2 l$$

$$Vol = 32\pi/3 + 4\pi l$$

$$l = \frac{V - \frac{32\pi}{3}}{4\pi} = \frac{V - 33.3}{12.6}$$

for $V = \frac{87.3}{2} = 43.65$ ft³:

$$l = \frac{43.65 - 33.3}{12.6} = 0.82 \text{ 'say } 1'$$

Use 2-48" ϕ x 60" for N_2O_4

$$\text{Volume provided} = 2[33.3 + 12.6(1)] =$$

91.8 ft³ N_2O_4
7850 lbs Capy.

for $V = \frac{72.8}{2} = 36.4$ ft³:

$$l = \frac{36.4 - 33.3}{12.6} = \frac{3.1}{12.6} = 0.246' \text{ say } \frac{1}{2} \text{ ft.}$$

USE 2-48" ϕ x 54" for UDMH/ N_2H_4

$$\text{Volume provided} = 2[33.3 + 12.6(0.5)] =$$

79.2 ft³
3960 lbs
Capy.
UDMH/ N_2H_4

Lemde Fuel Tanks (cont'd)

Thicknesses

Assuming 6 Al-4V titanium; 120 000 psi ultimate; FS = 2; and working pressure = 240 psi.

$$t = Pr / \sigma_k = 240 \text{ psi} \times 24'' / 60,000 \text{ psi} = 0.096''$$

USE for LEMDE TANKS

0.1 in titanium

Weights

$$\begin{aligned} \text{one } N_2O_4 \text{ tank} &= 0.1 \times 0.16 \text{ #/in}^3 [12.57(24)^2 + 6.28(24)(12)] \\ &= 145 \text{ lbs} + 5\% \text{ fittings} \\ &= \boxed{153 \text{ lbs one } N_2O_4 \text{ Tank.}} \end{aligned}$$

$$\begin{aligned} \text{one } N_2H_4 / \text{UDMH Tank} &= 0.1 \times 0.16 [12.57(24)^2 + 6.28(24)(6)] \\ &= 131 \text{ lbs} + 5\% \text{ fittings} \\ &= \boxed{137 \text{ lbs one UDMH / } N_2H_4} \end{aligned}$$

LEMDE Tank weights (w/ fittings, w/o mounting):

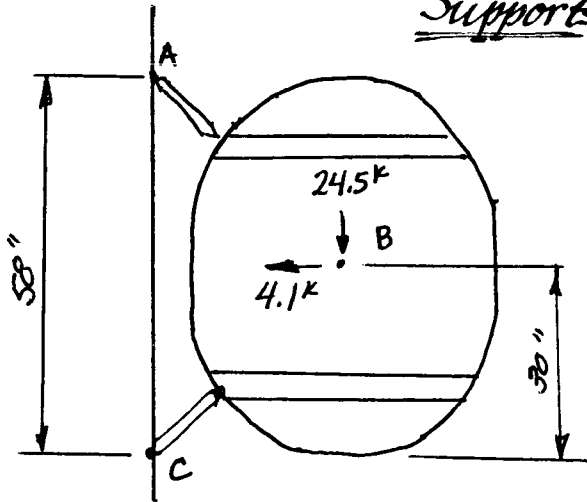
$$2 \times 153 = 306$$

$$2 \times 137 = 274$$

$$\boxed{580 \text{ lbs}}$$

Lemde Fuel Tanks (cont'd)

Supports



$$N_2O_4 = 3925 \text{ lbs}$$

$$\text{Tank} = \frac{153}{}$$

$$4078$$

$$\times 6$$

$$24,468 \text{ lbs.}$$

From 24.5^k

$$\underline{\Sigma M_A = 0}$$

$$58 C_h = 30 (24.5^k)$$

$$C_h = 12.65^k$$

$$F_c = \frac{1}{2} \times \frac{48.8}{30} \times 12.65 = 10.3^k$$

From 4.1^k

$$\underline{\Sigma M_A = 0}$$

$$4.1^k \times 30 = 60 C_h$$

$$C_h = 2.1$$

$$F_c = \frac{1}{2} \cdot 2.1 \times \frac{48.8}{30} = 1.63^k$$

$$\text{Maximum Compression} = 10.3 + 1.63 = 11.93^k$$

Try: $\left. \begin{array}{l} 3/4" \phi \\ t = 1/8" \end{array} \right\} 7075-T6 \text{ Al.}$

$$\text{Area} = \pi (0.375^2 - 0.25^2) = 0.245 \text{ in}^2$$

$$I = \pi t r^3 = (3.14)(0.125)(0.35)^3 = 0.055 \text{ in}^4$$

Lemde Fuel Tanks (contd).

Supports (contd.)

$$P_{cr} = \frac{\pi^2 EI}{L^2} = \frac{\pi^2 \times 1.04 \times 5.5 \times 10^{-2}}{4 \times 10^2}$$

$$P_{cr} = 13,300 \text{ lbs} \quad \text{OK} //$$

USE - LEMDE Fuel tank supports

4 - 3/4" ϕ , t = 1/8" each tank

Weights

per tank:

$$4 \times 0.245 \text{ m}^2 \times 20" \times 0.1 \text{ lbs/in}^3 = 1.95 \text{ lbs}$$

$$\text{Straps } 2 \times 0.063" \times 3" \times \pi \times 20" \times 0.1 \text{ lbs/in}^3 = 2.38$$

$$4.33 \text{ lbs say } \boxed{4.5 \text{ lbs}}$$

Weight LEMDE tank supports: 20 lbs

Secondary Propulsion Tanks

Based on 150 m/sec. midcse correction & 100 m/sec orbit trim; monopropellant reqd: 1400 lbs
22.4 ft³

Max radius = 1'

for two tanks,

$$t = \frac{pr}{\sigma_h} = \frac{240 \times 12}{6 \times 10^4} = 0.048$$

$$11.2 = \frac{4}{3}\pi(1)^3 + \pi(1)^2 l$$

$$\boxed{\text{Use } t = 0.05''}$$

$$11.2 = 4.19 + 3.14 l$$

$$l = 2.23' \rightarrow 2'-3''$$

USE - Monopropellant tanks -

2 - 24" ϕ x 51" tanks

Weight one tank: $0.05'' \times 0.16 \text{ #/in}^3 [4\pi r^3 + 2\pi r h]$

$$: 30.8 \text{ lbs} + 10\% = 34 \text{ lbs.}$$

one tank: 34 lbs

both tanks 68 lbs

Volume provided:

$$2(4.19 + \pi(1)^2(2.25)) = 2(11.26) =$$

$$22.52 \text{ ft}^3$$

1405 lbs

Cap

Mono-
prop

Attitude Control Tanks

Assuming $7.2 \text{ ft}^3 \text{ N}_2$ reqd.

Two Spheres

$$\text{Vol} = \frac{4\pi}{3} r^3$$

$$3.6 = \frac{4\pi}{3} r^3$$

$$r^3 = 0.86'$$

$$r = 0.95' \text{ say } 1 \text{ ft}$$

Thickness

$$t = \frac{pr}{\sigma} = \frac{3500 \times 12}{60,000} = 0.33 \text{ say } \boxed{0.35''}$$

Weight

one tank:

$$0.16 \times \frac{4\pi}{3} [12^3 - 11.65^3] = 97.8$$

say

98 lbs

Weight both tanks:

$$\boxed{196 \text{ lbs}}$$

Pressurant Tanks

<u>Volume</u>	N_2O_4	91.8 ft ³
	UDMH/ N_2H_4	79.2
	Monopropellant	<u>22.5</u>
		193.5 ft ³

At storage pressure these volumes reduce to

$$19.05 + 6.06 = \underline{25.11} \text{ ft}^3 \quad (\text{Ref VI.3.C. \& D. this report})$$

or 12.55 ft³ per tank

If radius = 1.0 ft then

$$12.55 = \frac{4}{3} \pi (1)^3 + \pi (1)^2 l \Rightarrow l = 2.67 \text{ ft (32")}$$

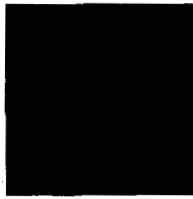
2 Tanks are provided 12" ϕ x 56" for He₂

$$\underline{\text{Thickness}}: T = \frac{Pr}{\sigma} = \frac{3500 \times 12}{60,000} = \underline{0.66"} \text{ "$$

$$\underline{\text{Weight}}: \text{ For one tank} = .66 \times .16 [4\pi \times 12^2 + 2\pi \times 12 \times 32] \\ = 447 \text{ lbs.}$$

and for both tanks wt = 894 lbs.

$$\underline{\text{He}_2 \text{ required}}: \frac{3500 \times 144 \times 25.11 \times 4}{530 \times 1543} = \underline{61.5} \text{ lbs. He}_2$$



APPENDIX G

ON-BOARD NAVIGATION AND GUIDANCE SYSTEM

APPENDIX G

ON-BOARD NAVIGATION AND GUIDANCE SYSTEM

DEFINITION OF SYMBOLS

\underline{r}	Spacecraft position vector
\underline{v}	Spacecraft velocity vector
\underline{a}_T	Thrust acceleration vector
\underline{g}	Gravity vector
\underline{V}_r	Required velocity vector
$\left. \begin{array}{l} O_s \\ 4_s \end{array} \right\}$	Sun sensor gimbal angles
d	Diameter of Sun
β	Half of the seen angular dimension as measured from spacecraft
i_x, i_y, i_z	Inertial reference frame
V_x, V_y, V_z	Vehicular reference frame
$\overline{\alpha^2}$	Mean-squared a priori estimation error
E	Error correlation matrix
W	Error transition matrix
W^t	Transpose of error transition matrix

DEFINITION OF SYMBOLS (Concluded)

\underline{b}	Measurement geometry vector
\underline{z}	A vector formed by postmultiplying W^t by \underline{b}
$\underline{\Delta V}$	Velocity-to-be-gained
\underline{w}	Weighting vector
\underline{x}	Vector cross product
t_n	At the nth sampling instant

INTRODUCTION

The guidance system is often referred to as the brain of a space vehicle; its function is to provide steering commands for required changes in course. In order to achieve this objective, it must perform the navigation function of determining as accurately as possible the spacecraft position and velocity in order to predict the state at some future time. Mathematical operations performed on the estimated vehicle position and velocity then lead to the determination of a desired maneuver as well as the control of the correction maneuver itself.

Consider the basic computation in the navigation loop of the inertial guidance system shown in Figure G-1. Outputs from inertially stabilized integrating accelerometers, together with components of gravitational acceleration computed as a function of inertial position are summed and integrated to give the components of the velocity components. The ultimate precision is limited by the accuracy of the inertial instruments, the speed of the guidance computer, and the knowledge of the initial conditions. Initial alignment errors and measurement errors are unavoidable. Both the inertial measurement errors and the errors in the initial conditions give rise to position errors which enter the gravity computer giving rise to gravity errors which in turn are fed back into the system. An error analysis shows that the errors in the navigation loop have both oscillatory and divergent components [Ref. G-1]. These errors can be damped by the use of damping circuits and motional or positional information obtained with auxiliary measurements. They may include:

1. Position - measuring stellar trackers
2. Velocity - measuring doppler and
3. Positive information of a reference trajectory.

It is evident that spacecraft navigation during prolonged coasting flight involves a good deal of data processing. The current trend is to apply the statistical methods of optimum linear estimation theory or optimum filter theory to find a linear estimator that minimizes some function of the variance and covariances of the uncertainties in the estimated state vector [Ref. G-2]. In the navigation of deep space vehicles such as in the Jupiter mission, the statistics may be at best only partially known, a self-optimizing filter [Ref. G-3] which adapts itself with respect to the environmental statistics, would be of great

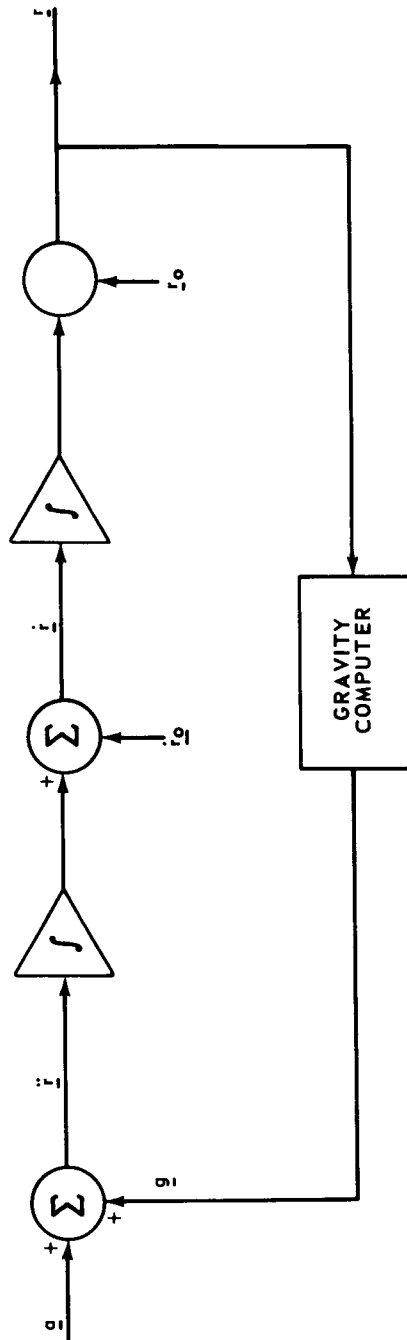


FIGURE G-1. THE BASIC NAVIGATION LOOP IN THE INERTIAL FRAME

advantage. Recent advances in the state-of-the-art of mechanization techniques, particularly on-board digital computers, have reached the point where practical implementation of this system configuration is possible.

A short description of the so-called "Recursive Method" [Ref. G-4] of spacecraft position and velocity estimation, which is under active consideration for use in the Integrated Mission Control Center, together with the "Velocity-to-be-Gained" method of guidance, is given in the following sections. This is compatible with the Adaptive Guidance Mode [Ref. G-5] developed at Marshall Space Flight Center for the Saturn Booster.

SATURN ASCENDING PHASE GUIDANCE

During the accelerated maneuver, a guidance computer is required to perform accurate integrations and gravity calculations in a real-time basis. In the Saturn Guidance Computer [Ref. G-6] the guidance and cut-off equations are empirically determined polynomial functions and the components of gravitational acceleration are approximated by a polynomial function of position components. The computation is repeated every one half second throughout the entire ascent phase in order to attain the accuracy compatible with desired Saturn performance.

A functional diagram for the Saturn guidance system is shown in Figure G-2. The vector values of velocity and position, the scalar magnitude of thrust acceleration and time are updated continuously by differentiating the outputs of the integrating accelerometers and taking the square root of the sum of the squares of the resulting derivatives approximately every second. The main difficulty with the adaptive guidance mode is to determine the best method of representing the volume of expected trajectories which yield minimum fuel consumption.

CELESTIAL-INERTIAL GUIDANCE

Over long flight times, the accumulated errors in the inertial guidance system may be overcome by a continuous series of fixes on celestial bodies and auxiliary observations made with on-board sensors. The navigation computer calculates an extrapolated estimate of the spacecraft position and velocity at the time a measurement is made. From this estimate, it is possible to predict the measured value of a quantity such as an angle, and the difference between the predicted and actual measured values is then used to improve the estimated position and velocity vector.

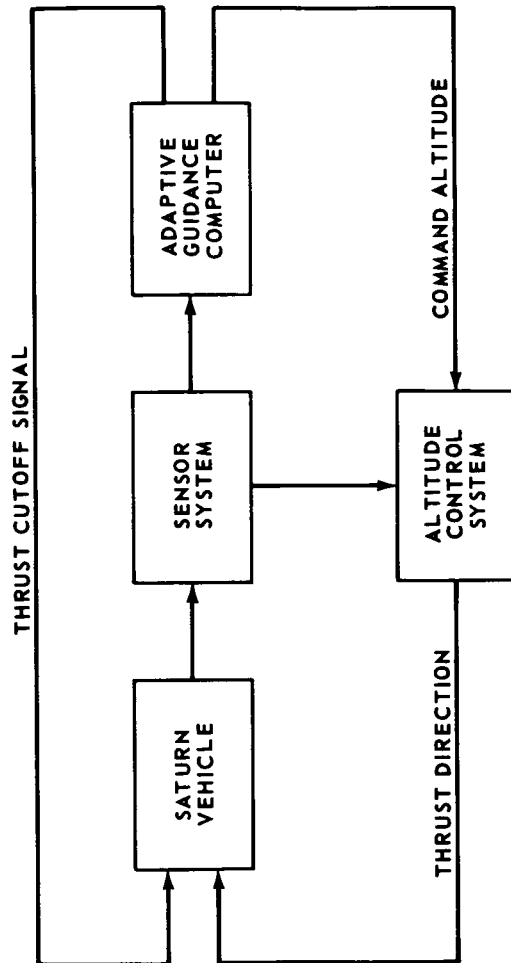


FIGURE G-2. ADAPTIVE SATURN GUIDANCE SYSTEM

Determination of Spacecraft Position using Sun Sensor. The position of a space vehicle in the interplanetary space can be determined from a sufficient number of on-board celestial observations [Ref. G-7], provided that the size, the orbit, and the motion of the planets are known and that at least one planet is observed each time. An accurate clock may be required for reading the sidereal time. For example, the sun sensor measures the angular dimension of the sun and its direction with respect to the vehicular frame. When the space vehicle is moving along a path around the sun, the origin of an inertial frame is heliocentric and its XYZ axes are fixed with respect to the fixed stars. A vehicular frame is rigidly fixed to the vehicle and follows its motion.

If d is the diameter of the sun and 2β is its angular dimension as measured from the vehicle (Fig. G-3), then the distance of the vehicle from the sun is

$$r = \frac{\frac{d}{2}}{\sin^2 \beta} \quad . \quad (1)$$

The direction of the sun with respect to the vehicle is readily determined from a knowledge of the gimbal angles θ_s and ψ_s . In terms of the vehicular frame the components of the position vector of the vehicle are

$$\begin{aligned} \text{X - component:} & \quad -r \cos \theta_s \cos \psi_s \\ \text{Y - component:} & \quad -r \sin \theta_s \cos \psi_s \\ \text{Z - component:} & \quad -r \sin \psi_s \quad . \end{aligned}$$

Now the components of the position vector in the inertial frame can be obtained by using the direction cosine matrix which establishes the relative orientation of the vehicular and inertial frames.

Recursive Navigation Computation. The essential feature of the recursive navigation operation is to combine the current best estimate with newly acquired information to produce a new and better estimate. Let the extrapolated estimate of the spacecraft position and velocity through integration of accelerometers be \underline{r} and \underline{v} . From this estimate, it is possible to make an estimate of a quantity to be measured such as an angle. The variation in the measured quantity resulting from variations in components of \underline{r} and \underline{v} is represented by a six dimensional vector \underline{b} . It depends on the geometrical configuration of the relevant celestial objects at the time t as well as on the particular type of measurement made. It is possible to combine algebraically the

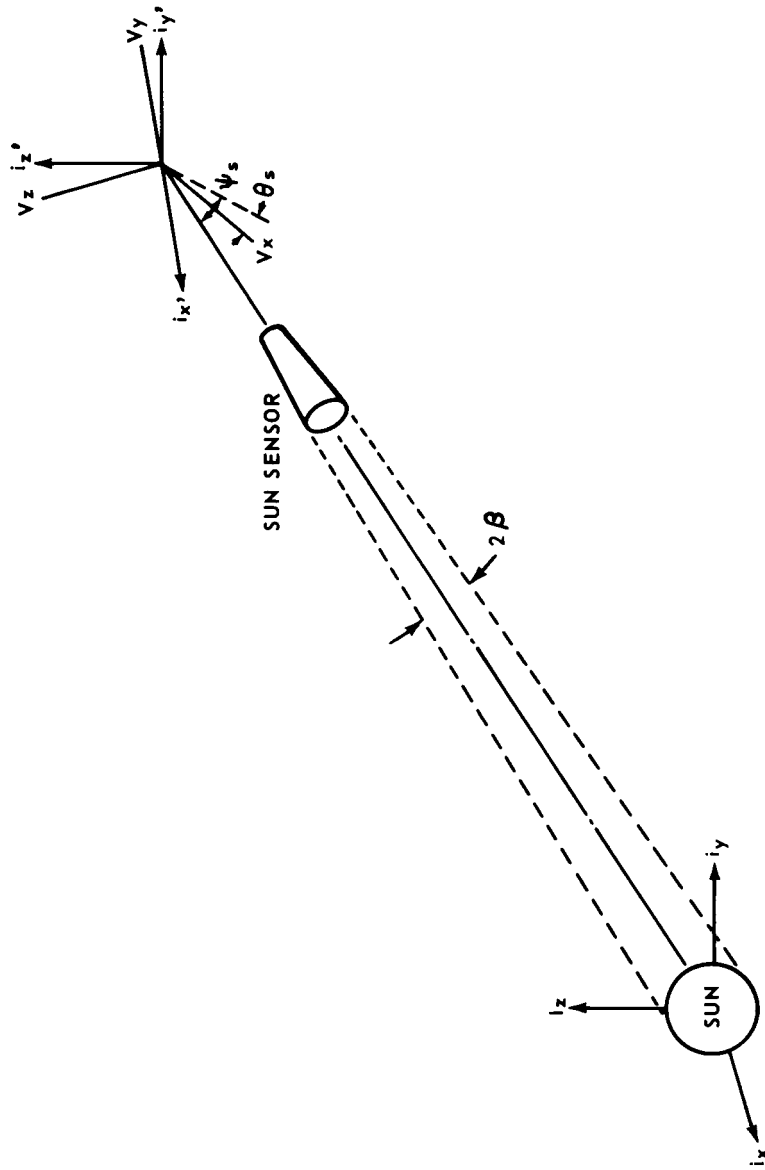


FIGURE G-3. DETERMINATION OF VEHICLE POSITION USING GIMBALED SUN SENSOR

vector \underline{b} , the error transition matrix W and a mean-squared a priori estimation error α^2 in the measurement to produce a required weighting vector W and the step change in error transition matrix δW to indicate changes in the uncertainties of the estimated quantities due to measurement.

The error transition matrix W is defined as a square root of the six-dimensional correlation matrix of estimation errors E , that is

$$E = W W^t \quad (2)$$

where t denoted taking the transpose operation. W satisfies the following differential equation

$$\frac{dW}{dt} = \begin{bmatrix} 0 & I \\ G & 0 \end{bmatrix} W \quad (3)$$

In the above, I is the three-dimensional identity matrix, 0 a three-dimensional null matrix and G a three-dimensional gravity gradient matrix. G is computed from a knowledge of estimated position information, that is,

$$G = \begin{bmatrix} \frac{\partial g}{\partial r} \end{bmatrix} \quad (4)$$

The introduction of the error transition matrix is to guarantee the correlation matrix to be at least positive definite. To avoid the difficulty caused by numerical inaccuracies, the correlation matrix may not remain positive definite after long computations.

The weighting vector W is computed from

$$W = \frac{W \underline{z}}{z^2 + \alpha^2} \quad (5)$$

where \underline{z} is defined as $\underline{z} = W^t \underline{b}$.

The step change in error transition matrix is given by

$$\delta W = \frac{W \underline{z}^t}{1 + \sqrt{\alpha^2 / (z^2 + \alpha^2)}} \quad (6)$$

Finally, where the predicted value of the quantity to be measured such as an angle is compared with the actual measured quantity, the difference is combined with the weighting vector to improve the estimated position and velocity vectors. A block diagram outlining the above computation procedure is shown in Figure G-4.

Consider the terminal navigation phase in project JOVE. Orbit determination and DSIF radio tracking help to determine the spacecraft position and velocity in the heliocentric space. The position of the spacecraft from Jupiter can then be estimated from a knowledge of Jupiter's location with respect to Earth and the tracking information. The planetocentric uncertainties in the position and velocity of the spacecraft are due to tracking errors and errors in Jupiter's ephemeris. These uncertainties can be reduced by direct observations of Jupiter from the spacecraft and with the on-board recursive navigation and guidance computations based on these observations.

Velocity-to-be-gained Method of Guidance. Let \underline{v} be the present spacecraft velocity and \underline{V}_r be the required instantaneous velocity corresponding to the present spacecraft location \underline{r} . The vector difference ΔV between \underline{V}_r and \underline{V} is the instantaneous velocity-to-be-gained, that is

$$\Delta \underline{V} = \underline{V}_r - \underline{V} \quad (7)$$

since

$$\frac{d\underline{V}}{dt} = \underline{g} + \underline{a}_T \quad (8)$$

where \underline{g} is gravity and \underline{a}_T is the thrust acceleration vector, the rate of change of $\Delta \underline{V}$ can be expressed as

$$\frac{d}{dt} (\Delta \underline{V}) = \frac{d\underline{V}_r}{dt} - \underline{g} - \underline{a}_T \quad (9)$$

A simple guidance logic is based on the recognition that all three components of $\Delta \underline{V}$ can be simultaneously driven to zero by aligning the time rate of change of the $\Delta \underline{V}$ vector with the vector itself. Clearly, a direction of \underline{a}_T can be chosen such that the cross produce

$$\Delta \underline{V} \times \frac{d(\Delta \underline{V})}{dt} = 0 \quad (10)$$

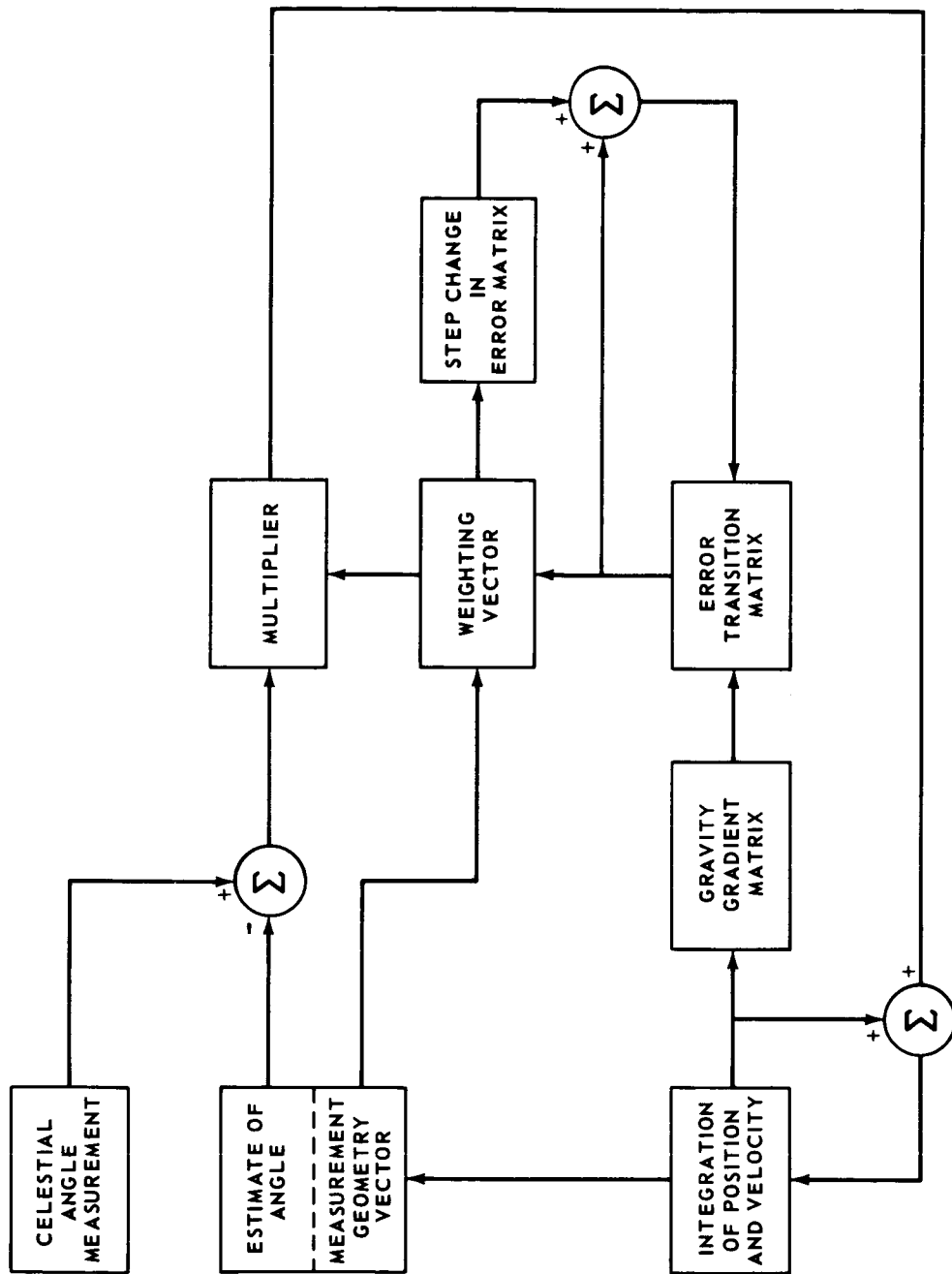


FIGURE G-4. RECURSIVE NAVIGATION COMPUTATION

\underline{v} , \underline{r} and \underline{g} are calculated from the outputs of accelerometers by the navigation computer previously described. \underline{v}_r is calculated from a knowledge of \underline{r} and a given set of mission objectives. Using values stored in previous sample time, the quantity

$$\underline{v}_r(t_n) - \underline{v}_r(t_{n-1}) - \underline{g} \Delta t$$

is easily obtained. Similarly, the integration accelerometer output is combined with the previously stored value to yield the quantity

$$\underline{v}_a(t_n) - \underline{v}_a(t_{n-1})$$

The error signal to direct the thrust vector \underline{a}_T to cause the vector $\frac{\Delta \underline{v}}{\Delta t}$ to be parallel to $\Delta \underline{v}$ and oppositely directed is the cross product

$$\Delta \underline{v} \times \underline{v}_r(t_n) - \underline{v}_r(t_{n-1}) - \underline{g} \Delta t - (\underline{v}_a(t_n) - \underline{v}_a(t_{n-1})).$$

When properly scaled, the cross product is a vector rate of command whose magnitude is proportional to the small angular displacement between the actual and the commanded thrust vectors and whose direction is simply the direction of the rotation of the spacecraft to cancel the error. The cross product guidance is terminated toward the end of the maneuver when $\Delta \underline{v}$ is small, and the engine cut-off is actuated on the basis of the magnitude of $\Delta \underline{v}$ while the spacecraft maintains a constant altitude. Figure G-5 shows a schematic diagram of cross product steering.

CONCLUDING REMARKS

In the serious planning of future ambitious programs of space exploration including the JOVE mission, it must be recognized that there are uncertainties in solar radiation pressure, solar plasma, meteoroid flux, the astronomical units, etc. The navigation and guidance requirements become increasingly severe if the payloads are of high degree of sophistication. Battin [Ref. G-4], director of space guidance analysis division of Apollo spacecraft, stated, "Navigation measurements are more accurately made by instrumentation carried aboard the spacecraft when the vehicle is far from Earth and in the vicinity of another planet. Furthermore, interplanetary distances tend to preclude primary reliance on communication with Earth for processing basic navigation data and providing guidance commands. The data-processing requirement must then be met by digital computation performed by a vehicle-borne computer. Therefore, the spacecraft of the future will operate with completely self-contained navigation and guidance systems."

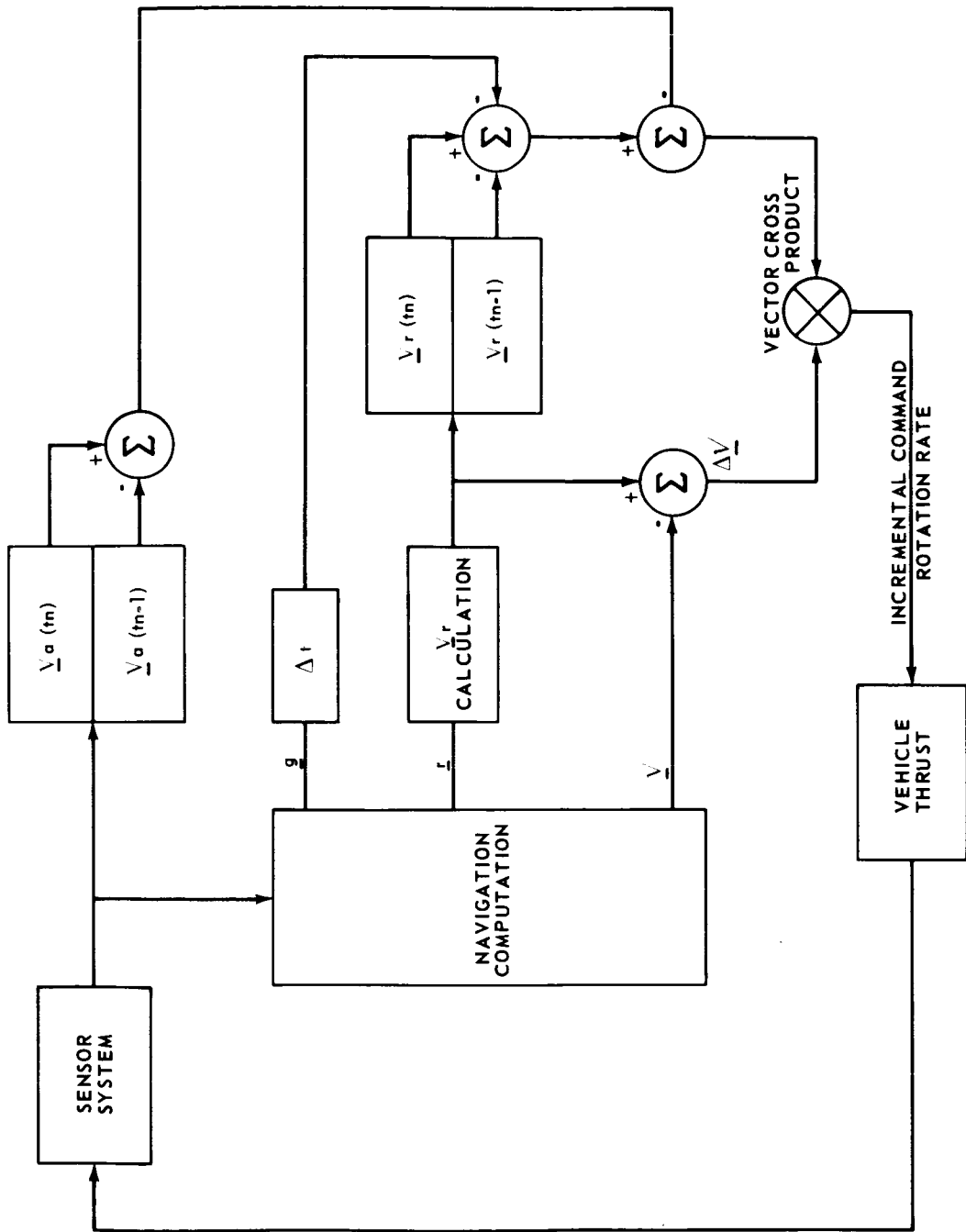


FIGURE G-5. ERROR SIGNAL FOR $\Delta \underline{v}$ STEERING

REFERENCES

1. Grammatikos, A.: Gimballess Inertial Systems for Space Navigation. NASA-CR-71089, 1966.
2. Potter, James E. and Stern, Robert G.: Statistical Filtering of Space Navigation Measurements. Progress in Astronautics and Aeronautics, vol. 13, pp. 775-801, Academic Press, New York, 1964.
3. Rome, H. James and Shen, D. W. C.: A Multi-input Self-Optimizing Filter with Applications to Hybrid Navigation Systems. Proceedings of 19th Annual National Aerospace Electronics Conference, May 1967, pp. 451-459.
4. Battin, Richard H.: Astronautical Guidance. McGraw-Hill Book Company, Inc., New York, 1964.
5. Chandler, Doris C. and Smith, Isaac E.: Development of the Iterative Guidance Mode with its Application to Various Vehicles and Missions. Journal of Spacecraft and Rockets, vol. 4, no. 7, July 1967, pp. 898-903.
6. Moore, F. Brooks and Brooks, Melvin: Saturn Ascending Phase Guidance and Control Techniques. Progress in Astronautics and Aeronautics, vol. 10, Academic Press, New York, 1963, pp. 183-209.
7. Cohen, D. F.: Hybrid Celestial Tracker. Proceedings 11th Annual East Coast Conference on Aerospace and Navigation Electronics, October 1964.



APPENDIX H

LEMDE EXHAUST JET EFFECTS

APPENDIX H

LEMDE EXHAUST JET EFFECTS

DEFINITION OF SYMBOLS

A_e	Exit area (ft ²)
c_p	Constant pressure specific heat ($\frac{\text{Btu}}{\text{lb}_m \text{ } ^\circ \text{F}}$)
g_c	Universal acceleration of gravity $\frac{\text{ft-lb}_m}{\text{lb}_f \text{Sec}^2}$
k	Ratio of specific heats (dimensionless)
M_e	Exit mach number (dimensionless)
M^*	Critical mach number (dimensionless)
\bar{M}	Mean molecular heat
m	Mass (lb _m)
p_e	Exit pressure (lb _p /in ²)
p_o	Combustion chamber pressure (lb _f /in ²)
R	Gas constant ($\frac{\text{lb}_f \text{ ft}}{\text{lb}_m \text{ } ^\circ \text{R}}$)
T_e	Exit temperature (°R)
T_o	Combustion chamber temperature (°R)
t	Time (seconds)
V_e	Exit velocity (ft/sec)

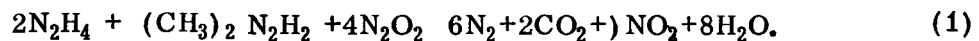
DEFINITION OF SYMBOLS (Concluded)

w	Weight flow rate (lb_m/sec)
ϵ	Emissivity (dimensionless)
τ	Thrust (lb_f)
$\omega (M^*)$	Simple wave flow function (dimensionless)

In order to estimate the angle of the jet exhaust issuing from the LEM engine the following engine performance characteristics are assumed:

Exit Velocity	$V_e = 9660 \text{ ft/sec}$
Exit Temperature	$T_e = 3460^\circ \text{ R}$
Weight Flow Rate	$w = 35 \text{ lb}_m/\text{sec}$
Exit Area	$A_e = 19.1 \text{ ft}^2$
Exit Pressure	$P_e = 4.15 \text{ lb}_f/\text{in}^2 \text{ absolute}$
Thrust	$\tau = 10\,500 \text{ lb}_f$
Firing Time Duration	$t = 50 - 1400 \text{ sec (300 sec average)}$
Chamber Pressure	$P_o = 220 \text{ lb}_f/\text{in}^2 \text{ absolute}$
Chamber Temperature	$T_o = 5500^\circ \text{ f}$

Engine propellants are nitrogen tetroxide (N_2O_4) with 50 percent hydrogen (N_2H_4) by weight and 50 percent Unsymmetrical Dimethylhydrazine ($(\text{CH}_3)_2 \text{N}_2\text{H}_2$) by weight. As a first approximation with the chemical reaction will be



The products of combustion which will appear in the exit plane will have an estimated mean molecular weight of $\bar{M}=27.5$ and a specific heat ratio of $k = 1.4$. This latter value is somewhat conservative because the actual value for the products of combustion assumed in Eq. (1) is slightly small than this.

The exit Mach number is

$$M_e = \frac{V_e}{C_e} = \frac{V_e}{\sqrt{g v k R T_e}} = \frac{9660}{\sqrt{(32.2)(1.4) \frac{1545}{27.5} (3460)}} \quad (2)$$

The corresponding critical Mach number is $M^* = 2.02$.

Since the flow in the nozzle is supersonic and discharges into a near vacuum, the flow cannot be treated as one-dimensional, but it will be two-dimensional in nature and as an under expanded nozzle. The flow is assumed to be simple-wave flow (Prandtl-Meyer flow) which is characterized by (1) all flow properties are uniform along each Mach wave* which are straight and (2) for given initial conditions, the magnitude of the velocity at any point depends on the velocity at that point. The simple-wave flow solution lies within the linearized theory of small perturbations along with steady two-dimensional, irrotational, and isentropic motion of the supersonic velocity potential.

With these assumptions of simple wave flow, a non-dimensional function $\omega(M^*)$ can be found which will determine the maximum turning angle through which a Prandtl-Meyer flow will turn. The turning angle is dependent on the exit plane Mach number and the fluid properties. Using the before mentioned assumptions, the turning angle for maximum expansion will be about 55 degrees (Fig. H-1). This angle represents the tangent to the exhaust flow at the nozzle. Internal friction and other losses decrease the flow along this tangent (Fig. H-2).

This analysis is for steady flow and does not include the transient start-up or shut-down times. By assuming that the transient impulse is 10^{-2} of the thrust level and by taking the average thrust of start-up and shut-down, it is estimated that unsteady flow exists for a total of 25 milliseconds during firing. During this time the exhaust angle will be greater than that for steady state and there exists a possibility of some back flow around the nozzle. This time duration is considered to be short enough so that the spacecraft and RTG's will not be adversely effected.

The partial pressures of the products of combustion are:

$$\begin{array}{l}
 p_{N_2} \left\{ \begin{array}{l} = 1.38 \text{ lb}_p/\text{in}^2 \text{ absolute} \\ = 0.094 \text{ atmospheres} \end{array} \right. \\
 p_{NO_2} \left\{ \begin{array}{l} = 0.46 \text{ lb}_p/\text{in}^2 \text{ absolute} \\ = 0.0313 \text{ atm} \end{array} \right. \\
 p_{CO_2} \left\{ \begin{array}{l} = 0.46 \text{ lb}_p/\text{in}^2 \text{ absolute} \\ = 0.0313 \text{ atm} \end{array} \right.
 \end{array}$$

* Mach waves are waves along which supersonic flow with small perturbations are propagated. These waves are pressure waves across which changes in fluid properties are achieved.

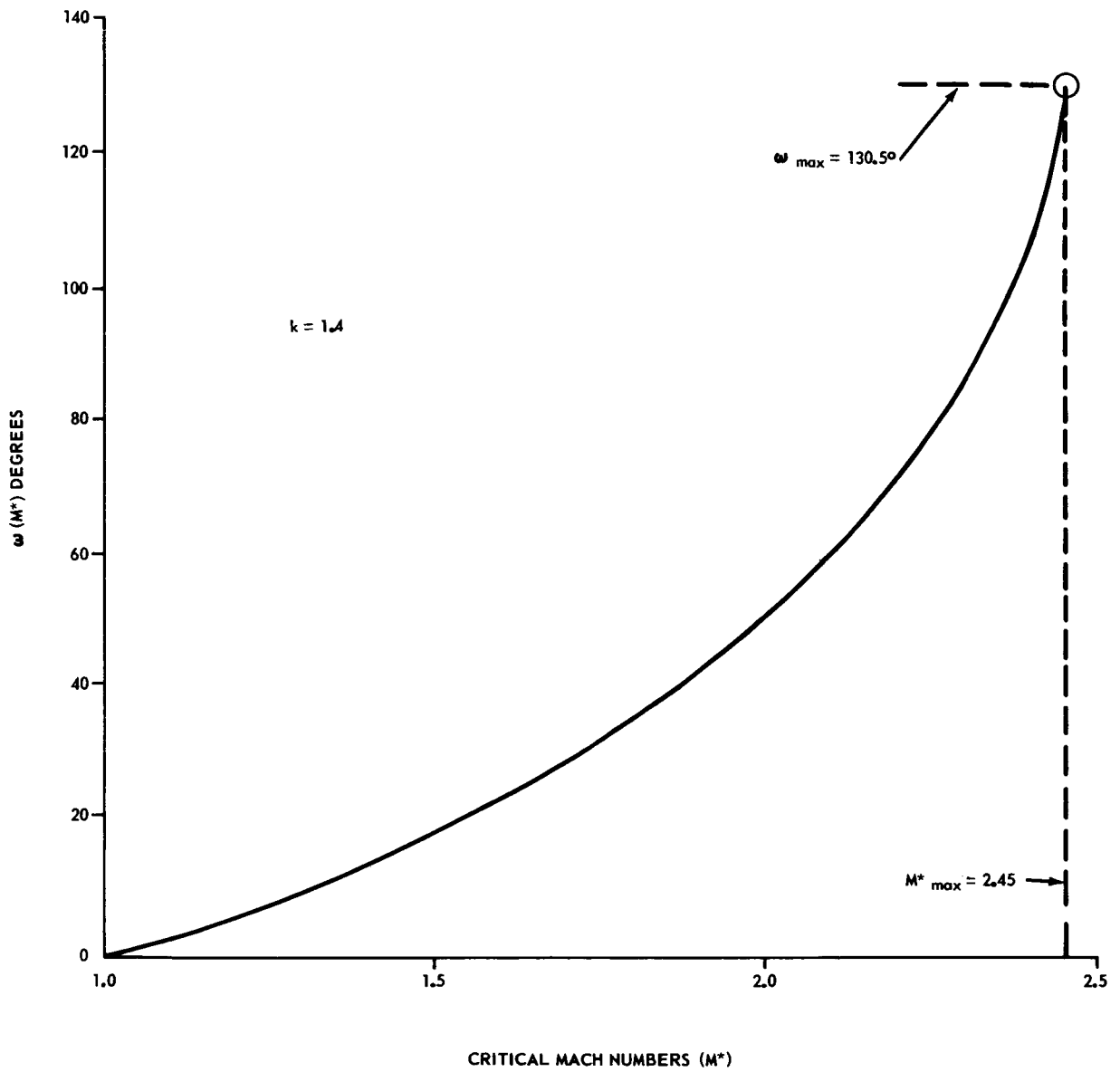


FIGURE H-1. TURNING ANGLE OF PRANDTL-MEYER FLOW

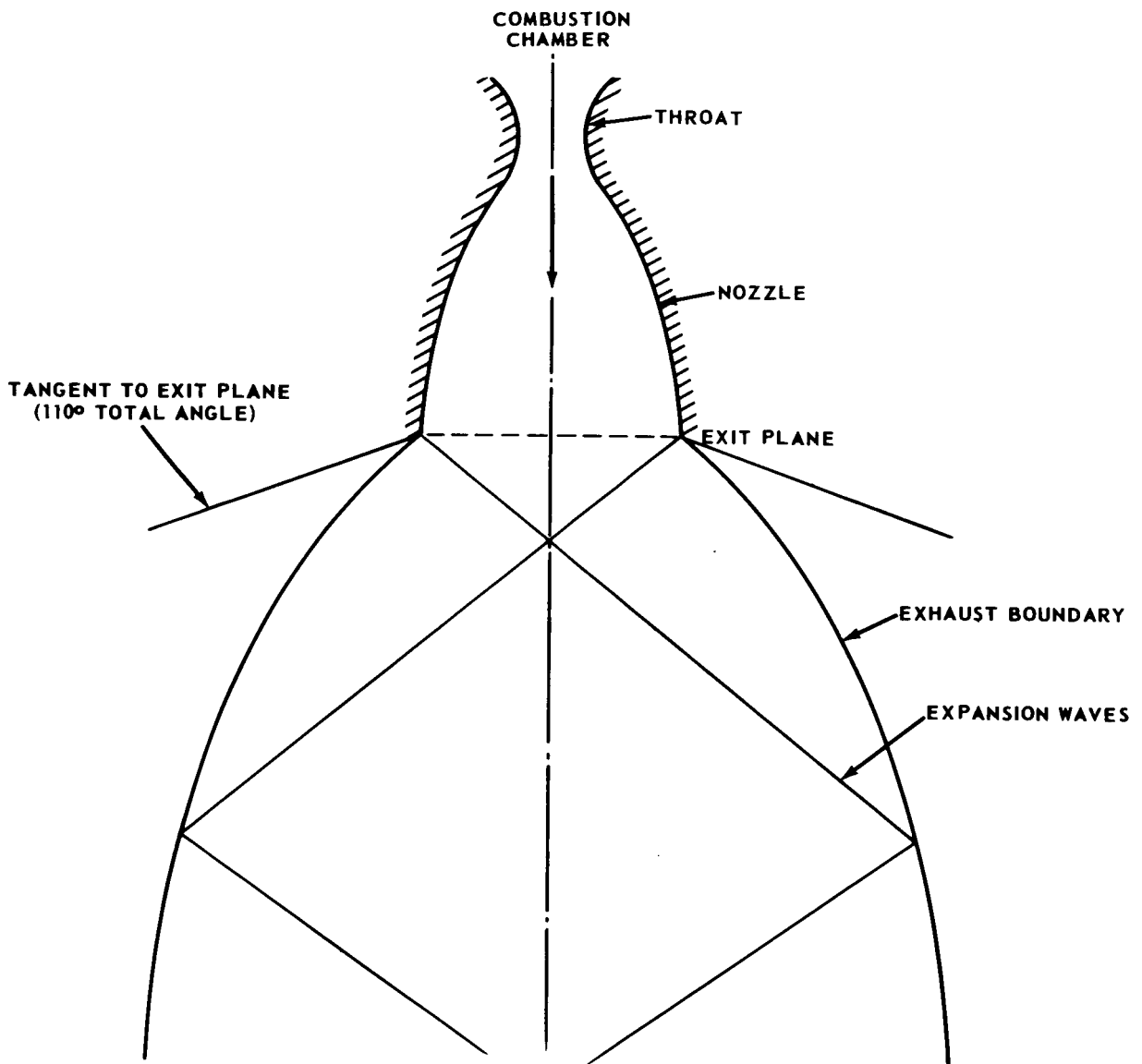


FIGURE H-2. SKETCH OF LEM ENGINE EXHAUST FOR SPACE ENVIRONMENT

$$P_{\text{H}_2\text{O}} \left\{ \begin{array}{l} = 1.84 \text{ lb}_f/\text{in}^2 \text{ absolute} \\ = 0.125 \text{ atm} \end{array} \right.$$

Of the assumed gases in the exhaust plume, only radiation from the heteropolar gases (carbon dioxide and water vapor) are of importance. For this analysis the plume will be approximated by an equivalent mean hemispherical beam length of 12 feet (Figs. H-1 and H-2). Using the partial pressures, of water vapor and carbon dioxide along with a mean plume gas temperature of 3170° R, the gas emissivities are:

$$\epsilon_{\text{H}_2\text{O}} = 0.145$$

$$\epsilon_{\text{CO}_2} = 0.06$$

Since both CO₂ and H₂ are present, the emissivities can be estimated by adding the emissivities of the two constituents giving a total emissivity of $\epsilon_T = 0.205$. In this analysis the exhaust plume has been estimated to be a cylinder of 12 feet radius and a mean temperature of 3170° R.

In order to calculate the heat transfer between the exhaust plume and the spacecraft base, the absorpctin of the plume is taken to equal the emissivity.

In order to estimate the steady state radiation from the exhaust plume to the spacecraft base a simplified model was used. This model consisted of approximating the plume by a cylinder of 12 feet in diameter and the spacecraft base by a 12 foot disk. Since these are in-line, radiation occurs between two parallel circular disks that have a common centerline. The separation distance is taken to be 10 feet. The temperature of the spacecraft disk is assumed to be that of the RTG's (850°R) while the temperature of the exhaust plume is assumed to be the average of the exit plane temperature and the ideal down-stream temperature or 3160° R (Fig. H-3).

In this model the radiation takes place only between the two disks and black space. Since the burn is for a retro maneuver, the spacecraft will be pointed toward the sun and the exhaust away from the sun. Therefore, the plume and RTG support may be assumed to see only each other and space.

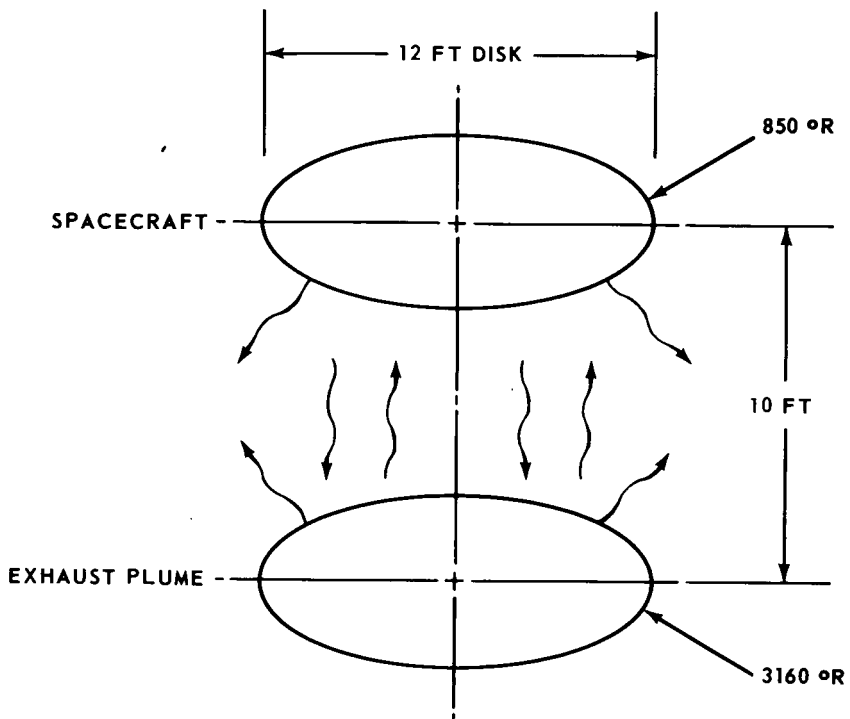


FIGURE H-3. MODEL FOR RADIANT HEAT TRANSFER FROM LEMDE EXHAUST JET TO SPACECRAFT

While it is recognized that even luminous gases do not act like solids, as a first approximation, it is assumed that the flame disk acts as a solid surface radiating to another solid disk whose absorptivity is 0.2. Then with an F_{1-2} of 0.22 (direct radiation) and $= \sigma \epsilon_1 \alpha_2 F_{1-2} (T_1^4 - T_2^4) A = 0.173 (0.205)$
 $(0.20) (0.22) (31.6^4 - 8.5^4) (113.2) = 177\ 300$ Btu/hr.

A net heat transfer of 14 790 Btu during a 300 second burn is computed. If the entire amount is absorbed by the RTG mass of 640 pounds, from $q = mc \frac{\Delta T}{p}$, the temperature rise would be 115° F. This being acceptable, no refinements in the models were attempted.

REFERENCES

1. Kreith, F.: Principles of Heat Transfer. International Textbook Company, 1965.
2. Shapiro, A. H.: The Dynamics and Thermodynamics of Compressible Fluid Flow, vol. 1, Ronald Press, 1953.